



HAL
open science

Planar antenna and antenna array optimization by shape gradient and Level Set method

Zhidong Zhao

► **To cite this version:**

Zhidong Zhao. Planar antenna and antenna array optimization by shape gradient and Level Set method. Electromagnetism. Université de Nice - Sophia Antipolis, 2015. English. NNT: 2015NICE4097. tel-01652369

HAL Id: tel-01652369

<https://hal.science/tel-01652369>

Submitted on 30 Nov 2017

HAL is a multi-disciplinary open access archive for the deposit and dissemination of scientific research documents, whether they are published or not. The documents may come from teaching and research institutions in France or abroad, or from public or private research centers.

L'archive ouverte pluridisciplinaire **HAL**, est destinée au dépôt et à la diffusion de documents scientifiques de niveau recherche, publiés ou non, émanant des établissements d'enseignement et de recherche français ou étrangers, des laboratoires publics ou privés.

UNIVERSITE DE NICE-SOPHIA ANTIPOLIS

ECOLE DOCTORALE STIC
SCIENCES ET TECHNOLOGIES DE L'INFORMATION ET DE LA COMMUNICATION

T H E S E

pour l'obtention du grade de

Docteur en Sciences

de l'Université Nice Sophia Antipolis

Mention : Electronique

présentée et soutenue par

Zhidong ZHAO

**Optimisation d'antennes et de réseaux d'antennes planaires par
gradient de forme et ensembles de niveaux (Level Sets)**

**Planar antenna and antenna array optimization by shape gradient
and Level Set method**

Thèse dirigée par *Christian PICHOT*

Soutenance prévue le 23 Novembre 2015

Jury :

M. Matteo PASTORINO	Professeur, Université de Gênes, Italie	Rapporteur
M. Giuseppe PELOSI	Professeur, Université de Florence, Italie	Rapporteur
M. Ala SHARAIHA	Professeur, Université de Rennes 1	Examineur
M. Claude DEDEBAN	Ingénieur, Orange Labs	Examineur
M. Christian PICHOT	Directeur de Recherche CNRS, UNS	Dir. de thèse

TABLE OF CONTENTS

CHAPTER 1: INTRODUCTION	1
1.1 Antenna analysis and design	3
1.2 Antenna optimization algorithms	3
1.3 Topological Gradient and Level Set method	4
CHAPTER 2: ELECTROMAGNETIC THEORY	6
2.1 General Questions	7
2.2 Maxwell Equations	7
2.3 Boundary Conditions	8
2.4 Wave Equations	9
2.5 Surface Equivalence Theorem: Huygens Principle	10
2.6 Radiation condition	11
2.7 Green's Function	12
2.8 EFIE and MFIE Equations Definition	12
2.9 Reaction Concept	14
2.10 Variational Formulation	15
CHAPTER 3: SR3D	17
3.1 Linear system	18
3.2 Reaction Matrix Z	19
3.3 Source Vector Definition	24
3.4 Reaction Matrix Discretization	26
3.5 Source Vector Discretization	28
CHAPTER 4: OPTIMIZATION TECHNIQUES	30
4.1 Global and local optimization	31
4.2 Stochastic method	32
4.2.1 Genetic Algorithms	33
4.2.2 Particle swarm optimization	33
4.2.3 Simulated annealing	34
4.2.4 Ant colony optimization	34
4.3 Deterministic method	34
4.3.1 Shape gradients calculation	35
4.3.2 Shape optimization using shape gradients	35
CHAPTER 5: SHAPE GRADIENT	37
5.1 Discrete method	39
5.2 Adjoint method	40
5.3 Analytical method	40
5.4 Shape gradient based on topological deformation	46
5.4.1 Contour definition of shape geometry	46
5.4.2 Shape Gradient method using nodal point mesh derivation	48
5.4.3 Topological Gradient method	49`

CHAPTER 6: LEVEL SET METHOD	53
6.1 General Description	54
6.2 The Level Set Function.....	54
6.3 The Normal Velocity.....	56
6.4 The Narrow Band method	58
6.5 Re-initialization	59
6.6 An upper limit to the size of Δt	60
6.7 Apply shape gradient to Level Set method.....	61
6.8 Procedure of Level Set optimization.....	62
CHAPTER 7: NUMERICAL VALIDATIONS.....	63
7.1 Study of the scattered field of a cylinder antenna.....	64
7.2 Validation of the adjoint formula for a cylinder antenna	68
7.3 Validation of the adjoint formula for a 2D patch antenna.....	70
7.4 Validation of the adjoint formula for a 3D patch antenna.....	73
7.4.1 Thin 3D patch antenna enlarging along all normal direction	73
7.4.2 Thin 3D patch antenna enlarging along +x direction	79
7.4.3 Thick 3D antenna enlarging along +x direction	80
7.5 Shape gradient computation by different shape deformations	82
CHAPTER 8: NUMERICAL EXPERIMENTS.....	86
8.1 Antenna array location optimization using conjugate gradient and analytical gradient method	88
8.1.1 Illumination of single-frequency-single-incident wave	89
8.1.2 Illumination of multi-frequency-multi-incident wave	90
8.2 Shape Optimization of a single square patch antenna using nodal point mesh derivation	94
8.2.1 Shape Optimization from an initial guess in the center.....	94
8.2.2 Shape Optimization from an initial guess in the corner.....	97
8.3 Shape optimization of a single patch antenna	101
8.3.1 Shape optimization using nodal point mesh derivation.....	102
8.3.2 Shape optimization using Topological Gradient without noise	104
8.3.3 Shape optimization using Topological Gradient with 20 dB noise	108
8.3.4 Shape Optimization using Topological Gradient with 10 dB noise	112
8.4 Shape Optimization of two rectangular patch antenna arrays using topological gradient	116
8.5 Shape Optimization of two circular patch antenna arrays	120
8.5.1 Shape Optimization using Frequency-hopping technique	121
8.5.2 Shape Optimization using multi-frequency technique	124
8.6 Shape Optimization of a single U-shape reflectarray element using topological gradient.....	130
8.6.1 Optimization from an initial guess of a larger size element	130
8.6.2 Optimization from an initial guess of a smaller size element.....	134
GENERAL CONCLUSION.....	143
Annex 1 - Spherical Coordinate System.....	146
Annex 2 - Calculation of Scattering Field	149

Annex 3 - Signal-to-noise ratio for Robustness test	154
BIBLIOGRAPHY	159

CHAPTER 1: INTRODUCTION

The inverse scattering problem for finding the optimal design of printed antenna arrays is particularly interesting for reflectarrays antennas and planar antenna arrays, which contain various types of printed elements. However, the design and optimization procedure require severe and efficient inverse and synthesis methods to meet the imposed constraints.

In this thesis, starting from Rumsey reaction concept, we describe an electromagnetic solver based on an integral formulation of the EM problem (SR3D code) for finding the forward electromagnetic solution. From this code, we have developed several inversion gradient-based algorithms to optimize planar antenna arrays. Especially, we give a new sense to the shape gradient versus an edge deformation (or transformation) in 3D for metallic layers with limited surfaces. The derived numerical model allows studying planar structures with the notion of metallic layer with a 2D outward normal direction.

In order to implement optimization procedure, we use level set method. The difficulty of the algorithm relies on finding the corresponding shape deformation velocities in the normal direction of contour, which we compute by the shape gradients (or shape sensitivity) versus radiation pattern modification taking into account the modeling of the antenna (Finite Element mesh).

In order to investigate the performance of the inverse algorithm and optimization procedure, different configurations are studied and shown in this thesis.

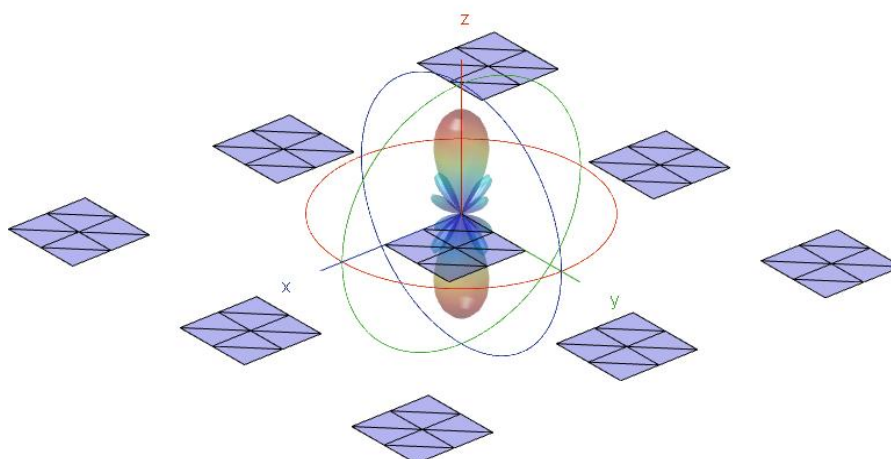


Figure1.1 Radiation Pattern radiated by antenna arrays

1.1 Antenna analysis and design

Antenna or antenna array structural design is a procedure to improve or enhance the performance of an existing structure by changing its parameters. The engineering design of the structural antenna in the simulation-based design process consists of antenna structure modeling, antenna design parameterization, antenna structure analysis, antenna geometry sensitivity analysis, and design optimization procedure.

The goal of antenna analysis is to determine the radiation characteristics, such as the radiation pattern and input impedance for a given antenna structure. The calculation of radiation pattern and input impedance requires solving Maxwell equations subject to certain boundary conditions, which are determined by antenna configurations. Unfortunately, we can only obtain analytical solution directly for a very few idealized and classical antenna geometries. However, for complex antenna structures, full-wave solutions to Maxwell equations are required to obtain reliable and accurate analysis.

Typically, the antenna design is based on numerical methods for solving Maxwell equations such as the Method of Moments (MoM), Finite Element Method (FEM), Finite Difference Time-Domain method (FDTD) and Transmission Line Matrix (TLM). Each numerical method has advantages and weak points concerning the computational cost, the level of accuracy, and the material modeling.

Antenna parametric studies are then performed to optimize the size of the structure under different constraints such as the return loss (S11 parameter), directivity, radiation pattern, polarization (linear, circular), or inter-element coupling. The quality of an optimized design is dependent on the parameterization of the optimization domain and the number of variables used. The use of a large number of variables leads to a large number of possible solutions and increases the complexity of the inverse problem.

1.2 Antenna optimization algorithms

Starting from an initial guess for the design variables of an existing geometry, optimization algorithms help to seek a solution of a formulated optimization problem by generating a sequence of updated design variables. In order to minimize the value of cost functional, at each step of optimization procedure, optimization algorithms are used to update the design variables by using the available information.

The multi-object optimization with the optimization of meta-heuristics (iterative stochastic algorithms) including evolutionary algorithms, such as the genetic algorithms (GA: Genetic Algorithms) [9-13], the simulated annealing (SA:

Simulated Annealing) algorithms, the particle swarm optimization (PSO: Particle Swarm Optimization) [14], ant colonies (ACO: Ant Colony Optimization) [15] or algorithms based on bad invasive weeds (IWO: invasive Weed Optimization) [16] or several hybrid stochastic algorithms [17], have been and are still widely used to optimize various electromagnetic devices. All evolutionary algorithms mentioned have shown their ability to find a global solution (in the sense of the global minimum of the objective or cost function to be minimized) of many optimization problems and synthesis of antennas and antenna arrays. However, the weak number of parameters or information contained in the objective or cost function to minimize, combined with the random strategy of evolutionary algorithms, is ineffective and thus optimizes complex structures with a large number of variables.

Gradient-based optimization algorithms have been used to solve inverse scattering electromagnetic problems and antenna optimization. Gradient-based optimization algorithms can converge faster towards the minimum, but on the other hand, the global convergence cannot be guaranteed. However, we can still use some techniques, able to improve the convergence performance of gradient type optimization algorithms. Using a priori or extra information or fixing some constraints, to the optimization procedure or by modifying the cost functional using regularization for example, may enhance the global convergence. We can use extra information with a frequency hopping technique, where the optimization is performed with respect to several frequencies and defining the final cost functional combining the results derived from each frequency. We can also use a multi-frequency technique by gathering all the information derived from a sequence of frequencies at each iteration. In addition, we can also control the size of the optimal time step in when using level set method. A large time-step speeds up the inherently slow curve evolution process, but the question is: how large value of Δt can we use? It was observed that, for small values of the time-step, though the convergence was slow, curve evolution results were satisfactory. When large time-steps were used to speed up the evolution process, we often got garbage outputs. Clearly there is a stability issue that depends on the value of the time-step Δt employed. We can also use the value of the CFL (Courant-Friedrichs-Lewy) [29] coefficient. All these techniques are able to modify the convergence of the cost functional.

1.3 Topological Gradient and Level Set method

When solving a problem of topology optimization, the number of variables can easily reach to thousands or even millions for 2D and 3D cases. The optimization techniques of gradient type are generally preferred to solve problems with a large number of variables. The main reason is that the

gradient of the objective function or cost function contains a lot of important information. The shape gradient based on an adjoint formulation [1-8] is only valid for a 3D regular closed surface where the outward-pointing normal is defined everywhere, which is not the case for planar or patch antennas. The numerical models to study metal planar structures typically use the concept of perfect conducting layer in a plane domain bounded by a closed curve. Then in the case of open structures, or in the case of structures with edges, the definition of adjoint problem can be problematic or very complex mathematically. Therefore, it is particularly interesting to carry out sensitivity analysis from the objective or cost function to determine the most sensitive parameters to optimize. The precise calculation of the shape gradient for the miniaturization of antennas is an imperative one for topology optimization with gradient type methods.

Level Set method is extremely suitable for reflectarray antenna and planar antenna array optimization, since it is able to compute geometric quantities, and handle topology changes easily. The shape of elements can be merged and separated, because the Hamilton-Jacobi equation is working on a higher dimension, it means that it is not only able to optimize the shape of element, and also the element number.

CHAPTER 2: ELECTROMAGNETIC THEORY

2.1 General Questions

In general, for electromagnetic problems, there are two main problems to solve: the forward and inverse problem. For the forward problem, when the incident sources, geometry of the structures, and their electromagnetic properties are completely defined, we need to find the solution of their interaction. While for the electromagnetic inverse problem, when the interaction of the electromagnetic field is known in a certain domain, we need to determine the all properties of the illumined structures, including the geometry information, electromagnetic properties, provided the incident sources are known.

An important point for solving the electromagnetic inverse problem is that the inversion algorithm must be based on a solution of the forward modelling that correctly solves the electromagnetic responses or interaction.

In this work, we are going to use an electromagnetic solver named SR3D ("Structures Rayonnantes 3D" meaning "3D Radiating Structures") based on a method of moment, for solving the electromagnetic forward problem. In this chapter, starting from Maxwell equations, we introduce the theoretical basis of SR3D solver, with the reaction concept and the variational formulation.

2.2 Maxwell Equations

Maxwell equations describe the property of electromagnetic waves and fields. Consider a homogeneous, isotropic domain Ω with boundary Γ defined by electric permittivity ε , magnetic permeability μ and conductivity σ . The electromagnetic wave is described by \bar{E} and \bar{H} , which corresponds to electric and magnetic fields, respectively. The Maxwell equations are defined here with a time-dependence $e^{-i\omega t}$:

$$\left\{ \begin{array}{l} \nabla \times \bar{E} = i\omega \bar{B} - \bar{M} \\ \nabla \times \bar{H} = -i\omega \bar{D} + \bar{J} \\ \nabla \cdot \bar{D} = \rho_e \\ \nabla \cdot \bar{B} = \rho_m \end{array} \right. \quad (2.1)$$

with:

ω	angular frequency
\bar{J}	electric current density
\bar{M}	magnetic current density
\bar{D}	electric induction
\bar{B}	magnetic induction
ρ_e	electric charge density
ρ_m	magnetic charge density

The Maxwell equations are first-order linear coupled differential equations relating the vector field quantities to each other. In addition to these four Maxwell equations, there are four medium-dependent equations, which are related with the constitutive relations:

$$\begin{aligned}
 \bar{D} &= \epsilon \bar{E} \\
 \bar{J} &= \sigma \bar{E} \\
 \bar{B} &= \mu \bar{H} \\
 \bar{M} &= \sigma_m \bar{H}
 \end{aligned}
 \tag{2.2}$$

with:

$$\begin{aligned}
 \epsilon &= \epsilon_0 \epsilon_r \\
 \mu &= \mu_0 \mu_r
 \end{aligned}$$

The magnetic and electric charge densities are defined as:

$$\begin{aligned}
 \nabla \cdot \bar{J} - i\omega \rho_e &= 0 \\
 \nabla \cdot \bar{M} - i\omega \rho_m &= 0
 \end{aligned}
 \tag{2.3}$$

2.3 Boundary Conditions

The material medium in which EM field exists is usually characterized by its constitutive parameters: the electric permittivity ϵ , the magnetic permeability μ and the conductivity σ . Consider the situation in which one medium, characterized by ϵ_1 and μ_1 and σ_1 , shares an interface with another medium, characterized by ϵ_2 , μ_2 and σ_2 . In order to solve for EM problems, at the interface, the tangential and normal fields must satisfy the boundary conditions:

$$\begin{aligned}
 \hat{n} \times (\bar{H}_2 - \bar{H}_1) &= \bar{J}_s \\
 \hat{n} \times (\bar{E}_2 - \bar{E}_1) &= -\bar{M}_s \\
 \hat{n} \cdot (\bar{D}_2 - \bar{D}_1) &= \rho_{es} \\
 \hat{n} \cdot (\bar{B}_2 - \bar{B}_1) &= \rho_{ms}
 \end{aligned}
 \tag{2.4}$$

where \hat{n} is a unit normal vector directed from medium 2 to medium 1.

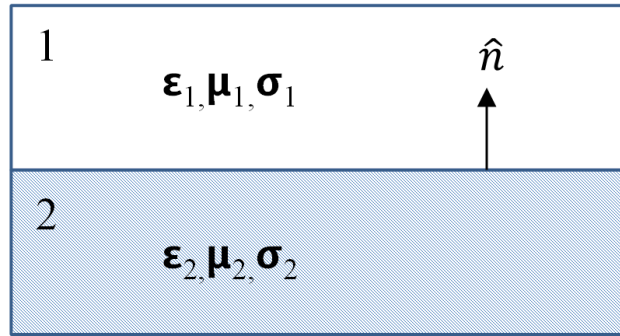


Figure 2.1: Boundary Conditions

In the case of a PEC boundary, we can write them as:

$$\begin{aligned}
 \hat{n} \times \bar{H}_2 &= \bar{J}_s \\
 \hat{n} \times \bar{E}_2 &= -\bar{M}_s \\
 \hat{n} \cdot \bar{E}_2 &= \rho_{es} / \epsilon_2 \\
 \hat{n} \cdot \bar{H}_2 &= 0
 \end{aligned}
 \tag{2.5}$$

2.4 Wave Equations

Maxwell equations are first-order coupled differential equations, difficult to solve as boundary-value problem. We can obtain a second-order differential equation (Helmholtz equation) that may be useful for solving electromagnetic problems.

We apply the operator $\Delta(\) = \nabla \nabla \cdot (\) - \nabla \times \nabla \times (\)$ on the two first equations and obtain:

$$\begin{aligned}
 (\Delta + k^2) \bar{E} &= -\frac{i}{\omega \epsilon} (\nabla \nabla \cdot \bar{J} + k^2 \bar{J}) + \nabla \times \bar{M} \\
 (\Delta + k^2) \bar{H} &= -\frac{i}{\omega \mu} (\nabla \nabla \cdot \bar{M} + k^2 \bar{M}) - \nabla \times \bar{J}
 \end{aligned}
 \tag{2.6}$$

with k wavenumber

$$k = \omega\sqrt{\epsilon\mu}$$

The wave equation or Helmholtz equation can be written as:

$$\begin{aligned} (\Delta + k^2)\bar{E} &= 0 \\ (\Delta + k^2)\bar{H} &= 0 \end{aligned} \tag{2.7}$$

2.5 Surface Equivalence Theorem: Huygens Principle

To solve radiation and scattering problems, it is often useful to formulate the problem in terms of an equivalent one which may be more convenient to solve. In the analysis of electromagnetic problems, it is possible to replace the real sources defined in the investigation domain with superficial sources on a closed surface. According to the Huygens' principle, we can substitute the general inhomogeneous volume problem with an ensemble of homogeneous and superficial problems, so that the problems of electric and magnetic fields can be replaced by the problems of surface currents, which can be defined as follows:

$$\begin{aligned} \bar{J}_s &= \hat{n} \times \bar{H}_s \\ \bar{M}_s &= -\hat{n} \times \bar{E}_s \\ \rho_{es} &= \epsilon \hat{n} \cdot \bar{E}_s \\ \rho_{ms} &= \mu \hat{n} \cdot \bar{H}_s \end{aligned} \tag{2.8}$$

We can replace the problem (a) with problem (b) by using the superficial currents. In the special case (c), the material in V_1 is an electric conductor, the magnetic currents on the surface is zero, while in the case (d), the material in V_1 is magnetic conductor, the electric currents on the surface is zero. [47]

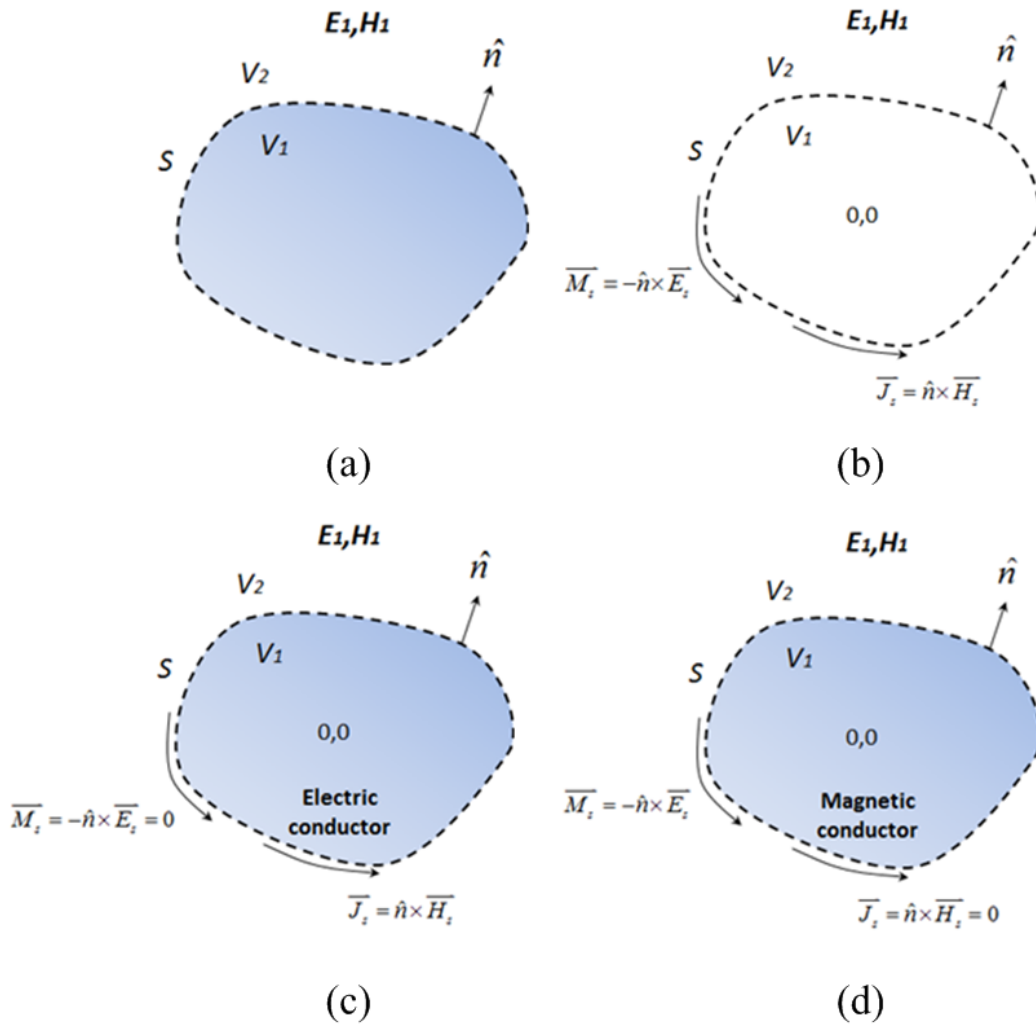


Figure 2.2: Huygens' equivalent Principle

2.6 Radiation Condition

The electromagnetic field must satisfy the next two conditions, which are the radiation conditions and finite energy conditions respectively:

$$\lim_{r \rightarrow \infty} \left(\hat{n} \times \bar{\nabla} \times \bar{E} - jk\bar{E} \right) = o\left(\frac{1}{r}\right)$$

$$\lim_{r \rightarrow \infty} \left(\hat{n} \times \bar{\nabla} \times \bar{H} - jk\bar{H} \right) = o\left(\frac{1}{r}\right)$$

$$\int_{\Omega} \|\bar{E}\|^2 d\Omega < \infty$$

$$\int_{\Omega} \|\bar{H}\|^2 d\Omega < \infty$$

They indicate that the energy, in the local closed domain Ω , is finite.

2.7 Green's Function

The Green's function is solution of the equation:

$$\begin{aligned} (\Delta + k^2)G(x, y) &= -\delta(x, y) \\ \text{with: } \delta(x, y) &= \begin{cases} 1 & \text{if } x=y=0 \\ 0 & \text{else} \end{cases} \end{aligned} \quad (2.9)$$

In \mathfrak{R}^3 , we have the general solution:

$$\begin{aligned} G(x, y) &= \frac{e^{\pm ikR}}{4\pi R} \\ \text{with: } R &= \|xy\| \end{aligned} \quad (2.10)$$

The radiation condition shows that the scattered wave is only an outgoing wave. The Green's function of the free space is then:

$$G(x, y) = G(R) = \frac{e^{ikR}}{4\pi R} \quad (2.11)$$

We can apply this equation to (2.6):

We then obtain:

$$\begin{aligned} \bar{E}(\bar{r}) &= \frac{i}{\omega\epsilon} (\nabla\nabla \cdot + k^2) \left(\bar{J}(\bar{r}') \times \bar{G}(\bar{r}, \bar{r}') \right) - \nabla \times \left(\bar{M}(\bar{r}') \times \bar{G}(\bar{r}, \bar{r}') \right) \\ \bar{H}(\bar{r}) &= \frac{i}{\omega\mu} (\nabla\nabla \cdot + k^2) \left(\bar{M}(\bar{r}') \cdot \bar{G}(\bar{r}, \bar{r}') \right) + \nabla \times \left(\bar{J}(\bar{r}') \times \bar{G}(\bar{r}, \bar{r}') \right) \end{aligned} \quad (2.12)$$

2.8 EFIE and MFIE Equations Definition

If we apply the Huygens principle to the inhomogeneous radiation and scattering problems, we can thereafter describe this problem as an equivalent surface electromagnetic problem. It also means that scattering problems can be considered as radiation problems where the local radiating currents are generated by other currents or fields.

We can firstly write the total field as:

$$\begin{aligned} \bar{E}(\bar{r}) &= \bar{E}^{inc}(\bar{r}) + \bar{E}^{sca}(\bar{r}) \\ \bar{H}(\bar{r}) &= \bar{H}^{inc}(\bar{r}) + \bar{H}^{sca}(\bar{r}) \end{aligned} \quad (2.13)$$

Using the Green's function, we can integrate over a closed surface domain Γ , where we have equivalent surface currents. Then, we can obtain the scattered field, and the total field:

$$\begin{aligned}\bar{E}(\bar{r}) &= \bar{E}^{inc}(\bar{r}) + j\omega\mu \oint_{\Gamma} G(\bar{r}, \bar{r}') \bar{J}(\bar{r}') d\Gamma \\ &+ \frac{j}{\omega\epsilon} \oint_{\Gamma} \bar{\nabla}_{\bar{r}} G(\bar{r}, \bar{r}') \bar{\nabla}_{\Gamma} \cdot \bar{J}(\bar{r}') d\Gamma - \bar{\nabla} \times \oint_{\Gamma} G(\bar{r}, \bar{r}') \bar{M}(\bar{r}') d\Gamma\end{aligned}\quad (2.14)$$

$$\begin{aligned}\bar{H}(\bar{r}) &= \bar{H}^{inc}(\bar{r}) + j\omega\epsilon \oint_{\Gamma} G(\bar{r}, \bar{r}') \bar{M}(\bar{r}') d\Gamma \\ &+ \frac{j}{\omega\mu} \oint_{\Gamma} \bar{\nabla}_{\bar{r}} G(\bar{r}, \bar{r}') \bar{\nabla}_{\Gamma} \cdot \bar{M}(\bar{r}') d\Gamma - \bar{\nabla} \times \oint_{\Gamma} G(\bar{r}, \bar{r}') \bar{J}(\bar{r}') d\Gamma\end{aligned}\quad (2.15)$$

The unknown local currents J and M are created by an external but known incident field \bar{E}^{inc} and \bar{H}^{inc} , the field E and H can be solved by an integral equation.

$$\begin{aligned}\bar{E}^{inc}(\bar{r}) &= j\omega\mu \oint_{\Gamma} G(\bar{r}, \bar{r}') \bar{J}_a(\bar{r}') d\Gamma \\ &+ \frac{j}{\omega\epsilon} \oint_{\Gamma} \bar{\nabla}_{\bar{r}} G(\bar{r}, \bar{r}') \bar{\nabla}_{\Gamma} \cdot \bar{J}_a(\bar{r}') d\Gamma - \bar{\nabla} \times \oint_{\Gamma} G(\bar{r}, \bar{r}') \bar{M}_a(\bar{r}') d\Gamma\end{aligned}\quad (2.16)$$

$$\begin{aligned}\bar{H}^{inc}(\bar{r}) &= j\omega\epsilon \oint_{\Gamma} G(\bar{r}, \bar{r}') \bar{M}_a(\bar{r}') d\Gamma \\ &+ \frac{j}{\omega\mu} \oint_{\Gamma} \bar{\nabla}_{\bar{r}} G(\bar{r}, \bar{r}') \bar{\nabla}_{\Gamma} \cdot \bar{M}_a(\bar{r}') d\Gamma - \bar{\nabla} \times \oint_{\Gamma} G(\bar{r}, \bar{r}') \bar{J}_a(\bar{r}') d\Gamma\end{aligned}\quad (2.17)$$

We have to enforce the boundary conditions on the tangential electric and magnetic fields:

$$\begin{aligned}\hat{n}(\mathbf{r}) \times \bar{E}^{sca}(\bar{r}) &= -\hat{n}(\mathbf{r}) \times \bar{E}^{inc}(\bar{r}) \\ \hat{n}(\mathbf{r}) \times \bar{H}^{sca}(\bar{r}) + \hat{n}(\mathbf{r}) \times \bar{H}^{inc}(\bar{r}) &= \bar{J}(\bar{r})\end{aligned}\quad (2.18)$$

where $\hat{n}(\mathbf{r})$ is the outward surface normal.

This allows us to write the above in terms of the known incident electric field $\vec{E}^{inc}(\vec{r})$ and magnetic field $\vec{H}^{inc}(\vec{r})$ as:

$$\begin{aligned} \hat{n} \times \vec{E}^{inc}(\vec{r}) = & -\hat{n} \times \left\{ j\omega\mu \oint_{\Gamma} G(\vec{r}, \vec{r}') \vec{J}(\vec{r}') d\Gamma \right. \\ & + \frac{j}{\omega\epsilon} \oint_{\Gamma} \vec{\nabla}_{\vec{r}'} G(\vec{r}, \vec{r}') \vec{\nabla}_{\Gamma} \cdot \vec{J}(\vec{r}') d\Gamma \\ & \left. - \oint_{\Gamma} \vec{M}(\vec{r}') \vec{\nabla}_{\vec{r}'} G(\vec{r}, \vec{r}') d\Gamma - \frac{1}{2} \hat{n} \times \vec{M}(\vec{r}') \right\} \end{aligned} \quad (2.19)$$

$$\begin{aligned} \hat{n} \times \vec{H}^{inc}(\vec{r}) = & -\hat{n} \times \left\{ j\omega\epsilon \oint_{\Gamma} G(\vec{r}, \vec{r}') \vec{M}(\vec{r}') d\Gamma \right. \\ & + \frac{j}{\omega\epsilon} \oint_{\Gamma} \vec{\nabla}_{\vec{r}'} G(\vec{r}, \vec{r}') \vec{\nabla}_{\Gamma} \cdot \vec{M}(\vec{r}') d\Gamma \\ & \left. + \oint_{\Gamma} \vec{J}(\vec{r}') \times \vec{\nabla}_{\vec{r}'} G(\vec{r}, \vec{r}') d\Gamma + \frac{1}{2} \hat{n} \times \vec{J}(\vec{r}') \right\} \end{aligned} \quad (2.20)$$

These two equations are called as the Electric Field Equation (EFIE) and the Magnetic Field Equation (MFIE).

2.9 Reaction Concept

The variational formulation can be obtained using the Rumsey reaction concept. Given an homogeneous domain Ω , with boundary surface Γ , sources $\{\vec{J}, \vec{M}\}$ and test sources $\{\vec{J}^{test}, \vec{M}^{test}\}$ defined along the tangent direction of

surface Γ and with boundary condition defined, then the reaction of sources on the test sources in Ω is defined as a following bilinear form:

$$R_{\Omega} \left(\left\{ \vec{J}, \vec{M} \right\}, \left\{ \vec{J}^{test}, \vec{M}^{test} \right\} \right) = \oint_{\Gamma} \left(\vec{E} \cdot \vec{J}^{test} - \left(\vec{M}^{test} \cdot \vec{H} \right) \right) d\Gamma^{test} \quad (2.21)$$

Where the electromagnetic field $\{\vec{E}, \vec{H}\}$ is generated by the surface currents $\{\vec{J}, \vec{M}\}$ defined inside Ω . We can also apply this concept to the incident

electromagnetic field $\{\vec{E}^{inc}, \vec{H}^{inc}\}$ generated by the surface currents $\{\vec{J}_a, \vec{M}_a\}$

inside Ω , the bilinear form for the incident waves can be written as:

$$R_{\Omega} \left(\left\{ \bar{J}_a, \bar{M}_a \right\}, \left\{ \bar{J}^{test}, \bar{M}^{test} \right\} \right) = \oint_{\Gamma} \left(\bar{E}^{inc} \cdot \bar{J}^{test} - \left(\bar{M}^{test} \cdot \bar{H}^{inc} \right) \right) d\Gamma^{test} \quad (2.22)$$

Both bilinear forms (C2.20) and (C2.21) have a symmetric property. So we can write the reciprocity principle:

$$R_{\Omega} \left(\left\{ \bar{J}, \bar{M} \right\}, \left\{ \bar{J}^{test}, \bar{M}^{test} \right\} \right) = R_{\Omega} \left(\left\{ \bar{J}_a, \bar{M}_a \right\}, \left\{ \bar{J}^{test}, \bar{M}^{test} \right\} \right) \quad (2.23)$$

2.10 Variational Formulation

If we use the equation (C2.16) and equations shown in (C2.20) and (C2.21), and apply the boundary conditions, we obtain:

$$R_{\Omega} \left(\left\{ \bar{J}, \bar{M} \right\}, \left\{ \bar{J}^{test}, \bar{M}^{test} \right\} \right) - R_{\Omega} \left(\left\{ \bar{J}_a, \bar{M}_a \right\}, \left\{ \bar{J}^{test}, \bar{M}^{test} \right\} \right) = 0 \quad (2.24)$$

We also define $\bar{E} = j\omega\mu_0 \bar{e}$, $\bar{M} = j\omega\mu_0 \bar{p}$ and $\bar{J} = \bar{j}$, develop equation (C2.20). After few mathematical transformations, we can obtain:

$$\begin{aligned} -S \left(\bar{E}^{inc}, \bar{H}^{inc}, \bar{j}^{test}, \bar{p}^{test} \right) &= \mu R_1 \left(\bar{j}, \bar{j}^{test} \right) + \frac{k^2}{\mu_r} R_1 \left(\bar{p}, \bar{p}^{test} \right) \\ &+ R_2 \left(\bar{j}, \bar{p}^{test} \right) + R_2 \left(\bar{p}, \bar{j}^{test} \right) \end{aligned} \quad (2.25)$$

The kernel terms can be defined as follows:

$$\begin{aligned} R_1 \left(\bar{a}, \bar{a}^{test} \right) &= \oint \oint (G) \left(\bar{a} \cdot \bar{a}^{test} \right) d\Gamma d\Gamma^{test} - \frac{1}{k^2} \oint \oint (G) \left(\bar{\nabla} \cdot \bar{a} \bar{\nabla} \cdot \bar{a}^{test} \right) d\Gamma d\Gamma^{test} \\ R_2 \left(\bar{a}, \bar{b}^{test} \right) &= \oint \oint \left(\left(\bar{\nabla}_r \cdot G \times \bar{a} \right) \cdot \bar{b}^{test} \right) d\Gamma d\Gamma^{test} \end{aligned} \quad (2.26)$$

If we apply the Huygens principle for a homogenous domain Ω , the domain can be divided in several sub-domains Ω_i , by considering the boundaries Γ_i generated by the subdomains Ω_i . Therefore, we can define the Rumsey concept on different N_d subdomains:

$$\sum_{i=1}^{N_d} R_{\Omega_i} \left(\left\{ \bar{J}, \bar{M} \right\}, \left\{ \bar{J}_i^{test}, \bar{M}_i^{test} \right\} \right) - R_{\Omega_i} \left(\left\{ \bar{J}_a, \bar{M}_a \right\}, \left\{ \bar{J}_i^{test}, \bar{M}_i^{test} \right\} \right) = 0 \quad (2.27)$$

$$-\sum_{i=1}^{N_d} S \left(\bar{E}^{inc}, \bar{H}^{inc}, \bar{j}, \bar{p} \right) = \sum_{i=1}^{N_d} \left[\mu R_{1i} \left(\bar{j}, \bar{j}^{test} \right) + \frac{k^2}{\mu_r} R_{1i} \left(\bar{p}, \bar{p}^{test} \right) \right. \\ \left. + R_{2i} \left(\bar{j}, \bar{p}^{test} \right) + R_{2i} \left(\bar{p}, \bar{j}^{test} \right) \right] \quad (2.28)$$

.28)

CHAPTER 3: SR3D

In this chapter, we start from the Rumsey reaction equation written in chapter 2, then define the MoM linear system, and finally describe every term of the linear system, including the reaction matrix and source vector.

3.1 Linear System

We can write the Rumsey reaction form related to a single couple of triangles T_K and T_L :

$$\begin{aligned}
 -S\left(\begin{matrix} \overline{E}^{inc} & \overline{H}^{inc} & \overline{j}^{-K} & \overline{p}^{-K} \end{matrix}\right) &= \mu R_1^{KL}\left(\begin{matrix} \overline{j}^{-L} & \overline{j}^{-K} \end{matrix}\right) + \frac{k^2}{\mu_r} R_1^{KL}\left(\begin{matrix} \overline{p}^{-L} & \overline{p}^{-K} \end{matrix}\right) \\
 &+ R_2^{KL}\left(\begin{matrix} \overline{j}^{-L} & \overline{p}^{-K} \end{matrix}\right) + R_2^{KL}\left(\begin{matrix} \overline{p}^{-L} & \overline{j}^{-K} \end{matrix}\right)
 \end{aligned} \tag{3.1}$$

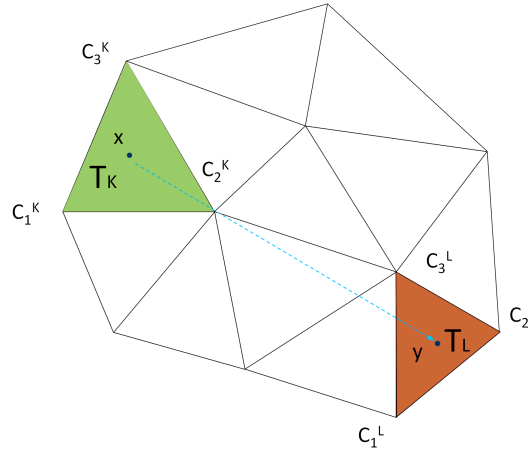


Figure 3.1: Coupling reaction between triangles

The terms R and S , which denote the coupling terms and source vector respectively, are defined by the following equation:

$$\begin{aligned}
 R_1\left(\begin{matrix} \overline{a}^{-L} & \overline{a}^{-K} \end{matrix}\right) &= \oint_{T_K} \oint_{T_L} G(\overline{x}, \overline{y}) \left(\overline{a}^{-L}(\overline{y}) \cdot \overline{a}^{-K}(\overline{x}) \right) dy dx \\
 &- \frac{4H_K H_L}{k^2} \oint_{T_K} \oint_{T_L} G(\overline{x}, \overline{y}) dy dx \\
 R_2\left(\begin{matrix} \overline{a}^{-L} & \overline{b}^{-K} \end{matrix}\right) &= \oint_{T_K} \oint_{T_L} \left(\overline{\nabla}_{\overline{y}} G(\overline{x}, \overline{y}) \times \overline{a}^{-L}(\overline{y}) \right) \cdot \overline{b}^{-K}(\overline{x}) dy dx \\
 S\left(\begin{matrix} \overline{E}^{inc} & \overline{H}^{inc} & \overline{j}^{-K} & \overline{p}^{-K} \end{matrix}\right) &= \int_{T_K} \left(\overline{E}^{inc} \cdot \overline{j}^{-K} - \overline{H}^{inc} \cdot \overline{p}^{-K} \right) dx
 \end{aligned} \tag{3.2}$$

$$\text{where: } H_T = \frac{1}{2\Lambda_T}, \Lambda_T \text{ is the surface of triangle T}$$

Then we can define the sub-linear system related to the triangles T_K and T_L as:

$$[S^K] = [Z^{KL}] [\Phi^L] \quad (3.3)$$

The electric J^L and magnetic M^L density surface currents contained in Φ^L are the solutions of the sub-system. The numerical modeling of the antennas is based on surface discretization, using triangular finite element cells. The matrix Z^{KL} depends on the structure geometry of the ensemble of triangles T_K and T_L of the mesh, in which the different triangles summits are C_i^K and C_i^L ($i=1,2,3$). S is the second member, associated with the incident fields.

If we consider the global antenna structure, which contains all the discretized triangles, by considering all the coupling reactions and the second member, the whole linear system of MoM, can be finally defined as follow:

$$[S] = [Z][\Phi] \quad (3.4)$$

Then we can write the whole linear system as below:

$$\begin{bmatrix} S_1 \\ \vdots \\ S_{n-1} \\ S_n \end{bmatrix} = \begin{bmatrix} Z_{1,1} & \cdots & Z_{1,n-1} & Z_{1,n} \\ \vdots & \ddots & \vdots & \vdots \\ Z_{n-1,1} & \cdots & Z_{n-1,n-1} & Z_{n-1,n} \\ Z_{n,1} & \cdots & Z_{n,n} & Z_{n,n} \end{bmatrix} \begin{bmatrix} J_1 \\ \vdots \\ J_{n-1} \\ J_n \end{bmatrix} \quad (3.5)$$

$[Z]$ is an $n \times n$ symmetrical matrix, where n is the number of degrees of freedom of the antenna structure. For each degree of freedom, we compute the coupling reaction between others and itself, and the second member.

3.2 Reaction Matrix Z

If we consider the sub-linear system related to triangles T_K and T_L as written in equation (3.3), the combination of matrix elements $[Z^{KL}]$ is a 6×6 symmetrical one, and composed by 6 degrees of freedom, given by triangle

T_K and T_L respectively. The elements of $[Z^{KL}]$ are placed at different location within the global matrix, as the matrix element is ranged according to the arrangement of fluxes. The sub-matrix $[Z_{ee}^{KL}]$ denotes the coupling reaction given by electric-electric currents, $[Z_{em}^{KL}]$ by electric-magnetic currents, $[Z_{me}^{KL}]$ by magnetic- electric currents, and $[Z_{mm}^{KL}]$ by magnetic-magnetic currents. We hav

$$[Z^{KL}]_{C \times S} = \begin{bmatrix} [Z_{ee}^{KL}]_{C \times S} & [Z_{em}^{KL}]_{C \times S} \\ [Z_{me}^{KL}]_{C \times S} & [Z_{mm}^{KL}]_{C \times S} \end{bmatrix} \quad (3.6)$$

where C denotes the number of Cartesian coordinates, S the number of triangle vertices, e is the electric reaction, m the magnetic reaction. In our system, C and S are equal to 3.

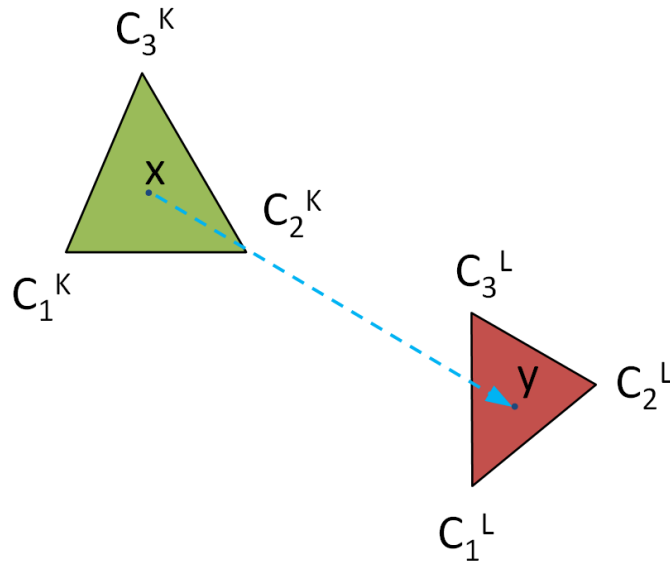


Figure 3.2: Coupling reaction between triangles K and L

We first define all the geometric variables related to triangles T_K and T_L in equation (3.7). In Figure 3.2, we describe the geometric relationship between triangles T_K and T_L , and x and y are the points defined in the triangle T_K and T_L respectively.

$$\begin{aligned}\bar{r} &= (\overline{y-x}), \quad r = \|\overline{y-x}\| \quad \bar{x}, \bar{y} \in T_K, T_L \in \mathfrak{R}^3 \\ \bar{x} &= [x_1, x_2, x_3], \quad \bar{y} = [y_1, y_2, y_3] \\ \bar{C}_s^T &= C_{cs}^T = [C_{1s}^T, C_{2s}^T, C_{3s}^T] \in \mathfrak{R}^3, \quad c, s = 1, 2, 3\end{aligned}\tag{3.7}$$

where:

c is the Cartesian coordinate index
s is the vertex index number

Then, we define the matrix by terms of electric and magnetic properties as follows:

$$\begin{aligned}[Z_{ee}^{KL}]_{C \times S} &= \mu [R_{ee}^{KL}]_{C \times S} I_{se_{cs}} \\ [Z_{em}^{KL}]_{C \times S} &= [R_{em}^{KL}]_{C \times S} I_{se_{cs}} \\ [Z_{me}^{KL}]_{C \times S} &= [R_{me}^{KL}]_{C \times S} I_{sm_{cs}} \\ [Z_{mm}^{KL}]_{C \times S} &= \frac{k^2}{\mu} [R_{mm}^{KL}]_{C \times S} I_{sm_{cs}}\end{aligned}\tag{3.8}$$

where μ denotes the magnetic permeability, k the wavenumber of the electromagnetic radiation and I terms is the coupling terms (-1 or +1), related to the degrees of freedom, needed to represent the global reaction matrix. Thereby, using this reference we can explicit these terms as follows:

$$\begin{aligned}R_{1aa}^{KL} &\rightarrow R_{ee}^{KL}, R_{mm}^{KL} \\ &\text{represented by the same kind of electric or magnetic currents, ee or mm} \\ R_{2ab}^{KL} &\rightarrow R_{em}^{KL}, R_{me}^{KL} \\ &\text{represented by the different kind of electric or magnetic currents, em or me}\end{aligned}\tag{3.9}$$

For sake of completeness, we can define the A, D, T, F operator expressions:

$$\begin{aligned}A^{KL}(G) &= \oint_{T_K} \oint_{T_L} G(\bar{x}, \bar{y}) \left(\bar{a}^{-L}(\bar{y}) \cdot \bar{a}^{-K}(\bar{x}) \right) dy dx \\ D^{KL}(G) &= H_K H_L \oint_{T_K} \oint_{T_L} G(\bar{x}, \bar{y}) dy dx \\ T^{KL}(G) &= \oint_{T_K} \oint_{T_L} \left(\bar{\nabla}_{\bar{y}} G(\bar{x}, \bar{y}) \times \bar{a}^{-L}(\bar{y}) \right) \cdot \bar{b}^{-K}(\bar{x}) dy dx\end{aligned}\tag{3.10}$$

where:

$G = \frac{e^{jkr}}{r}$, $r = \ \overline{y-x}\ $
--

We can define the extended form of basis function with $\bar{\alpha}$ and $\bar{\beta}$ for the triangle T_K and T_L :

$$\begin{aligned} \left[\Theta^K(\bar{x}) \right] &= \bar{\alpha}^K = \bar{\beta}^K = \left[H_K(\bar{C}_3x) \middle| H_K(\bar{C}_1x) \middle| H_K(\bar{C}_2x) \right] \\ \left[\Theta^L(\bar{y}) \right] &= \bar{\alpha}^L = \bar{\beta}^L = \left[H_L(\bar{C}_3y) \middle| H_L(\bar{C}_1y) \middle| H_L(\bar{C}_2y) \right] \\ \left[\Delta^{KL}(\bar{x}, \bar{y}) \right] &= \left[\left(\bar{\nabla}_{\bar{y}} G(\bar{x}, \bar{y}) \times \bar{a}^L(\bar{y}) \right) \cdot \bar{b}^K(\bar{x}) \right] \end{aligned} \quad (3.11)$$

$$\text{where: } \boxed{H_T = \frac{1}{2\Lambda_T}, \Lambda_T \text{ is the surface of triangle T}}$$

If we suppose:

$$\begin{aligned} \left[\Theta^K(\bar{x}) \right] &= H_K \left[\left(\bar{C}_3x \right) \middle| \left(\bar{C}_1x \right) \middle| \left(\bar{C}_2x \right) \right] = H_K \left[B^K(\bar{x}) \right] \\ \left[\Theta^L(\bar{y}) \right] &= H_L \left[\left(\bar{C}_3y \right) \middle| \left(\bar{C}_1y \right) \middle| \left(\bar{C}_2y \right) \right] = H_L \left[B^L(\bar{y}) \right] \\ \text{where: } \boxed{ \begin{aligned} B^K(\bar{x}) &= \left[\left(\bar{C}_3x \right) \middle| \left(\bar{C}_1x \right) \middle| \left(\bar{C}_2x \right) \right] \\ B^L(\bar{y}) &= \left[\left(\bar{C}_3y \right) \middle| \left(\bar{C}_1y \right) \middle| \left(\bar{C}_2y \right) \right] \end{aligned} } \end{aligned} \quad (3.12)$$

$$\phi(r) = G(r) = \frac{e^{jkr}}{r}$$

$$\psi(r) = \frac{\partial \phi(r)}{\partial r} = (jkr - 1) \frac{e^{jkr}}{r^3}$$

$$\bar{\nabla} G(r) = \bar{\nabla} \phi(r) = \psi(r) \cdot r$$

2)

We obtain:

$$\begin{aligned}
 \left[\Delta^{KL}(\bar{x}, \bar{y}) \right]_{cs} &= \psi(r) \cdot \bar{r} \times H_L \left[B^L(\bar{y}) \right]_s \cdot H_K \left[B^K(\bar{x}) \right]_c \\
 &= \psi(r) \left\{ H_K \left[B^K(\bar{x}) \right]_c \times H_L \left[B^L(\bar{y}) \right]_s \right\} \cdot \bar{r} \\
 &= H_K H_L \psi(r) \left[\Omega^{KL}(\bar{x}, \bar{y}) \right]_{cs} \tag{3.13} \\
 \left[\Omega^{KL}(\bar{x}, \bar{y}) \right]_{cs} &= \det \left(\text{col}_s \left[B^L(\bar{y}) \right] \mid \text{col}_c \left[B^K(\bar{x}) \right] \mid \left[\bar{y} - \bar{x} \right] \right) \\
 \text{where: } & \boxed{\left[B^T(\bar{w}) \right]_i = \text{col}_i \left[B^T(\bar{w}) \right]}
 \end{aligned}$$

We can define a simpler formula for A , D , T operators as follows:

$$\begin{aligned}
 \left[A^{KL}(\phi) \right]_{cs} &= H_K H_L \iint_{T_K T_L} \phi(x, y) \left[B^K(x) \right]_c \left[B^L(y) \right]_s dy dx \\
 \left[D^{KL}(\phi) \right]_{cs} &= H_K H_L \iint_{T_K T_L} \phi(x, y) dy dx \\
 \left[T^{KL}(\psi) \right]_{cs} &= H_K H_L \iint_{T_K T_L} \psi(x, y) \left[\Omega^{KL}(x, y) \right]_{cs} dy dx \tag{3.14}
 \end{aligned}$$

where: $c, s = 1, 2, 3$
 $c =$ Cartesian coordinates index
 $s =$ triangle vertex index

Until now, we have defined the kernel of the coupling reactions between two triangles T_K and T_L , we can express the formulas using the operators A , D , T :

$$\begin{aligned}
 \left[Z_{ee}^{KL} \right]_{C \times S} &= \mu \left\{ \left[A^{KL}(\phi) \right]_{cs} - \frac{4}{k^2} \left[D^{KL}(\phi) \right]_{cs} \right\} I_{se_{cs}} \\
 &= \mu \left\{ \left[A^{KL}(\phi) \right]_{cs} + \left[D^{KL}(-4k^{-2}\phi) \right]_{cs} \right\} I_{se_{cs}} \\
 \left[Z_{em}^{KL} \right]_{C \times S} &= \left[T^{KL}(\psi) \right]_{cs} I_{se_{cs}} \\
 \left[Z_{me}^{KL} \right]_{C \times S} &= \left[T^{KL}(\psi) \right]_{cs} I_{sm_{cs}} \tag{3.15} \\
 \left[Z_{mm}^{KL} \right]_{C \times S} &= \frac{k^2}{\mu} \left\{ \left[A^{KL}(\phi) \right]_{cs} - \frac{4}{k^2} \left[D^{KL}(\phi) \right]_{cs} \right\} I_{sm_{cs}} \\
 &= \frac{1}{\mu} \left\{ \left[A^{KL}(k^2\phi) \right]_{cs} - 4 \left[D^{KL}(\phi) \right]_{cs} \right\} I_{sm_{cs}}
 \end{aligned}$$

By defining the four kernel expressions,

$$\begin{aligned}\phi &= \frac{e^{jkr}}{r}, & \psi &= (jkr - 1) \frac{e^{jkr}}{r^3}, \\ \Gamma &= -\frac{4}{k^2} \frac{e^{jkr}}{r}, & \chi &= k^2 \frac{e^{jkr}}{r}\end{aligned}\tag{3.16}$$

We finally obtain the discrete expressions for the $[Z_{xx}^{KL}]$

$$\begin{aligned}[Z_{ee}^{KL}]_{C \times S} &= \mu \left\{ [A^{KL}(\phi)]_{cs} + [D^{KL}(\Gamma)]_{cs} \right\} I_{se_{cs}} \\ [Z_{em}^{KL}]_{C \times S} &= [T^{KL}(\psi)]_{cs} I_{se_{cs}} \\ [Z_{me}^{KL}]_{C \times S} &= [T^{KL}(\psi)]_{cs} I_{sm_{cs}} \\ [Z_{mm}^{KL}]_{C \times S} &= \frac{1}{\mu} \left\{ [A^{KL}(\chi)]_{cs} - 4 [D^{KL}(\phi)]_{cs} \right\} I_{sm_{cs}}\end{aligned}\tag{3.17}$$

3.3 Source Vector Definition

We first define an electric dipole as a source for the scattering computation. The source vector of the linear system takes into account the sources defined inside the analysis domain. The reaction between the source and the discrete triangle (metallic or dielectric) is considered. We then obtain a vector S_K .

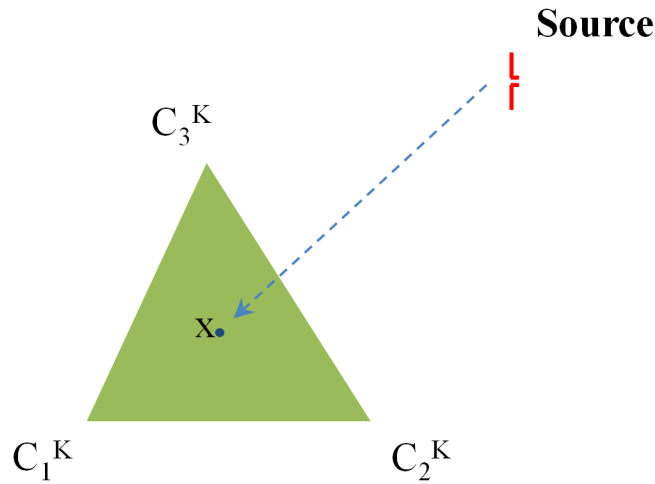


Figure 3.3: Source Vector

Source vector Dipole: The source vector is considered as the reaction between an incident dipole D_K in free space and a single triangle T_K of a metallic or dielectric mesh of a discretized structure. We can write the coupling reaction vector as:

$$[S^K]_{2C \times 1} = \begin{bmatrix} [S_e^K]_{2C \times 1} \\ [S_m^K]_{2C \times 1} \end{bmatrix} \quad (3.18)$$

where:

$C = 3$, number of the cartesian coordinates
 $K =$ triangle index
 $e =$ electric reaction
 $m =$ magnetic reaction

Suppose we have N discrete triangles in the whole domain, the source vector S should have $6*N$ rows in total. It can be represented as:

$$[S] = \begin{bmatrix} [S^1]_6 \\ \vdots \\ [S^K]_6 \\ \vdots \\ [S^N]_6 \end{bmatrix} \quad (3.19)$$

We define all the geometry variables for triangle T_K and dipole D_K :

$$\begin{aligned} \bar{r} &= (\overline{x - y^D}), \quad r = \|\overline{x - y^D}\| \quad \bar{x} \in T_K \in \mathfrak{R}^3, \bar{y}^D \in T_K \in \mathfrak{R}^3 \\ \bar{x} &= [x_1, x_2, x_3], \quad \bar{y}^D = [y_1^D, y_2^D, y_3^D] \\ \bar{C}_s^K &= C_{cs}^K = [C_{1s}^K, C_{2s}^K, C_{3s}^K] \in \mathfrak{R}^3, \quad c, s = 1, 2, 3 \end{aligned} \quad (3.20)$$

where:

c is the Cartesian coordinate index
 s is the vertex index number

The terms of vector S_K can be defined as follows:

$$\begin{aligned} [S_e^K(\bar{m}, y^D)]_c &= -\mu \oint_{T_K} \phi(\bar{x}, y^D) \left\{ [\Theta^K(\bar{x})]_c \bar{m}_i(\bar{x}, y^D) \right. \\ &\quad \left. + \frac{1}{k \|\overline{x - y^D}\|} \left(j - \frac{1}{k \|\overline{x - y^D}\|} \right) \left(2 [\Theta^K(\bar{x})]_c \bar{m}^D \right. \right. \\ &\quad \left. \left. - 3 [\Theta^K(\bar{x})]_c \bar{m}_i(\bar{x}, y^D) \right) \right\} dx \\ [S_m^K(\bar{m}, y^D)]_c &= -\mu \oint_{T_K} \psi(\bar{x}, y^D) [\varepsilon^K(\bar{x}, y^D)]_c dx \end{aligned} \quad (3.21)$$

$$\left[\varepsilon^K \left(\begin{array}{c} \bar{x} \\ \bar{y} \end{array} \right) \right]_c = \det \left(\text{col}_c \left[\Theta^L(\bar{y}) \right] \left| \begin{array}{c} \bar{m} \\ \bar{r} \end{array} \right. \right)$$

where: $\bar{m} = \begin{bmatrix} \bar{m}_1 & \bar{m}_2 & \bar{m}_3 \end{bmatrix}$, dipole D with dipole moment \bar{m}

$$\bar{m}_t \left(\begin{array}{c} \bar{x} \\ \bar{y} \end{array} \right) = \bar{m} \cdot \left[\frac{\bar{r}}{\|\bar{r}\|} \right] \cdot \left[\frac{\bar{r}}{\|\bar{r}\|} \right], \text{ dipole D transversal dipolar moment } \bar{m}_t$$

We can reduce the term ε^K as:

$$\left[\varepsilon^K \left(\begin{array}{c} \bar{x} \\ \bar{y} \end{array} \right) \right]_c = \det \left(\text{col}_c \left[\Theta^L(\bar{y}) \right] \left| \begin{array}{c} \bar{m} \\ \bar{r} \end{array} \right. \right) = H_K \left[\Upsilon^K \left(\begin{array}{c} \bar{x} \\ \bar{y} \end{array} \right) \right]_c \quad (3.22)$$

$$\text{with: } \left[\Upsilon^K \left(\begin{array}{c} \bar{x} \\ \bar{y} \end{array} \right) \right]_c = \det \left(\text{col}_c \left[B^K(\bar{x}) \right] \left| \begin{array}{c} \bar{m} \\ \bar{r} \end{array} \right. \right)$$

The reduced form of the source vector can be written as:

$$\begin{aligned}
 \left[S_e^K \left(\begin{array}{c} \bar{m} \\ \bar{y} \end{array} \right) \right]_c &= -\mu H_K \oint_{T_K} \phi \left(\begin{array}{c} \bar{x} \\ \bar{y} \end{array} \right) \left\{ \left[B^K(\bar{x}) \right]_c \bar{m}_t \left(\begin{array}{c} \bar{x} \\ \bar{y} \end{array} \right) \right. \\
 &\quad \left. + \frac{1}{k \|\bar{x} - \bar{y}^D\|} \left(j - \frac{1}{k \|\bar{x} - \bar{y}^D\|} \right) \left(2 \left[B^K(\bar{x}) \right]_c \bar{m} \right. \right. \\
 &\quad \left. \left. - 3 \left[B^K(\bar{x}) \right]_c \bar{m}_t \left(\begin{array}{c} \bar{x} \\ \bar{y} \end{array} \right) \right) \right\} dx \\
 \left[S_m^K \left(\begin{array}{c} \bar{m} \\ \bar{y} \end{array} \right) \right]_c &= -\mu H_K \oint_{T_K} \psi \left(\begin{array}{c} \bar{x} \\ \bar{y} \end{array} \right) \left[\Upsilon^K \left(\begin{array}{c} \bar{x} \\ \bar{y} \end{array} \right) \right]_c dx
 \end{aligned} \quad (3.23)$$

3.4 Reaction Matrix Discretization

From a computational point of view, we need to discretize A , D , T operators, and $[Z_{xx}^{KL}]$ term. We use a seven-point Gauss discretization method to discretize all the terms.

We define the normalized Gauss method weights γ_T for a genetic discretization point defined inside the triangle T :

$$\gamma_w = \alpha_w \Lambda_T = \frac{\alpha_w}{2H_T} \quad (3.24)$$

where: α_w is non-normalized Gauss weight for the w point

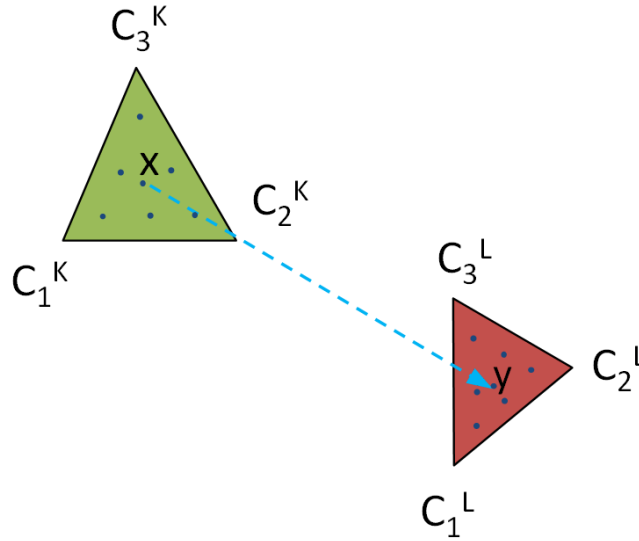


Figure 3.4: Reaction Matrix discretization

In figure 3.4, we apply a seven-Gauss method to the triangle T_K and T_L . Thereafter, we can write the discretized form of a generic Green's function kernel as:

$$G(\bar{x}, \bar{y}) = \sum_K \sum_L \gamma_K \gamma_L G(\bar{x}_K, \bar{y}_L) = \frac{1}{4H_K H_L} \sum_K \sum_L \gamma_K \gamma_L G(\bar{x}_K, \bar{y}_L) \quad (3.25)$$

According to the equation (3.14), the A , D , T operators and $[Z_{xx}^{KL}]$ terms can be discretized as follows:

$$\begin{aligned}
 [A^{KL}(\mathbf{g}_1)]_{cs} &= H_K H_L \frac{1}{4H_K H_L} \sum_k \sum_l \alpha_k \alpha_l \mathbf{g}_1(\bar{x}_k, \bar{y}_l) [B^K(\bar{x}_k)]_c^t [B^L(\bar{y}_l)]_s \\
 [D^{KL}(\mathbf{g}_2)]_{cs} &= H_K H_L \frac{1}{4H_K H_L} \sum_k \sum_l \alpha_k \alpha_l \mathbf{g}_2(\bar{x}_k, \bar{y}_l) \\
 [T^{KL}(\mathbf{g}_3)]_{cs} &= H_K H_L \frac{1}{4H_K H_L} \sum_k \sum_l \alpha_k \alpha_l \mathbf{g}_3(\bar{x}_k, \bar{y}_l) [\Omega^{KL}(\bar{x}_k, \bar{y}_l)]_{cs}
 \end{aligned} \tag{3.26}$$

$$\text{where: } \begin{cases} \mathbf{g}_1(\bar{x}_k, \bar{y}_l) = \begin{cases} \phi(\bar{x}_k, \bar{y}_l) \\ \chi(\bar{x}_k, \bar{y}_l) \end{cases}, \text{ along with } \mathbf{g}_2(\bar{x}_k, \bar{y}_l) = \begin{cases} \Gamma(\bar{x}_k, \bar{y}_l) \\ \phi(\bar{x}_k, \bar{y}_l) \end{cases} \\ \mathbf{g}_3(\bar{x}_k, \bar{y}_l) = \Psi(\bar{x}_k, \bar{y}_l) \end{cases}$$

The reduced form can be written as:

$$\begin{aligned}
 [A^{KL}(\mathbf{g}_1)]_{cs} &= \frac{1}{4} \sum_k \sum_l \alpha_k \alpha_l \mathbf{g}_1(\bar{x}_k, \bar{y}_l) [B^K(\bar{x}_k)]_c^t [B^L(\bar{y}_l)]_s \\
 [D^{KL}(\mathbf{g}_2)]_{cs} &= \frac{1}{4} \sum_k \sum_l \alpha_k \alpha_l \mathbf{g}_2(\bar{x}_k, \bar{y}_l) \\
 [T^{KL}(\mathbf{g}_3)]_{cs} &= \frac{1}{4} \sum_k \sum_l \alpha_k \alpha_l \mathbf{g}_3(\bar{x}_k, \bar{y}_l) [\Omega^{KL}(\bar{x}_k, \bar{y}_l)]_{cs}
 \end{aligned} \tag{3.27}$$

The discretized form for the term $[Z_{xx}^{KL}]$ can be written as:

$$\begin{aligned}
 [Z_{ee}^{KL}]_{CS} &= \mu \left\{ [A^{KL}(\phi)]_{cs} + [D^{KL}(\Gamma)]_{cs} \right\} I_{se_{cs}} \\
 [Z_{em}^{KL}]_{CS} &= [T^{KL}(\psi)]_{cs} I_{se_{cs}} \\
 [Z_{me}^{KL}]_{CS} &= [T^{KL}(\psi)]_{cs} I_{sm_{cs}} \\
 [Z_{mm}^{KL}]_{CS} &= \frac{1}{\mu} \left\{ [A^{KL}(\chi)]_{cs} - 4 [D^{KL}(\phi)]_{cs} \right\} I_{sm_{cs}}
 \end{aligned} \tag{3.28}$$

3.5 Source Vector Discretization

For the source vector, in order to implement numerical computation, we need also to discretize the source vector. The method of discretization is based on the same seven-point Gauss discretization method. (Shown in Figure 3.5)

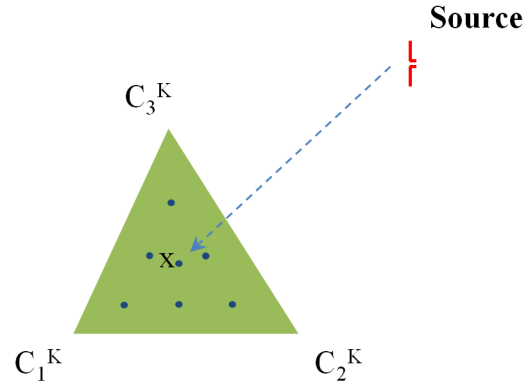


Figure 3.5: Source vector discretization

By applying the discretization method, we can obtain the reduced form for the source vector terms:

$$\begin{aligned}
 \left[S_e^K \left(\begin{matrix} -D & -D \\ m & y \end{matrix} \right) \right]_c &= -\frac{\mu}{2} \sum_k \alpha_k g_1 \left(\begin{matrix} - & -D \\ x_k & y \end{matrix} \right) \left\{ \left[B^K \left(\begin{matrix} - \\ x_k \end{matrix} \right) \right]_c \begin{matrix} -D \\ m_t \end{matrix} \left(\begin{matrix} - & -D \\ x_k & y \end{matrix} \right) \right. \\
 &\quad + \frac{1}{k \|x_k - y^D\|} \left(j - \frac{1}{k \|x_k - y^D\|} \right) \left(2 \left[B^K \left(\begin{matrix} - \\ x_k \end{matrix} \right) \right]_c \begin{matrix} -D \\ m \end{matrix} \right. \\
 &\quad \left. \left. - 3 \left[B^K \left(\begin{matrix} - \\ x_k \end{matrix} \right) \right]_c \begin{matrix} -D \\ m_t \end{matrix} \left(\begin{matrix} - & -D \\ x_k & y \end{matrix} \right) \right\} \right. \\
 \left[S_m^K \left(\begin{matrix} -D & -D \\ m & y \end{matrix} \right) \right]_c &= -\frac{\mu}{2} \sum_k \alpha_k g_3 \left(\begin{matrix} - & -D \\ x_k & y \end{matrix} \right) \left[\Upsilon^K \left(\begin{matrix} - & -D \\ x_k & y \end{matrix} \right) \right]_c
 \end{aligned} \tag{3.29}$$

where:

$$\begin{cases} g_1 \left(\begin{matrix} - & -D \\ x_k & y \end{matrix} \right) = \phi \left(\begin{matrix} - & -D \\ x_k & y \end{matrix} \right) \\ g_3 \left(\begin{matrix} - & -D \\ x_k & y \end{matrix} \right) = \phi \left(\begin{matrix} - & -D \\ x_k & y \end{matrix} \right) \end{cases}$$

CHAPTER 4: OPTIMIZATION TECHNIQUES

Global and local optimization algorithms are broadly divided into deterministic and stochastic. In this chapter, starting from the concept of global and local optimization, we introduce several deterministic and stochastic optimization methods, and discuss the advantages and weak points of each one.

4.1 Global and Local Optimization

Normally, most of optimization techniques focus on search and optimization problems associated with minimizing a cost function $F = F(\Omega)$. We can define the solution set for an optimization problem:

$$X^* = \arg \min_{x \in X} F(x) = \{x^* \in X : F(x^*) \leq F(x) \text{ for all } x \in X\} \quad (4.1)$$

Where x is a p -dimensional vector of parameters that being adjusted and $X \subseteq \mathbb{R}^p$ is the domain for x , which represents constraints on allowable values for x . The statement $\arg \min_{x \in X} F(x)$ illustrates that X^* is the set of values $x = x^*$ (x the “argument” in “arg min”) that minimizes $F(x)$ subject to x^* satisfying the constraints represented in the set X . [49]

Figure 4.1 illustrates a simple distinction of local and global minima for a one-dimensional optimization problem. When the optimal value equals to x_{local} , the value of cost function is $F(x_{local})$, however, it is not the lowest of cost function from the global viewpoint, comparing with a global optimal point x^* , where the value of cost function is $F(x^*)$.

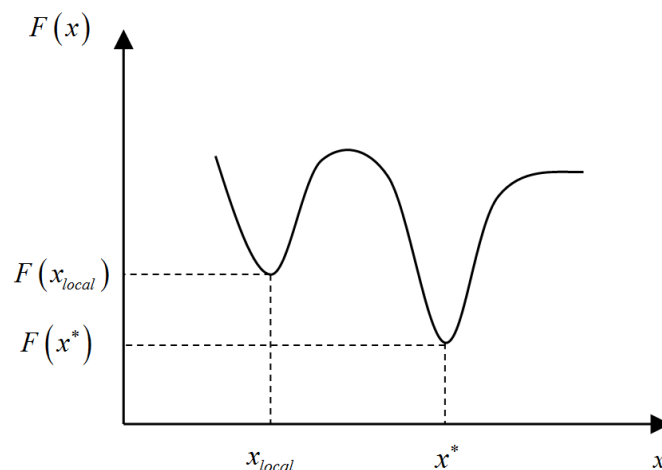


Figure 4.1: Local and global minima

The difference between global and local optimization is one of the major distinction in optimization techniques. When considering all other factors in the optimization problems equally, one would always hope to find a globally optimal solution, which can provide a lowest value of cost function, and normally a better similarity comparing with the goal. While in practice, especially for nonlinear problems, the cost function always has a large number of local minima. Finding an arbitrary local optimum is relatively straightforward by using classical local optimization methods, and finding the global minimum of a function is far more difficult. In this situation, a global solution may not be always available and sometimes a local minimum is better than any in its vicinity, but can be an acceptable result.

When we consider the concept of local optimization, it means that the optimization procedure attempts to find a local minimum, and obtaining the global minimum cannot be guaranteed. Local optimization algorithms generally depend on derivatives of the cost function and constraints to aid in the search procedure. Thus, there are strict requirements for the input information.

4.2 Stochastic Method

Stochastic methods normally can locate a global optimum faster than deterministic ones and only offer a guarantee in probability. In additional, stochastic methods can adapt better to unknown formulations and extremely ill-behaved functions, whereas deterministic methods usually rely on some analytical assumptions about the problem formulation and its analytical properties. However, in general search and optimization, it is very difficult to develop automated methods for indicating when the algorithm is close enough to the solution that it can be stopped, and it cost a considerable computation

for finding optimal solutions. We introduce some popular stochastic methods below.

4.2.1 Genetic Algorithms

The genetic algorithm was first introduced by Holland (1975) [52], and has become a popular method for solving large optimization problems with multiple local optima. In a genetic algorithm, a population of candidate solutions to an optimization problem is evolved toward better generations. Each candidate solution has a set of properties, which are represented in binary, and considered as 0s and 1s. The evolution usually starts from a population of randomly generated individuals, and then for each generation or iteration, the fitness of every individual in the population is evaluated stochastically by selecting the multiple individuals from the current population. When a solution is found that satisfies minimum criteria for the population, the algorithm terminates and we can obtain optimal solution.

However, in order to find the optimal solution for complex high-dimensional and multimodal problems, very expensive cost function evaluations are often required. When we solve the practical problems such as structural optimization problems, typical optimization methods may not be able to deal with it. Moreover, a genetic algorithm needs a considerable number of computations and iterations before finding the convergence towards the optimum.

4.2.2 Particle Swarm Optimization

Particle swarm optimization (PSO) is a population based stochastic optimization technique developed by Eberhart and Kennedy in 1995 [53]. It is a computational method that optimizes a problem by iteratively trying to improve a candidate solution with regards to a given measure of quality.

PSO shares many similarities with evolutionary computation techniques such as Genetic Algorithms. The optimization system is randomly initialized with a population of solutions and searches for optima by updating generations. PSO optimizes a problem by moving the potential solutions, which are called the particles, around in the search-space according to simple mathematical formulae over the particle's position and velocity.

PSO is a metaheuristic method, which makes few or no assumption about the problem being optimized and can search very large spaces of candidate solutions. However, it cannot guarantee an optimal solution is ever found, and is easily trapped into a local minimum.

4.2.3 Simulated Annealing

Simulated annealing (SA) is also a generic probabilistic metaheuristic method proposed by Kirkpatrick, Gelett and Vecchi (1983) [54] and Cerny (1985) [55]. It is for the global optimization problem of locating a good approximation to the global optimum of a given cost function in a large search space, which is often discrete.

The principle of simulated annealing is typically described in terms of thermodynamics. Simulated annealing is a process where the temperature is reduced slowly. Starting from a random search at high temperature eventually, it becomes pure greedy descent as it approaches zero temperature. The randomness should tend to jump out of local minima and find regions that have a low heuristic value. Simulated annealing maintains a current assignment of values to variables. At each step, it picks a variable at random, and then picks a value at random.

As a kind of probabilistic metaheuristic method, simulated annealing algorithm also needs a huge number of computations and iterations for finding the convergence towards the optimum.

4.2.4 Ant Colony Optimization

Ant colony optimization algorithm (ACO) is a probabilistic technique for solving computational problems, proposed by Marco Dorigo in 1992 [56]. It is an algorithm for finding optimal paths that is based on the behaviour of ants searching for food. At first, the ants wander randomly. When an ant finds a source of food, it walks back to the colony leaving pheromones that show the path has food. When other ants come across the pheromones, they follow the path with a certain probability. As more ants find the path, it gets stronger until there are a couple streams of ants traveling to various food sources near the colony.

Because the ant-colony works on a very dynamic system, the ant colony algorithm works very well in graphs with changing topologies, but also needs a considerable number of computations for finding the optimum.

4.3 Deterministic Method

Normally deterministic methods provide a theoretical guarantee of locating the global minimum, or at least a local one, and assume that perfect information,

which is used to determine the search direction in a deterministic manner at every step of the algorithm, is available for the cost function. However, in many practical problems, there are also some constraints for deterministic methods. For example, the information used to determine the search directions is not always available.

4.3.1 Shape Gradients Calculation

When we consider a smooth velocity field V and the family of transformations of the initial domain under the velocity field V :

$$x(0) = x_0 \in \Omega, \quad x'(s) = V(x(s)), \quad T_s(x_0) = x(s), \quad s \geq 0$$

and we also denote

$$\Omega_0 \text{ a } T_s(\Omega_0) = \Omega_s$$

Then, by calculating the differential of the cost functional, we can define that the shape derivative of $F(\Omega)$ at Ω_0 with respect to the shape Ω is the limit of formula

$$dF(\Omega_0; V) = \lim_{s \rightarrow 0} \frac{F(\Omega_s) - F(\Omega_0)}{s} \quad (4.2)$$

(if this limit exists.)

In order to reduce the value of the cost functional, we evolve the boundary of Ω along a direction (gradient line), then the shape gradient can be defined as:

$$dF(\Omega_0; V) = \langle \nabla F, V \rangle_{\partial\Omega_0} \quad (4.3)$$

where ∇F is called the shape gradient.

4.3.2 Shape Optimization Using Shape Gradients

By computing of the derivatives of cost function with respect to the design parameters (if can be defined), shape optimization can be faced using standard optimization methods. For example, the gradient descent method can be used for the optimization procedure for finding especially the local minimum. As an improved method of gradient descent method, conjugate gradient method use conjugate direction instead of the local gradient for going downhill. And the minimum can be reached in far fewer steps than using

gradient descent method. By means of the velocity of Halmilton-Jacobi function [57], which is computed using the shape gradient, the level set method can also be implemented for the shape optimization procedure.

CHAPTER 5: SHAPE GRADIENT

The inverse scattering procedure for optimizing the geometry from imposed radiation patterns or for reconstructing the geometry from measurements, is based on finding a solution (if such a solution exists) that minimizes the cost functional defined as follows:

$$F(\Omega) = \frac{\sum_{s=1}^S \sum_{q=1}^Q \left\| \vec{E}_{s,q}^{meas} - \vec{E}_{s,q}^{comp}(\Omega) \right\|^2}{\sum_{s=1}^S \sum_{q=1}^Q \left\| \vec{E}_{s,q}^{meas} \right\|^2} \quad (5.1)$$

Where $\vec{E}^{comp}(\Omega)$ is the computed scattered field or radiation pattern for a certain geometry Ω and $\vec{E}^{meas}(\Omega)$ is the imposed or measured scattered field or radiation patterns.

In order to minimize the cost functional, we need to compute the differential of the cost functional versus global geometry Ω that requires to determine the differential of the scattered field $\delta \vec{E}^{comp}$:

$$\delta F = \frac{-2 \sum_{s=1}^S \sum_{q=1}^Q \operatorname{Re} \left[\left(\vec{E}_{s,q}^{meas} - \vec{E}_{s,q}^{comp}(\Omega) \right) \cdot \delta \vec{E}_{s,q}^{comp}(\Omega) \right]}{\sum_{s=1}^S \sum_{q=1}^Q \left\| \vec{E}_{s,q}^{meas} \right\|^2} \quad (5.2)$$

We can see that, in order to calculate the derivative of the cost functional, we have to know the derivative of the scattered field versus the geometry.

For the computation of this derivative, five kinds of numerical methods are developed: a discrete form of the gradient, a formulation based on the adjoint method, an analytical expression, nodal point mesh derivation method, and topological shape gradient method.

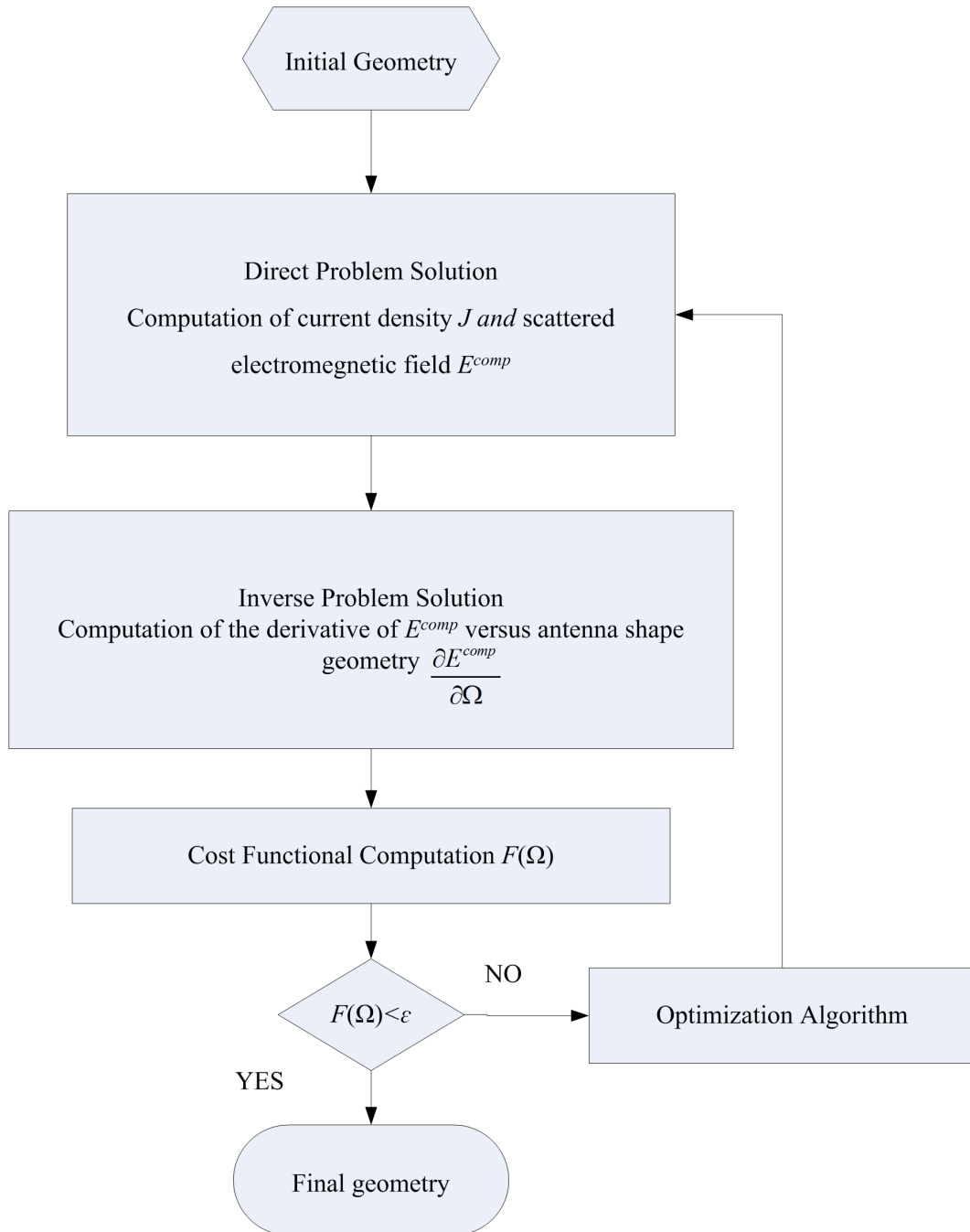


Figure 5.1: Flow chart of optimization procedure

5.1 Discrete Method

The derivative of the scattered field with respect to the geometry can be computed using the central finite difference:

$$\frac{\partial \vec{E}_{s,q}^{\text{comp}}(\Omega)}{\partial \Omega} = \frac{\vec{E}_{s,q}^{\text{comp}}(\Omega + \Delta\Omega) - \vec{E}_{s,q}^{\text{comp}}(\Omega - \Delta\Omega)}{\Delta\Omega \times 2} \quad (5.3)$$

One can see that the derivative is defined with respect to a given geometry difference $\Delta\Omega$, in order to compute the derivative, first the difference of the computed scattered field on geometry $\Omega+\Delta\Omega$ and $\Omega-\Delta\Omega$ is computed, then by dividing two times the geometry difference $\Delta\Omega$, we can get the derivative of the scattered field with respect to the geometry Ω .

5.2 Adjoint Method

We exchange the incident field locations with the measurement point locations, and compute the adjoint current density.

$$\begin{aligned} \delta \vec{E}_{s,q}^{\text{comp}}(\Omega) &= \frac{j}{\omega\mu} \int_{\Omega} (\vec{\nabla} \cdot \vec{J}_s) (\vec{\nabla} \cdot \vec{J}'_q) (\delta \vec{S} \cdot \vec{n}) d\Omega \\ &- j\omega\mu \int_{\Omega} \vec{J}_s \vec{J}'_q (\delta \vec{S} \cdot \vec{n}) d\Omega \end{aligned} \quad (5.4)$$

This formulation is valid when the deformation is along the normal direction \vec{n} .

5.3 Analytical Method

Considering an arbitrary antenna shape, which is meshed by triangles, if we move a point P on the contour to P' , the fluxes connected to the triangle T_1 , T_2 , T_3 would be changed, as well as the terms of the coupling matrix related to these triangles. If we can determine the sensitivity of the scattered field when moving the points on the contour, we can obtain the value of the shape gradient.

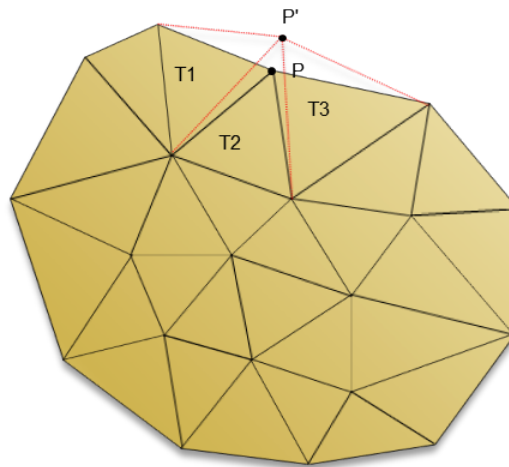


Figure 5.2: Geometry modification when moving point P

If we write a simple expression of computed scattered field as:

$$\mathbf{u}_{E^{s,comp}} = [G][\Phi] \quad (5.5)$$

where $[G]$ denotes Green's matrix, and $[\Phi]$ the current density vector.

We can compute the derivative of the scattered field with respect to the geometry Ω by computing the derivative of Green's matrix and current density vector with respect to the geometry Ω :

$$\frac{\partial E^{s,comp}}{\partial \Omega} = \left[\frac{\partial G}{\partial \Omega} \right] [\Phi] + \left[\frac{\partial \Phi}{\partial \Omega} \right] [G] \quad (5.6)$$

)

We can find the derivative of current density vector Φ with respect to the triangle apexes C_i^K :

$$\frac{\partial \Phi}{\partial C_i^K} = Z^{-1} \left[\frac{\partial S}{\partial C_i^K} - \left(\frac{\partial Z}{\partial C_i^K} \right) \Phi \right] \quad (5.7)$$

This equation shows that, when moving an apex of triangle on edge, in order to compute the derivative of the current density with respect to the mesh, we need to compute the derivative of the reaction matrix and second member with respect to the apex of triangle T_K , respectively.

Given a triangle-meshed surface Ω , for i th apex on the triangle K , the reaction matrix derivative with respect to this triangle apex can be expressed as:

$$\left[\frac{\partial Z}{\partial C_i^K} \right]_{M \times N} = \begin{bmatrix} \left. \frac{\partial Z}{\partial C_i^K} \right|_{11} & \cdots & \left. \frac{\partial Z}{\partial C_i^K} \right|_{1n} \\ \cdots & \cdots & \cdots \\ \left. \frac{\partial Z}{\partial C_i^K} \right|_{m1} & \cdots & \left. \frac{\partial Z}{\partial C_i^K} \right|_{mn} \end{bmatrix} \quad (5.8)$$

Where C_i^K indicates the i th apex on the triangle K , m and n denote the derived element matrix indices. $M \times N$ is the size of reaction matrix.

Similarly, the derivative of the source vector can be expressed as:

$$\left[\frac{\partial S}{\partial C_i^K} \right]_{m \times 1} = \begin{bmatrix} \left. \frac{\partial S}{\partial C_i^K} \right|_1 \\ \vdots \\ \left. \frac{\partial S}{\partial C_i^K} \right|_m \end{bmatrix} \quad (5.9)$$

Considering the sub-linear system, which is related to the single couple of triangles of T_K and T_L , we write it as:

$$[Z^{KL}][\Phi^L] = [S^K] \quad (5.10)$$

We can derive the reaction matrix of the sub-linear system according to the electric and magnetic reactions, which can be written as:

$$[Z^{KL}] = \begin{bmatrix} [Z_{ee}^{KL}] & [Z_{em}^{KL}] \\ [Z_{me}^{KL}] & [Z_{mm}^{KL}] \end{bmatrix} \quad (5.11)$$

For the expression of the derivative of the sub-matrix with respect to the coordinates and the triangle summit, we have:

$$\frac{\partial [Z^{KL}]}{\partial C_{uv}^L} = \begin{bmatrix} \left. \frac{\partial [Z_{ee}^{KL}]}{\partial C_{uv}^L} \right|_{C \times S} & \left. \frac{\partial [Z_{em}^{KL}]}{\partial C_{uv}^L} \right|_{C \times S} \\ \left. \frac{\partial [Z_{me}^{KL}]}{\partial C_{uv}^L} \right|_{C \times S} & \left. \frac{\partial [Z_{mm}^{KL}]}{\partial C_{uv}^L} \right|_{C \times S} \end{bmatrix} \quad (5.12)$$

)

where : C,S=3

C = number of Cartesian coordinates

S = number of triangle summits

e = electric reaction

m = magnetic reaction

The matrix contains four parts of reaction: electric-to-electric, electric-to-magnetic, magnetic-to-electric, magnetic-to-magnetic; u and v are referring to the Cartesian components, and triangle summits of triangle, therefore, the

sub-matrix $\left. \frac{\partial [Z_{\alpha\beta}^{KL}]}{\partial C_{uv}^L} \right|_{C \times S}$ is a 3×3 one.

The gradient of the SR3D reaction matrix for a metallic structure is obtained through the reaction matrix derivative with respect to each summit of the related triangle and direction.

$$\nabla_{C_i^L} [Z^{KL}] = \left(\frac{\partial [Z_{ee}^{KL}]}{\partial C_{xi}^L}, \frac{\partial [Z_{ee}^{KL}]}{\partial C_{yi}^L}, \frac{\partial [Z_{ee}^{KL}]}{\partial C_{zi}^L} \right) \quad (5.13)$$

We apply the R terms from the Rumsey reaction to the reaction matrix derivative with respect to a single couple of triangles T and L. The Z^{KL} derivative can be defined term by term as follows:

$$\begin{aligned} \left. \frac{\partial [Z_{ee}^{KL}]}{\partial C_{uv}^L} \right|_{C \times S} &= \mu \left. \frac{\partial [R_{ee}^{KL}]}{\partial C_{uv}^L} \right|_{C \times S} I_{se_{cs}} \\ \left. \frac{\partial [Z_{em}^{KL}]}{\partial C_{uv}^L} \right|_{C \times S} &= \left. \frac{\partial [R_{em}^{KL}]}{\partial C_{uv}^L} \right|_{C \times S} I_{se_{cs}} \\ \left. \frac{\partial [Z_{me}^{KL}]}{\partial C_{uv}^L} \right|_{C \times S} &= \left. \frac{\partial [R_{me}^{KL}]}{\partial C_{uv}^L} \right|_{C \times S} I_{sm_{cs}} \\ \left. \frac{\partial [Z_{mm}^{KL}]}{\partial C_{uv}^L} \right|_{C \times S} &= \frac{k^2}{\mu} \left. \frac{\partial [R_{me}^{KL}]}{\partial C_{uv}^L} \right|_{C \times S} I_{sm_{cs}} \end{aligned} \quad (5.14)$$

We apply SR3D A, D, T operators, and evolve the formula above:

$$\begin{aligned}
 \left. \frac{\partial [Z_{ee}^{KL}]}{\partial C_{uv}^L} \right|_{C \times S} &= \mu \left\{ \left. \frac{\partial [A^{KL}(\phi)]}{\partial C_{uv}^L} \right|_{C \times S} + \left. \frac{\partial [D^{KL}(\Gamma)]}{\partial C_{uv}^L} \right|_{C \times S} \right\} I_{se_{cs}} \\
 \left. \frac{\partial [Z_{em}^{KL}]}{\partial C_{uv}^L} \right|_{C \times S} &= \left. \frac{\partial [T^{KL}(\Psi)]}{\partial C_{uv}^L} \right|_{C \times S} I_{se_{cs}} \\
 \left. \frac{\partial [Z_{me}^{KL}]}{\partial C_{uv}^L} \right|_{C \times S} &= \left. \frac{\partial [T^{KL}(\Psi)]}{\partial C_{uv}^L} \right|_{C \times S} I_{sm_{cs}} \\
 \left. \frac{\partial [Z_{mm}^{KL}]}{\partial C_{uv}^L} \right|_{C \times S} &= \frac{1}{\mu} \left\{ \left. \frac{\partial [A^{KL}(\chi)]}{\partial C_{uv}^L} \right|_{C \times S} + \left. \frac{\partial [D^{KL}(\phi)]}{\partial C_{uv}^L} \right|_{C \times S} \right\} I_{sm_{cs}}
 \end{aligned} \tag{5.15}$$

Let's now write the derivative of the above-mentioned terms using the new notation:

$$\begin{aligned}
 \left[D_{uv}^L \{ A^{KL}(\mathbf{g}_1) \} \right]_{cs} &= H_K H_L \oint_{T_k} \oint_{T_l} \left\{ D_{uv}^L \left\{ \mathbf{g}_1(\bar{x}, D_{uv}^L \{ \bar{y} \}) \right\} \left[B^K(\bar{x}) \right]_c^t \left[B^L(\bar{y}) \right]_s \right. \\
 &\quad \left. + \mathbf{g}_1(\bar{x}, \bar{y}) \left[B^K(\bar{x}) \right]_c^t D_{uv}^L \left\{ \left[B^L(D_{uv}^L \{ \bar{y} \}) \right]_s \right\} \right\} dx dy \\
 \left[D_{uv}^L \{ A^{KL}(\mathbf{g}_2) \} \right]_{cs} &= H_K H_L \oint_{T_k} \oint_{T_l} D_{uv}^L \left\{ \mathbf{g}_2(\bar{x}, D_{uv}^L \{ \bar{y} \}) \right\} dy dx \\
 \left[D_{uv}^L \{ T^{KL}(\mathbf{g}_3) \} \right]_{cs} &= H_K H_L \oint_{T_k} \oint_{T_l} D_{uv}^L \left\{ \mathbf{g}_3(\bar{x}, D_{uv}^L \{ \bar{y} \}) \right\} \left[\Omega^{KL}(\bar{x}, \bar{y}) \right]_{cs} \\
 &\quad + \mathbf{g}_3(\bar{x}, \bar{y}) D_{uv}^L \left\{ \left[\Omega^{KL}(\bar{x}, D_{uv}^L \{ \bar{y} \}) \right]_{cs} \right\} dy dx
 \end{aligned} \tag{5.16}$$

$$\begin{aligned}
 D_{uv}^L \left\{ g_1 \left(\bar{x}, D_{uv}^L \{y\} \right) \right\} &= \begin{cases} \frac{\partial \phi(\bar{x}, \bar{y})}{\partial [\bar{y}]} D_{uv}^L \left\{ [\bar{y}] \right\} \\ \frac{\partial \chi(\bar{x}, \bar{y})}{\partial [\bar{y}]} D_{uv}^L \left\{ [\bar{y}] \right\} \end{cases} \\
 D_{uv}^L \left\{ g_2 \left(\bar{x}, D_{uv}^L \{y\} \right) \right\} &= \begin{cases} \frac{\partial \Gamma(\bar{x}, \bar{y})}{\partial [\bar{y}]} D_{uv}^L \left\{ [\bar{y}] \right\} \\ \frac{\partial \phi(\bar{x}, \bar{y})}{\partial [\bar{y}]} D_{uv}^L \left\{ [\bar{y}] \right\} \end{cases} \\
 D_{uv}^L \left\{ g_3 \left(\bar{x}, D_{uv}^L \{y\} \right) \right\} &= \frac{\partial \Psi(\bar{x}, \bar{y})}{\partial [\bar{y}]} D_{uv}^L \left\{ [\bar{y}] \right\}
 \end{aligned} \tag{5.17}$$

Similarly, we also have the expression of the derivative of the second member with respect to the summits of triangles.

$$\frac{\partial [S^{KL}]}{\partial C_{uv}^L} = \begin{bmatrix} \frac{\partial [S_e^{KL}]}{\partial C_{uv}^L} \Big|_{C \times 1} \\ \frac{\partial [S_m^{KL}]}{\partial C_{uv}^L} \Big|_{C \times 1} \end{bmatrix} \tag{5.18}$$

$$\begin{aligned}
 [D_{uv}^K \{S_e^K(m^D, y^D)\}]_c &= -\mu H_K \int_{j_k}^k D_{uv}^K \left\{ \phi \left(D_{uv}^K \{x\}, y^D \right) \right\} \left[-[B^K(x)]_c^t m_i^D(x, y^D) \right. \\
 &+ \frac{1}{k \|x - y^D\|} \left(j - \frac{1}{k \|x - y^D\|} \right) \left(2 [B^K(x)]_c^t m^D - 3 [B^K(x)]_c^t m_i^D(x, y^D) \right) \\
 &+ \phi(x, y^D) \left[-D_{uv}^K \left\{ [B^K(D_{uv}^K \{x\})]_c^t \right\} m_i^D(x, y^D) + [B^K(x)]_c^t D_{uv}^K \left\{ m_i^D(D_{uv}^K \{x\}, y^D) \right\} \right. \\
 &+ D_{uv}^K \left\{ \frac{1}{k \|x - y^D\|} \left(j - \frac{1}{k \|x - y^D\|} \right) \right\} \left(2 [B^K(x)]_c^t m^D - 3 [B^K(x)]_c^t m_i^D(x, y^D) \right) \\
 &+ \frac{1}{k \|x - y^D\|} \left(j - \frac{1}{k \|x - y^D\|} \right) \left(2 D_{uv}^K \left\{ [B^K(D_{uv}^K \{x\})]_c^t \right\} m^D \right. \\
 &\left. \left. - 3 D_{uv}^K \left\{ [B^K(D_{uv}^K \{x\})]_c^t m_i^D(x, y^D) - 3 [B^K(x)]_c^t D_{uv}^K \left\{ m_i^D(D_{uv}^K \{x\}, y^D) \right\} \right\} \right) \right\} dx
 \end{aligned} \tag{5.19}$$

$$\left[D_{uv}^K \left\{ S_m^K \left(\overset{-D}{m}, \overset{-D}{y} \right) \right\} \right]_C = -\mu H_K \oint_{T_k} D_{uv}^K \left\{ \Psi \left(D_{uv}^K \left\{ \overset{-}{x}, \overset{-D}{y} \right\} \right) \right\} \left[\Upsilon^K \left(\overset{-}{x}, \overset{-D}{y} \right) \right]_C + \Psi \left(\overset{-}{x}, \overset{-D}{y} \right) D_{uv}^K \left\{ \left[\Upsilon^K \left(D_{uv}^K \left\{ \overset{-}{x}, \overset{-D}{y} \right\} \right) \right]_C \right\} dx \quad (5.20)$$

5.4 Shape Gradient-Based on Topological Deformation

For the shape optimization of reflectarrays or planar antenna arrays, we usually consider 2D metallic antenna structures to obtain approximate solutions instead of 3D realistic structures. In fact, when we consider the shape deformation of antennas in a two-dimensional plane, it is difficult to find the outward-pointing normal. In order to solve this problem, we give a new sense to the shape gradient versus an edge deformation (or transformation) in 3D for metallic layers with limited surfaces. We can use this derived numerical model to study planar structures with the notion of metallic layer with a 2D outward normal direction.

The shape gradient is computed using two different methods: one based on nodal point mesh derivation with an infinitesimal modification of the triangular elements on the contour along the outward normal direction and the other on topological gradient when adding a small triangular element to an edge.

5.4.1 Contour Definition of Shape Geometry

For an arbitrary 2D triangular discretized geometry Ω . Let Ω be a domain of \mathbb{R}^2 , Γ a polyline on the contour of Ω . On the polyline of Γ , we suppose there are n triangular apexes and n edges on the contour of geometry Ω .

We define the set of all the triangular apexes in the domain Ω : $\bigcup_{i=1}^M \{P_i\}$, $i \in \{1, 2, \dots, M\}$.

For the whole triangular domain Ω , we suppose we have N triangles, which can be defined as: $\Omega = \bigcup_{k=1}^N T_k$, $\Omega \in \mathbb{R}^2$, $T_k \cap T_{k'} = \emptyset, k \neq k'$, with $k = 1, 2, \dots, N$. We also define the set of all the apexes by all the triangles in the domain $S_\sigma^k \in \mathbb{P}$ $\sigma = 1, 2, 3; k = 1, 2, \dots, N$, where σ denotes the index of apexes in one triangle.

Therefore, we can define the set of \mathbb{P} as: $\mathbb{P} = \bigcup_{i=1}^M \{P_i\} = \bigcup_{k=1}^N \{S_1^k, S_2^k, S_3^k\}$

$\forall k \in \{1, 2, L, N\}, \forall \sigma \in \{1, 2, 3\}, \exists ! i \in \{1, 2, L, M\}$, which can satisfy $P_i = S_\sigma^k$.

Let I be the function

$$I: \{1, 2, L, N\} \times \{1, 2, 3\} \rightarrow \{1, 2, L, M\}$$

$$I: (k, \sigma) \rightarrow I(k, \sigma): S_\sigma^k = P_{I(k, \sigma)}$$

For the triangular apexes which are on the contour Γ , we define the set

$X^p \in \dot{P}, \forall p \in \{1, 2, L, n\}, \exists ! j \in \{1, 2, L, M\}$, which satisfy $X^p = P_j$

Let $J^\Gamma: \{1, 2, L, n\} \rightarrow \{1, 2, L, M\}$, $J^\Gamma: p \rightarrow J^\Gamma(p): X^p = P_{J^\Gamma(p)}$

Let $\Pi_{TS}: \bar{\sigma} (\{1, 2, L, N\} \rightarrow \{1, 2, 3\})$ be the set of subsets of $\{1, 2, L, N\} \rightarrow \{1, 2, 3\}$.

We define for $P_i \in \dot{P}$, we have $I^{-1}(i) \in \Pi_{TS}$

At each point $p, p \in \{1, 2, L, n\}$, we can associate $\hat{T}_s(p) \in \Pi_{TS}$,

$\hat{T}_s(p) = I^{-1}(J^\Gamma(p))$, where we have $(k, \sigma) \in \hat{T}_s(p)$ and $I(k, \sigma) = J^\Gamma(p)$. It

means that if $(k, \sigma) \in \hat{T}_s(p)$, then X^p is the apex S_σ^k of T_K ($\sigma=1$ or 2 or 3),

and if $(k, \sigma) \in \hat{T}_s(p)$, and $(k, \sigma') \in \hat{T}_s(p)$, then we have $\sigma = \sigma'$

Therefore, we can define the subset $\hat{T}(p)$ of $\{1, 2, L, N\}$, for $k \in \hat{T}(p)$,

$\exists \sigma \in \{1, 2, 3\} (k, \sigma) \in \hat{T}_s(p)$, where $\hat{T}(p)$ is the set of the index of the triangles, which have X^p as an apex.

Let $\hat{n}_T(p)$ be the number of triangles, which have X^p as an apex, we can define at last:

$$\hat{k}_i^p: \{1, 2, L, N\} \rightarrow \hat{T}(p)$$

which indexes the elements of $\hat{T}(p)$.

We can construct that

$$\dot{k}_i^P, P=1,2,L, M, i=1,2,L, \max\left(\hat{n}_T(p)\right)$$

$$\text{with } \dot{k}_i^P = 0, \text{ if } i > \hat{n}_T(p)$$

$$\dot{k}_i^P = k_i^P, \text{ if } i \leq \hat{n}_T(p)$$

5.4.2 Shape Gradient Method Using Nodal Point Mesh Derivation

Suppose P is a nodal point on the contour of the geometry Ω . For this nodal point a certain number of triangles (e.g. T_1, T_2 and T_3 for P_i as shown in Figure 2) are connected to point P . As we have defined before, $\hat{n}_T(p)$ is the number of triangles have P as an apex. $\hat{T}(p)$ is the set of the index of the triangles which have P as an apex.

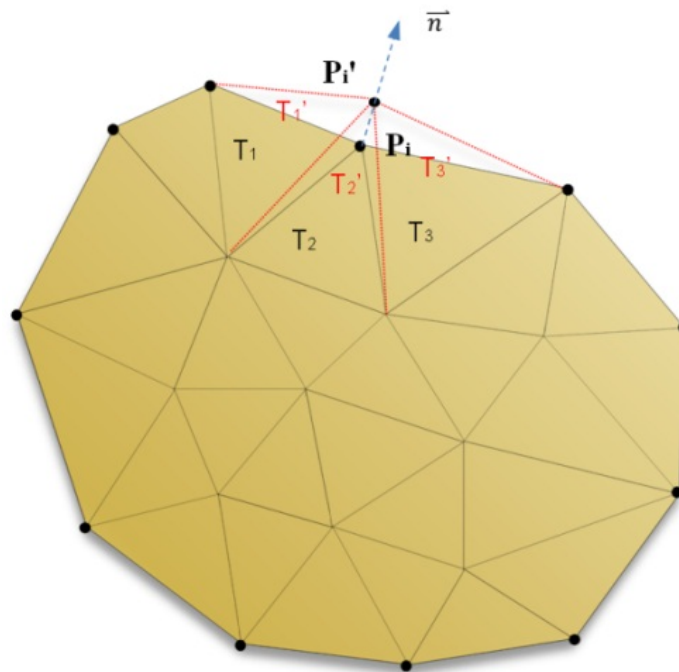


Figure 5.3: Nodal point mesh derivation

When moving this nodal point P_i along the normal direction of the contour to P_i' , we obtain a modified geometry $\Omega + \Delta\Omega$, given by the shape deformation of $\hat{T}(p)$. As illustrate in figure 2, the triangles (T_1, T_2 , and T_3) are changed into (T_1', T_2' , and T_3').

Comparing with the initial shape geometry Ω , the difference is the triangles connected to the point P_i and P'_i . With the new triangular mesh, we compute again the new coupling matrix $[Z_{\Omega+\Delta\Omega}]$, then solve the new linear system:

$$[Z_{\Omega+\Delta\Omega}].[\Phi_{\Omega+\Delta\Omega}] = [S_{\Omega+\Delta\Omega}] \quad (5.21)$$

With the new fluxes $[\Phi_{\Omega+\Delta\Omega}]$, we can obtain the new electric field $\vec{E}^{comp}(\Omega + \Delta\Omega)$ directly. Using finite difference method, we can compute the differential of the field with respect to the moving point P_i along the normal direction

$$\delta \dot{E}^{comp} = \dot{E}^{comp}(\Omega + \Delta\Omega) - \dot{E}^{comp}(\Omega) \quad (5.22)$$

5.4.3 Topological Gradient method

For an arbitrary 2D triangular discretized geometry Ω , we assume there are n triangular edges on the contour Γ .

Let $\left\{ \bigcup_{i=1}^n L_i \right\}$ be the set of triangular edges on the contour, we also define the set of all the triangular edges by all the triangles in the domain $U_\rho^k \in \dot{P} \quad \rho = 1, 2, 3; \quad k = 1, 2, \dots, N$, where ρ denotes the index of flux in one triangle.

Let the linear system $[Z].[\Phi] = [S]$ be associated with an initial geometry Ω .

We modify the initial geometry Ω to a new geometry $\Omega + \Delta\Omega$ by adding a triangle T' with small height δh (with $\delta h \ll \lambda$, where λ is the wavelength) to a triangle T on the edge of the contour (Fig. 2.3). The flux through the edge of the contour is null in the initial geometry but there is now a new unknown flux φ to determine on the common edge between T and T' . The fluxes on the two other edges of triangle T' are null as they belong to the new contour.

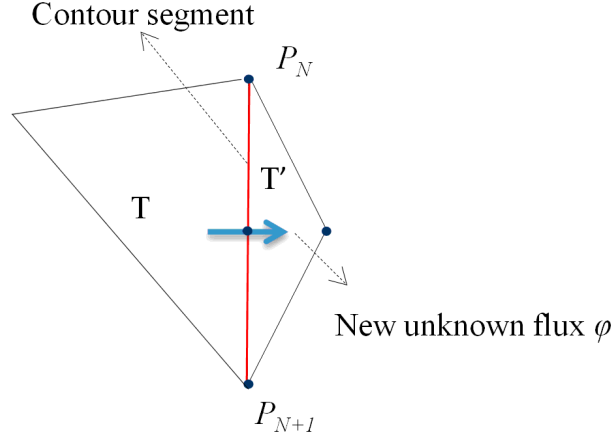


Figure 5.4: Topological modification

$$M_{ij} = \int_{T_k^i \cup T_k^i} \int_{T_l^j \cup T_l^j} \mu(x)_{\sigma_c^{k^i}(k^i, k^i)} \sigma_c^{k^i}(k^i, k^i) \Phi(x, y) \mu(y)_{\sigma_c^{l^j}(l^j, l^j)} \sigma_c^{l^j}(l^j, l^j) dx dy \quad (5.23)$$

Where $\mu_{\sigma\sigma'}^{kk'}$ is the basic finite element function with triangle $T_k^i \cup T_k^i$

$$\begin{aligned} \mu_{\sigma\sigma'}^{kk'}(x) &= I_\sigma \Theta^k(x) + I_{\sigma'} \Theta^{k'}(x) \\ \text{where } : I_\sigma &= \begin{cases} -1 \\ +1 \end{cases}, \text{ and } I_\sigma \cdot I_{\sigma'} = -1 \end{aligned} \quad (5.24)$$

$$\begin{aligned} M_{ij} &= \int_{T_k^i} \int_{T_l^j} I_{\sigma_c^{k^i}}^k \Theta_{\sigma_c^{k^i}}^{k^i}(x)^{\alpha_i \beta_j} \Phi(x, y) I_{\sigma_c^{l^j}}^l \Theta_{\sigma_c^{l^j}}^{l^j}(y) dx dy \\ &+ \int_{T_k^i} \int_{T_l^j} I_{\sigma_c^{k^i}}^k \Theta_{\sigma_c^{k^i}}^{k^i}(x)^{\alpha_i \beta_j} \Phi(x, y) I_{\sigma_c^{l^j}}^l \Theta_{\sigma_c^{l^j}}^{l^j}(y) dx dy \\ &+ \int_{T_k^i} \int_{T_l^j} I_{\sigma_c^{k^i}}^k \Theta_{\sigma_c^{k^i}}^{k^i}(x)^{\alpha_i \beta_j} \Phi(x, y) I_{\sigma_c^{l^j}}^l \Theta_{\sigma_c^{l^j}}^{l^j}(y) dx dy \\ &+ \int_{T_k^i} \int_{T_l^j} I_{\sigma_c^{k^i}}^k \Theta_{\sigma_c^{k^i}}^{k^i}(x)^{\alpha_i \beta_j} \Phi(x, y) I_{\sigma_c^{l^j}}^l \Theta_{\sigma_c^{l^j}}^{l^j}(y) dx dy \end{aligned} \quad (5.25)$$

Where $\alpha_i, \beta_j \in \{e, m\}$, e, m represent the electric and magnetic current

We define i be a degree of freedom, if $i = q(k, k')$ and $I_{\sigma_c^k}^k(k, k') > 0$, we have

$$q^{-1}(i) = (k, k')$$

$$q^{-1} : \{1, 2, \dots, N_j\} \rightarrow \{1, 2, \dots, N\} \times \{1, 2, \dots, N\}$$

If $q^{-1}(i) = (k, k')$, we can define $q_1^{-1}(i) = k$ and $q_2^{-1}(i) = k'$

We define $\tilde{\sigma}^1(i) = \sigma_c^{q_1^{-1}(i)}(q_1^{-1}(i))$ and $\tilde{\sigma}^2(i) = \sigma_c^{q_2^{-1}(i)}(q_2^{-1}(i))$

So we have

$$\begin{aligned} M_{ij} &= \alpha_i \alpha_j Z_{\tilde{\sigma}^1(i) \tilde{\sigma}^1(j)}^{q_1^{-1}(i) q_1^{-1}(j)} - \alpha_i \alpha_j Z_{\tilde{\sigma}^1(i) \tilde{\sigma}^2(j)}^{q_1^{-1}(i) q_2^{-1}(j)} - \alpha_i \alpha_j Z_{\tilde{\sigma}^2(i) \tilde{\sigma}^1(j)}^{q_2^{-1}(i) q_1^{-1}(j)} + \alpha_i \alpha_j Z_{\tilde{\sigma}^2(i) \tilde{\sigma}^2(j)}^{q_2^{-1}(i) q_2^{-1}(j)} \\ M_{ii} &= \alpha_i \alpha_i Z_{\tilde{\sigma}^1(i) \tilde{\sigma}^1(i)}^{q_1^{-1}(i) q_1^{-1}(i)} - \alpha_i \alpha_i Z_{\tilde{\sigma}^1(i) \tilde{\sigma}^2(i)}^{q_1^{-1}(i) q_2^{-1}(i)} - \alpha_i \alpha_i Z_{\tilde{\sigma}^2(i) \tilde{\sigma}^1(i)}^{q_2^{-1}(i) q_1^{-1}(i)} + \alpha_i \alpha_i Z_{\tilde{\sigma}^2(i) \tilde{\sigma}^2(i)}^{q_2^{-1}(i) q_2^{-1}(i)} \\ \alpha_i \alpha_i Z_{\tilde{\sigma}^1(i) \tilde{\sigma}^2(i)}^{q_1^{-1}(i) q_2^{-1}(i)} &= \alpha_i \alpha_i Z_{\tilde{\sigma}^2(i) \tilde{\sigma}^1(i)}^{q_2^{-1}(i) q_1^{-1}(i)} \end{aligned} \quad (5.26)$$

(5.26)

We obtain:

$$M_{ii} = \alpha_i \alpha_i Z_{\tilde{\sigma}^1(i) \tilde{\sigma}^1(i)}^{q_1^{-1}(i) q_1^{-1}(i)} - 2 \alpha_i \alpha_i Z_{\tilde{\sigma}^1(i) \tilde{\sigma}^2(i)}^{q_1^{-1}(i) q_2^{-1}(i)} + \alpha_i \alpha_i Z_{\tilde{\sigma}^2(i) \tilde{\sigma}^2(i)}^{q_2^{-1}(i) q_2^{-1}(i)} \quad (5.27)$$

Let the initial structure have m number of degrees of freedom, for the new flux, the index is $m+1$. We can compute the new coupling between the old degrees of freedom with the new one, it can be written as:

$[M] = [M_{1m}, M_{2m}, \dots, M_{mm+1}]^T$, and we suppose $\tau = B_{m+1m+1}$ is the new coupling between flux $m+1$ and itself.

The linear system associated with the modified geometry $\Omega + \Delta\Omega$ can be written as

$$\begin{bmatrix} [Z] & [M] \\ [M]^T & \tau \end{bmatrix} \cdot \begin{bmatrix} [\Phi'] \\ \varphi \end{bmatrix} = \begin{bmatrix} [S] \\ \vartheta \end{bmatrix} \quad (5.28)$$

Where $[\Phi'] = [\Phi'_{1,L}, \Phi'_m]^T$ denotes the modified value of flux vector corresponding to initial geometry Ω when adding element T' , ϑ the excitation term on T' , and $[M]^T$ the transpose matrix of $[M]$, respectively.

Introducing vector $[D] = [\Phi'] - [\Phi]$, we have:

$$[Z][D] = -\varphi[M] \quad (5.29)$$

$$\varphi = \frac{\vartheta - [M]^T \cdot [\Phi]}{\tau - [M]^T \cdot [Z]^{-1} \cdot [M]} \quad (5.30)$$

The determination of the differential field $\delta \bar{E}^{comp}$ using the formula above can be easily computed as the matrix A has been already factorized for computing the vector $[\Phi]$ for the initial geometry.

By controlling different heights δh of the external triangle T', and using finite differential method, we can obtain the derivative of field related to the shape deformation:

$$\frac{\mathbf{W}_{comp}}{\partial E} = \frac{\delta E_{\delta h_2}^{comp} - \delta E_{\delta h_1}^{comp}}{\delta h_2 - \delta h_1} \quad (5.31)$$

CHAPTER 6: LEVEL SET METHOD

6.1 General Description

Antenna array optimization in general, and for reflectarray application in particular, must include not only the miniaturization of the different elements, but also the reduction of the number of elements, by finding at same time, the optimum shape/size and the of antenna elements for a certain goal or under certain constraints such as the radiation pattern, return loss, etc. leading to a global reduction size, if of course such a solution exists.

In the last chapter, we have discussed the calculation of the shape gradient on the contour. The shape gradient or sensitivity indicates the shape deformation during iterations, meanwhile, it shows the decrease of the cost functional. By means of the implicit shape representation using the Level Set method, we can deform the object contour along the normal direction with a certain velocity, with an opposite sign to the shape gradient vector.

A classic shape representation is the Lagrangian formulation, which considers a parameterized form of the velocity $V(x)$. Every point of the contour is defined. Since there are generally an infinite number of points on the front (except, in one spatial dimension), this means discretizing the boundary in a relatively dense and uniform manner to represent and trace the boundary accurately. The Lagrangian formulation is a very intuitive and direct method. It represents every point on the boundary versus time, and traces the motion of each one. However, the algorithm to determine the connectivity is difficult to design, especially when a topological change occurs, for example, when the boundary begins to be merged or splitted.

Level Set method is based on an implicit representation of the contours, which defines a one-higher dimension function, and the boundary is represented as the zero iso-contour of this function. This method was first introduced by Osher and Sethian in 1988. [29] One of the most important properties of level set method is that the shape of elements can merge and/or break. The Level Set Method is therefore an excellent method and quite suitable for not only optimizing the shape of a single patch antenna but also to optimize the number of elements, by finding the optimum size as well as the optimum number of elements.

6.2 Level Set Function

The original idea of level set methods is that the subsequent motion of the boundary is analyzed under a velocity field \vec{V} , which can depend on position, time, geometry of interface, and some optimization constrains (e.g., it can be related to the cost function). Mathematically, the key idea of level set is the

Hamilton-Jacobi approach to numerical solutions of a time-dependent equation for moving an implicit surface, [57] which is the level set function. Given an interface, which is bounded with an open region Ω , the level set function ϕ has the following properties:

$$\begin{cases} \phi(x,t) < 0 & \text{if } x \in \Omega \\ \phi(x,t) = 0 & \text{if } x \in \Gamma \\ \phi(x,t) > 0 & \text{if } x \notin \Omega \end{cases} \quad (6.1)$$

By the definition of the level set function, the interface is represented for all later times. The motion is analyzed by converting the levels with the velocity field \vec{V} , and the evolution of the level set function is defined by a Hamilton-Jacobi equation of the form:

$$\frac{\partial \phi}{\partial t} + \vec{V} \cdot \nabla \phi = 0 \quad (6.2)$$

With initial value given by:

$$\phi(\cdot, 0) = \phi_0 \quad (6.3)$$

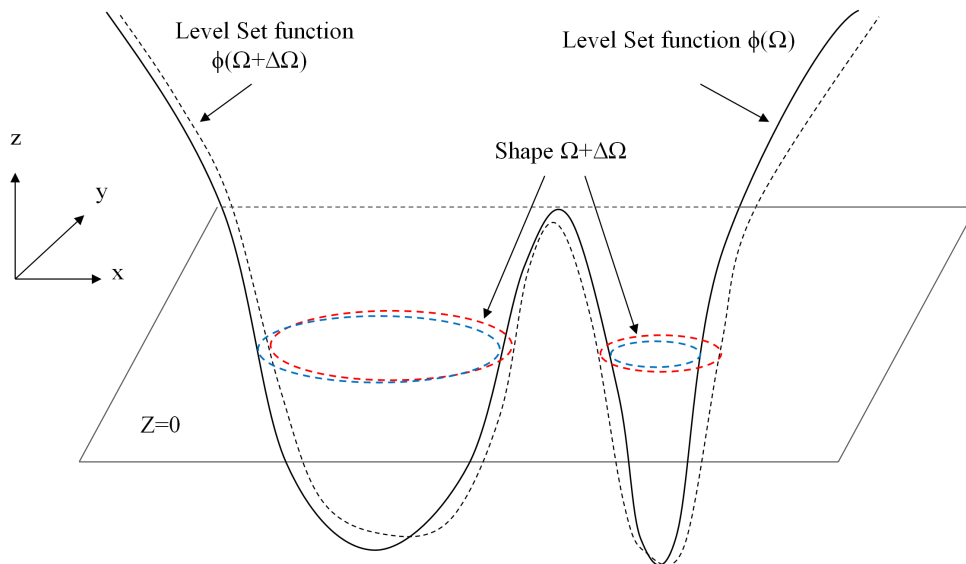


Figure: 6.1: Level Set function

Figure 6.1 illustrates an example of the shape deformation using the Level Set method. In the XOY plane, the former shape Ω (blue line) evolves to the shape $\Omega + \Delta\Omega$ (red line). It is difficult to describe and evolve the shape Ω to $\Omega + \Delta\Omega$ only by defining the contour of the shape and transforming it numerically. Using Level Set method, one can define a level set function

which works on a higher dimension space than the geometric shape, by computing and analysing the update of the level set functional, which works in an implicit way, the shape can evolve easily rather than evolving the boundary of the object in the initial dimension directly.

6.3 Normal Velocity

When we consider a boundary, in order to characterize the evolution of the level set function, a speed function V can be defined such as:

$$V(x) = \frac{\partial x}{\partial t} \quad (x \in \Gamma) \quad (6.4)$$

This velocity function can depend on many factors, and be derived from the independent external physical field, global properties of the front, and the local geometric information such as curvature and normal directional velocity. Generally, when we consider the inverse electromagnetic problems, we only consider the local geometric information. [29]

In this case, the normal unit outward vector can be written as:

$$\vec{n} = \frac{\nabla \phi}{|\nabla \phi|} \quad (6.5)$$

And, the curvature is:

$$K = \nabla \cdot \left(\frac{\nabla \phi}{|\nabla \phi|} \right) \quad (6.6)$$

Suppose the normal component of the velocity in the normal direction \vec{N} is V_N , of the velocity \vec{V} . We can obtain:

$$\left(\vec{V}_N \cdot \nabla \right) \phi = \vec{V}_N \cdot \nabla \phi = \left(V_N \cdot \vec{n} \right) \cdot \nabla \phi = V_N \frac{\nabla \phi}{|\nabla \phi|} \cdot \nabla \phi = V_N \cdot |\nabla \phi| \quad (6.7)$$

By considering this normal deformation velocity, we can use for the level set function, the Hamilton-Jacobi equation:

$$\begin{aligned}\frac{\partial \phi}{\partial t} + V_N \cdot |\nabla \phi| &= 0 \\ \frac{\partial \phi}{\partial t} &= -V_N \cdot |\nabla \phi|\end{aligned}\tag{6.8}$$

From this Hamilton-Jacobi equation, we can see that the left part of the partial equation is the derivative of level set function versus time, and the right part $\nabla \phi$ denotes the spatial derivative of ϕ at the grid point. Once we obtain the spatial derivative of ϕ and the normal velocity, then we can apply finite difference approximation to evolve the level set function. Suppose the current evolution is m , and the next one is $m+1$, we have different level set function for time t^{m+1} and t^m , which are ϕ^{m+1} and ϕ^m respectively, and $\Delta t = t^{m+1} - t^m$ represents the time step. [29] We can obtain the level set function at t^{m+1} using the first order forward Euler method:

$$\frac{\phi^{m+1} - \phi^m}{\Delta t} = -V_N \cdot |\nabla \phi|\tag{6.9}$$

We use a uniform grid for all the set of data points where the implicit function ϕ is defined, and initially we use a signed distance function to define different level set function, it can be written as:

$$\phi(x, 0) = \begin{cases} -\min\left(\left| \overset{\mathbf{v}}{x} - \overset{\mathbf{v}}{x_\Gamma} \right| \right) & \text{if } x \in \Omega \\ 0 & \text{if } x \in \Gamma \\ \min\left(\left| \overset{\mathbf{v}}{x} - \overset{\mathbf{v}}{x_\Gamma} \right| \right) & \text{if } x \notin \Omega \end{cases}\tag{6.10}$$

With the signed distance function, which is an implicit function, we can find the contour by computing the different distance values of all the pixels, and distinguish the region in and out of the object from negative and positive signs. In addition, $\min\left(\left| \overset{\mathbf{v}}{x} - \overset{\mathbf{v}}{x_\Gamma} \right| \right)$ is an Euclidean distance function with gradient

$\nabla \phi = 1$, is monotonic across the surface and can be differentiated there with significantly higher confidence. [29]

We have:

$$\mathbf{V}_N \cdot \nabla \phi = V_N \cdot |\nabla \phi| = u\phi_x + v\phi_y + w\phi_z \quad (6.11)$$

For the one-dimensional case, and considering a specific grid point x_i , we can write:

$$\frac{\phi_i^{m+1} - \phi_i^m}{\Delta t} = -u_i^m (\phi_x)_i^m \quad (6.12)$$

If $u_i > 0$, the values of ϕ are moving from the left to right, and the method of characteristics tells us to look to the left of x_i to determine what value of ϕ will land on the point x_i at the end of a time step. Similarly, if $u_i < 0$, the values of ϕ are moving from the right to left, and the method of characteristics implies that we should look to the left of x_i to determine what value of ϕ will land on the point x_i at the end of a time step. [29]

When $u_i > 0$, we should use a first-order accurate backward difference to approximate ϕ_x

$$D^- \phi_x = \frac{\partial \phi}{\partial x} \approx \frac{\phi_i - \phi_{i+1}}{\Delta x} \quad (6.13)$$

When $u_i < 0$, we should use a first-order accurate forward difference to approximate ϕ_x

$$D^+ \phi_x = \frac{\partial \phi}{\partial x} \approx \frac{\phi_{i+1} - \phi_i}{\Delta x} \quad (6.14)$$

This method of choosing an approximation to the spatial derivatives based on the sign of u is known as upwind differencing, the errors are $O(\Delta x)$ [29].

6.4 Narrow Band Method

When we apply an implicit representation to describe the motion of objects, actually we define not only the objects with a distance function, but also all the spatial maps. However, in our case, when we evolve the shape of antenna elements, in fact, only the conditions on the contour of antenna elements are changed. In other words, when we use the Level Set method to optimize antenna elements, we need only to consider the motion of the object contour,

and it is not efficient to evolve the entire surface. Thereafter, we need to find a method to evolve only the level set function, which are close to the boundary [50].

Therefore, we need to apply the narrow band method in the processing of evolution of the Level Set method. The idea of the narrow band method is to solve the level set equation in a narrow band with γ pixels wide around the interface. All the values outside this band are set to a value of $+\gamma$ or $-\gamma$, and not to be evolved until they are close enough to the narrow band [50]. Then the narrow band can be represented by:

$$\phi(x) = \begin{cases} -\gamma & \text{if } d(x) < -\gamma \\ d(x) & \text{if } |d(x)| \leq \gamma \\ \gamma & \text{if } d(x) > \gamma \end{cases} \quad (6.15)$$

6.5 Re-Initialization

As the interface evolves, the level set function ϕ will generally drift away from its initialized value as signed distance, the evolution of $\phi_t + V \cdot \nabla \phi = 0$ often distorts the level set function after several iterations. It happens in the sense that the slope is too flat or too steep around the interface. A small perturbation of the level function may lead a big change of interface location, and the level function may lose enough regularity near the interface. Thus it is necessary to apply a kind of techniques periodically in order to keep ϕ approximately equal to the signed distance. We can apply the distance function to the interface to replace the level set function in order to keep the regularity near the interface [50].

The re-initialization is done by solving the Eikonal equation :

$$\frac{\partial \phi}{\partial t} = \text{Sign}(\phi)(1 - |\nabla \phi|) \quad (6.16)$$

where *Sign* is the sign function defined as

$$\text{Sign}(\phi) = \begin{cases} 1 & \text{if } \phi > 0 \\ 0 & \text{if } \phi = 0 \\ -1 & \text{if } \phi < 0 \end{cases} \quad (6.17)$$

By using this Eikonal equation, we can eliminate many numerical issues and preserve the interface.

In order to apply the re-initialization step in a certain range to the level set function, we need to define a band, which can be written as:

$$\phi(x+x') = \begin{cases} -\gamma & \text{if } d(x+x') < \gamma \\ d(x+x') & \text{if } |d(x+x')| \leq \gamma \\ \gamma & \text{if } d(x+x') > \gamma \end{cases} \quad (6.18)$$

where $|x'| < \Delta x$, Δx is the size of the level set pixel.

6.6 An Upper Limit to the Size of Δt

The Courant-Friedrichs-Lewy (CFL) stability condition indicates that the numerical wave speed of $\Delta x / \Delta t$ must be at least as fast as the physical wave speed $|u|$, i.e., $\Delta x / \Delta t > |u|$ [29]. This requires to have an upper bound on Δt .

When the shape deforms in the normal direction, we only choose the largest value of $|u|$ on the interface, With this value, we can guarantee that all the discretized pixels satisfy the CFL time step restriction:

$$\Delta t \left(\frac{\max\{|u|\}}{\Delta x} \right) = \alpha \quad (6.19)$$

Where: $0 < \alpha < 1$.

A multidimensional CFL condition can be written as:

$$\Delta t \max \left\{ \frac{|u|}{\Delta x} + \frac{|v|}{\Delta y} + \frac{|w|}{\Delta z} \right\} = \alpha \quad (6.20)$$

Where Δx , Δy , Δz denotes the discretized spatial step in x, y, z direction [29].

The time step Δt is an important configuration for reaching a stable solution, and also related to the shape deform velocity.

Unfortunately, the simple central differencing is unstable with forward Euler time discretization and the usual CFL conditions with $\Delta t \sim \Delta x$. Stability can be achieved by using a much more restrictive CFL condition with Δt is equivalent to higher order of Δx .

In addition, the upper limit of the time Δt can be used to control the motion of level set function. For the aim of satisfying CFL condition, α should be less than zero, while in some situations of optimization procedure, for example, when the optimal object is close to the goal, we need to slow down the motion of the boundary. There are some ways to manage this boundary motion, for instance, we can use a smaller grid to discretize the level set map, decrease the evolving times number to limit the iteration steps at every time iteration, and also decrease the coefficient α , as we discussed above, which means if we use smaller value of α , we can control the change of level set function to use a small step to approach the goal object slowly.

6.7 Apply Shape Gradient to Level Set Method

The differential of the cost functional is given by:

$$\delta F = \frac{-2 \sum_{s=1}^S \sum_{q=1}^Q \operatorname{Re} \left[\left(\vec{E}_{s,q}^{meas} - \vec{E}_{s,q}^{comp}(\Omega) \right) \cdot \delta \vec{E}_{s,q}^{comp}(\Omega) \right]}{\sum_{s=1}^S \sum_{q=1}^Q \left| \vec{E}_{s,q}^{meas} \right|^2} \quad (6.21)$$

Thus we can write the shape gradient as:

$$\frac{\partial F}{\partial \Omega} = \frac{-2 \sum_{s=1}^S \sum_{q=1}^Q \operatorname{Re} \left[\left(\vec{E}_{s,q}^{meas} - \vec{E}_{s,q}^{comp}(\Omega) \right) \cdot \frac{\partial \vec{E}_{s,q}^{comp}(\Omega)}{\partial \Omega} \right]}{\sum_{s=1}^S \sum_{q=1}^Q \left| \vec{E}_{s,q}^{meas} \right|^2} \quad (6.22)$$

$$\text{where } \frac{\partial \vec{E}_{s,q}^{comp}(\Omega)}{\partial \Omega} = \frac{\delta \vec{E}_{s,q}^{comp}(\Omega)}{\delta \Omega}$$

By considering the CFL condition, we take into account the coefficient α , which we discussed in the last section. Then the velocity can be written as:

$$V_N = -\alpha \frac{\partial F}{\partial \Omega} = 2\alpha \frac{\sum_{s=1}^S \sum_{q=1}^Q \operatorname{Re} \left[\left(\vec{E}_{s,q}^{meas} - \vec{E}_{s,q}^{comp}(\Omega) \right) \cdot \frac{\partial \vec{E}_{s,q}^{comp}(\Omega)}{\partial \Omega} \right]}{\sum_{s=1}^S \sum_{q=1}^Q \left| \vec{E}_{s,q}^{meas} \right|^2} \quad (6.23)$$

The sign of the normal velocity is different from the shape gradient. It means that if we evolve the antenna boundary along its normal direction, and take the negative value of shape gradient, the cost functional will be decreased. When the cost functional reaches a small enough value, we hope to obtain an optimized antenna or antenna array shape.

6.8 Procedure of Level Set Optimization

Once we obtained the shape gradient for antenna geometry, we can apply it as the normal velocity to the Hamilton-Jacobi equation. At n th iteration, we define the surface ϕ_n as the zero-level iso-surface of a function.

Thus at n th iteration, the optimization procedure contains:

1. Computation of the shape gradient;
2. Extension of the shape gradient to the deformation velocity V_N to every pixel of the narrow band;
3. Evolve the level set function, and obtain a new value of level set;
4. Determine the new narrow band;
5. Chain the pixels of level zero, obtain a new shape ϕ_{n+1} , and apply the forward scattering algorithm;
6. Compute the cost functional for the new shape.

CHAPTER 7: NUMERICAL VALIDATIONS

In the last chapters, we have described all the optimization procure, and explained in details the numerical method used to solve forward and inverse problem. In this chapter, we present some numerical validations to investigate the performances of different shape gradient methods in different situations. The main work contains:

1. Study of the scattered fields of a cylinder antenna
2. Validation of the adjoint formula for a cylinder antenna
3. Validation of the adjoint formula for a 2D patch antenna
4. Validation of the adjoint formula for a 3D patch antenna
5. Shape gradient computation by different shape deformations

7.1 Study of the Scattered Field of a Cylinder Antenna

We are using three different antenna shapes (shown in Figure 7.1 as object A, B and C) to study the differences between their scattered fields. Object A is a cylinder shape antenna with top, B a circular shape antenna, and C a cylinder shape antenna without top. In fact, from the structure of the antenna shape, Object A is composed with B and C. There are 6 dipoles surrounding the object and illuminating the object (shown in Table 7.1), and working at 3 GHz. The scattered fields are measured on a plane parallel to the xOy plane ($z=0.05$ m). We sum up the scattered field radiated by objects B and C, and compare with the scattered field radiated by object A for different cases given by different sizes of antennas. The radius of cylinder and circle R is equal to 0.6λ , 0.7λ , 0.8λ , 0.9λ , 1.0λ , respectively. The mesh size is $\lambda/10$.

Dipole N#	Dipole Moment	x [m]	y [m]	z [m]
1	(0,1,1)	2	0	0.05
2	(-0.866, 0.5,1)	1	1.732	0.05
3	(-0.866,-0.5,1)	-1	1.732	0.05
4	(0,-1,1)	-2	0	0.05
5	(0.866,-0.5,1)	-1	-1.732	0.05
6	(0.866, 0.5,1)	1	-1.732	0.05

Table 7.1: Position and moment of dipoles

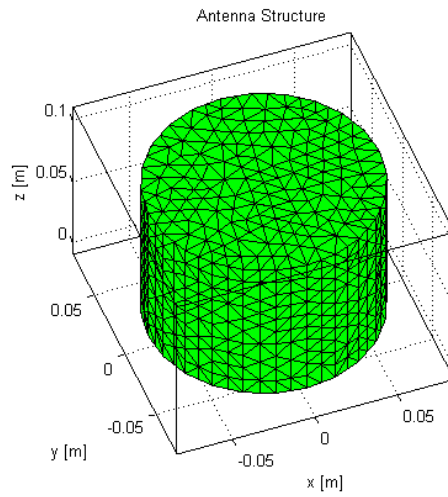


Figure 7.1a: Object A

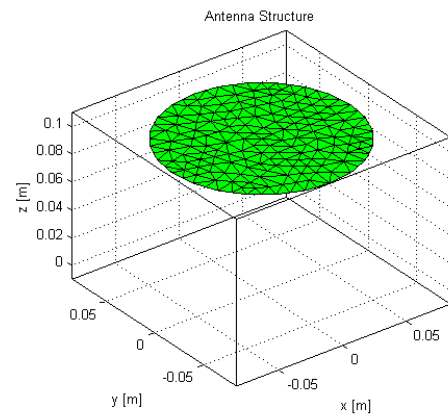


Figure 7.1b: Object B

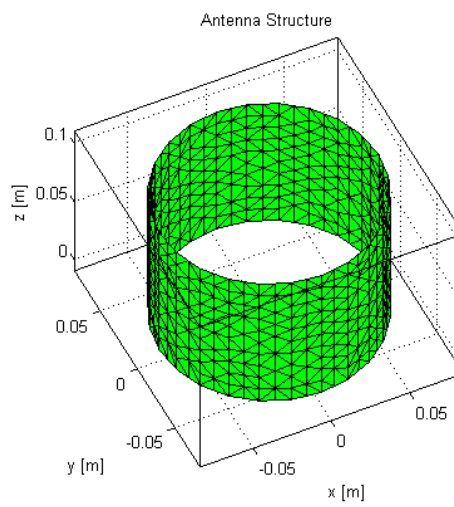


Figure 7.1c: Object C

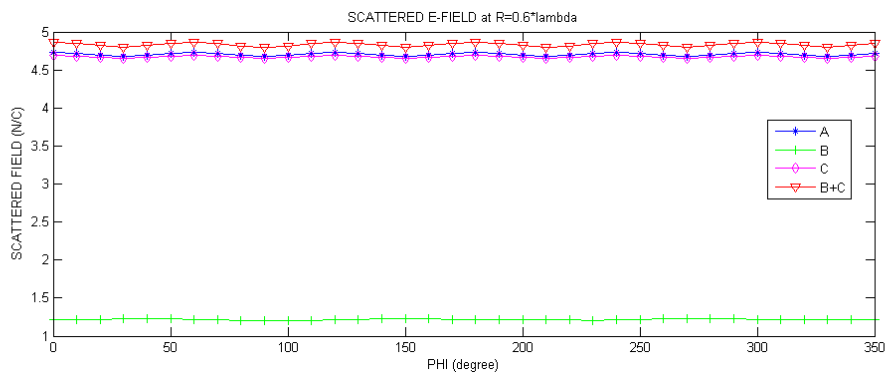


Figure 7.2a: Scattered field $R=0.6\lambda$

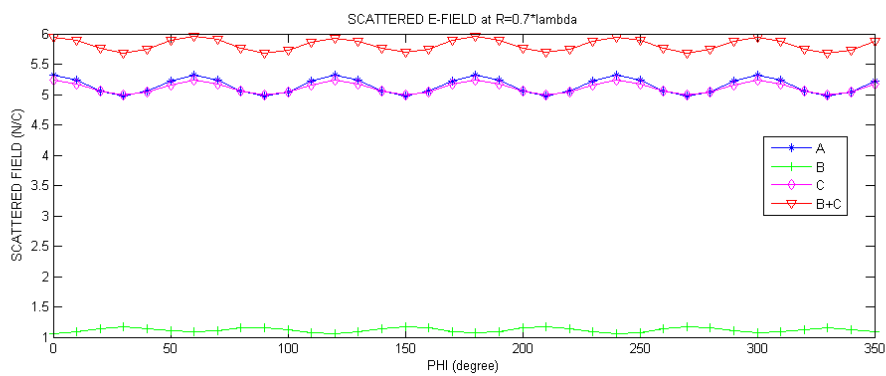


Figure 7.2b: Scattered field $R=0.7\lambda$

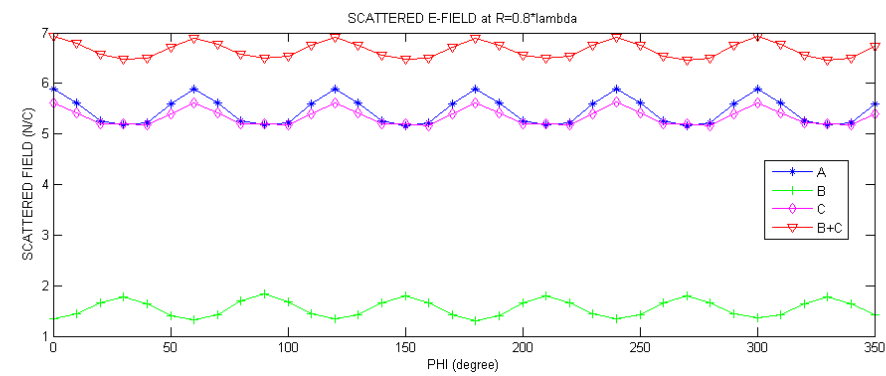


Figure 7.2c: Scattered field $R=0.8\lambda$

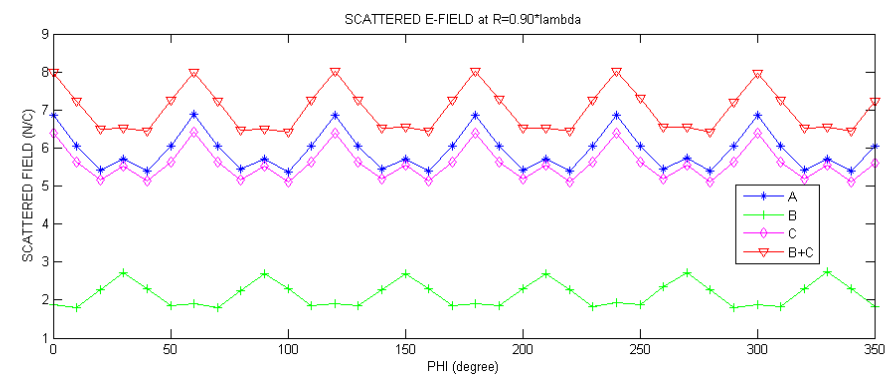


Figure 7.2d: Scattered field $R=0.9\lambda$

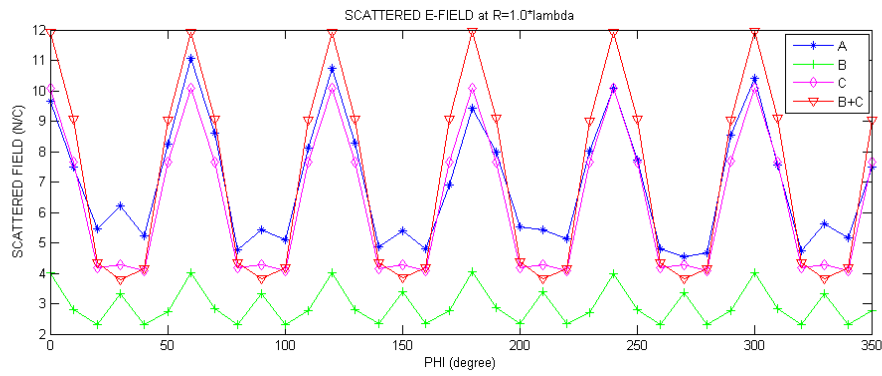


Figure 7.2e: Scattered field $R=1.0\lambda$

The results illustrated in Figure 7.2 show that when we compute the scattered field of a cylinder antenna, the field scattered by the side of cylinder more is important, and by comparing the field of object A and B, we find that there are no large differences. By summing up the scattered field radiated by object B and C, we find a higher value than the field radiated by objects B and C.

7.2 Validation of the Adjoint Formula for a Cylinder Antenna

In this study, we validate the shape gradient of a cylinder antenna by using adjoint and discrete method. Figure 8.3 shows the antenna structure of the cylinder antenna, the mesh of the antenna is $\lambda/20$. We use six incident dipoles illuminating at different positions (shown in Table 7.2), working at 3 GHz, and measured at the same positions as the incident dipoles.

Dipole N#	Dipole Moment	x[m]	y[m]	z[m]
1	(0,0,1)	2	0	0.1
2	(0,0,1)	1	1.732	0.1
3	(0,0,1)	-1	1.732	0.1
4	(0,0,1)	-2	0	0.1
5	(0,0,1)	-1	-1.732	0.1
6	(0,0,1)	1	-1.732	0.1

Table 7.2: Position and moment of dipoles

We compare the shape gradient of different antenna sizes by changing the radius of the cylinder. (Shown in Table 7.3)

Working Frequency	Dimension	Mesh
3.0GHz	R= ($0.665\lambda \sim 0.720\lambda$) Step: 0.005λ	$\lambda/20$

Table 7.3: Information of the cylinder antenna

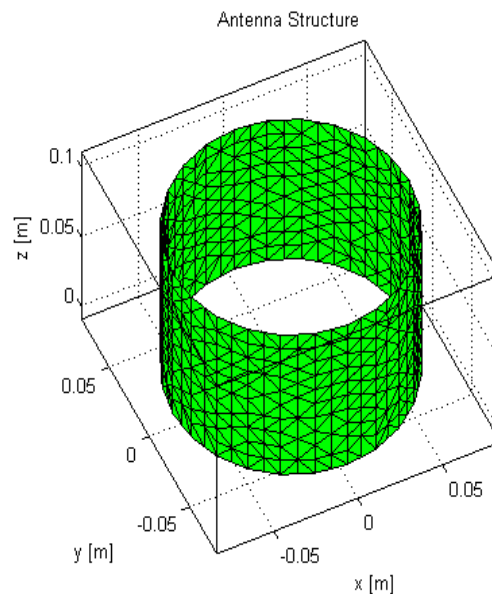


Figure 7.3: Cylinder Antenna

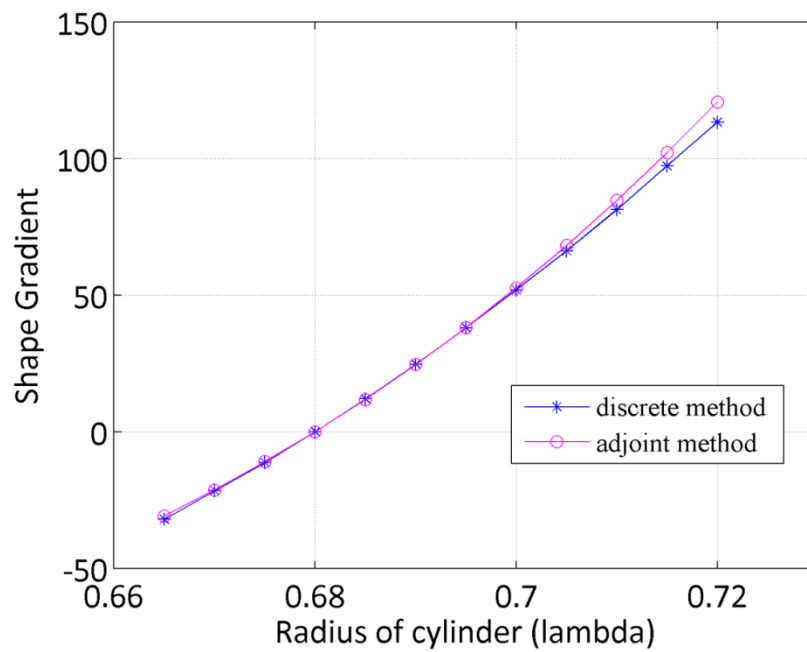


Figure 7.4: Antenna shape gradient

The results shown in Figure 7.4 indicate that when we enlarge the radius of the cylinder, we can get almost the same results of the shape gradient by using discrete and adjoint method.

7.3 Validation of the Adjoint Formula for a 2D Patch Antenna

In this experiment, we compute the shape gradients of a 2D patch rectangular antenna located in the xOy plane moving along z direction by using discrete, analytical, and adjoint methods, respectively. The size of the rectangular antenna is about $0.6\text{ m} \times 0.3\text{ m}$ shown in Figure 7.5. By changing the height of incident dipole (shown in Figure 7.6), we can change relatively the location of the goal along z direction.

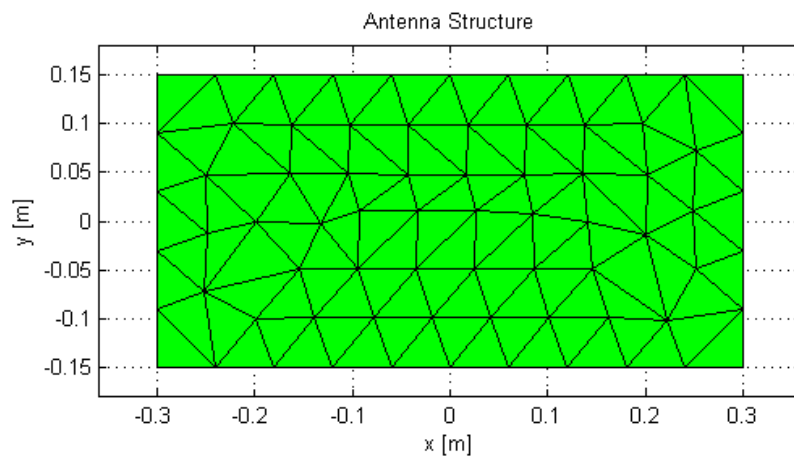


Figure 7.5: Antenna structure

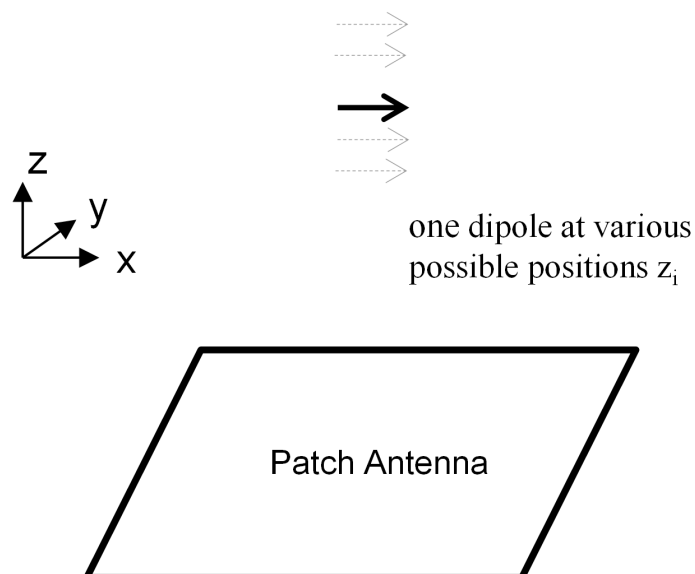


Figure 7.6: One incident dipole moving along z direction

We use one incident dipole working at 3GHz to illumine the patch antenna (shown in Table 7.4, and z_0 is the initial location of the incident dipole), and measured at the same position as the incident dipoles. The initial position of the incident dipole is at 6 m height.

Dipole N#	Dipole Moment	x[m]	y[m]	z[m]
1	(1,0,0)	0	0	$z_i = z_0 + \Delta z * i$ $\Delta z = 0.001\text{m}$ $z_0 = 6\text{ m}$ $i = (0, 1, 2, 3 \dots 20)$

Table 7.4: Incident dipoles

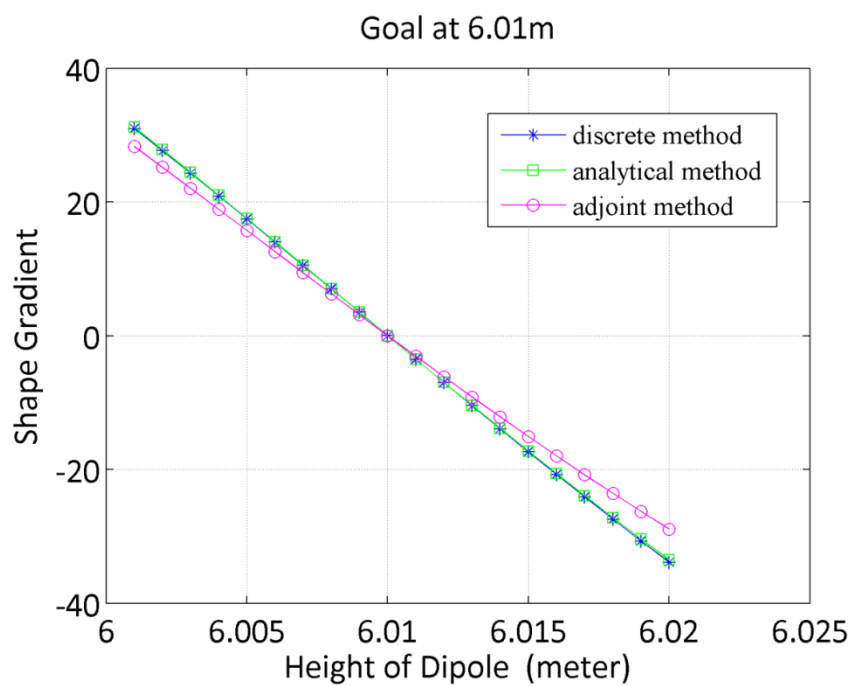


Figure 7.7a: Antenna shape gradient

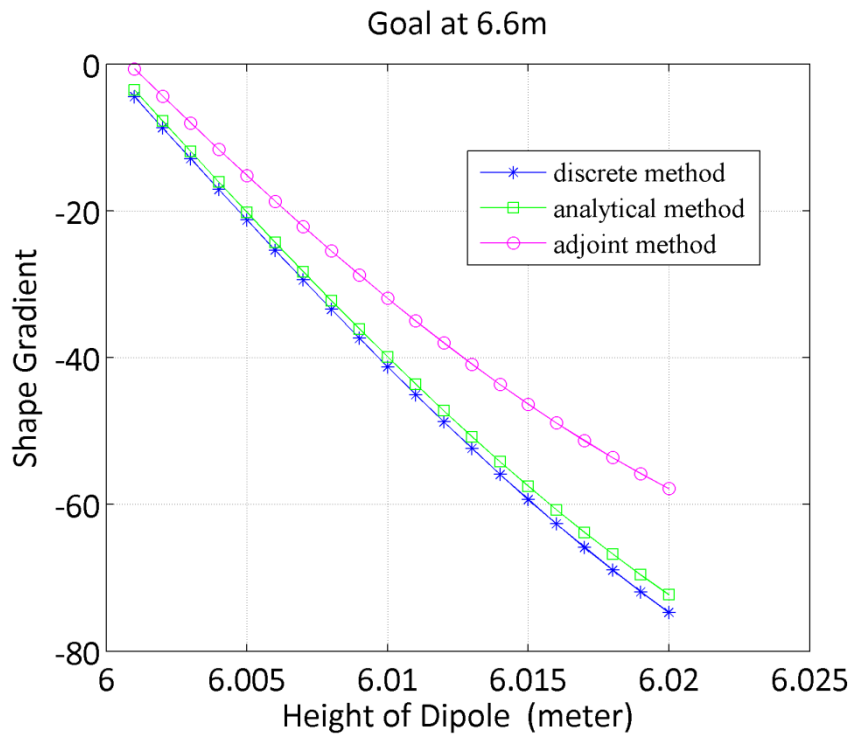


Figure 7.7b: Antenna shape gradient

From the results shown in Figure 7.7, we can see that for both the goal at 6.01m and 6.6 m, the results of analytical, adjoint, and discrete method are relatively close. However, the analytical method can give a more accurate result by comparing the results of discrete method as a criterion. In the Figure 7.7b, we can see as we increase the height of incident dipole, the adjoint method gives more different values from the discrete and analytical method.

7.4 Validation of the Adjoint Formula for a 3D Patch Antenna

In this experiment, we compute the shape gradient of a 3D patch rectangular antenna enlarging along the normal direction on the surface by using discrete, and adjoint method, respectively.

7.4.1 Thin 3D Patch Antenna Enlarged Along All Normal Directions

We first compute the shape gradient for a thin patch 3D antenna. The size of the rectangular antenna is around 10 cm*5 cm*0.2 cm as shown in Figure 7.8, and the mesh size is $\lambda/20$. We use one incident dipole working at 3 GHz to illuminate and one measurement point to measure in the same location as shown in Table 7.5. By changing the moments of the incident dipole as illustrated in Figure 7.10, we compute the shape gradient of moving the 3D antenna shape along its normal direction (shown in Figure 7.9).

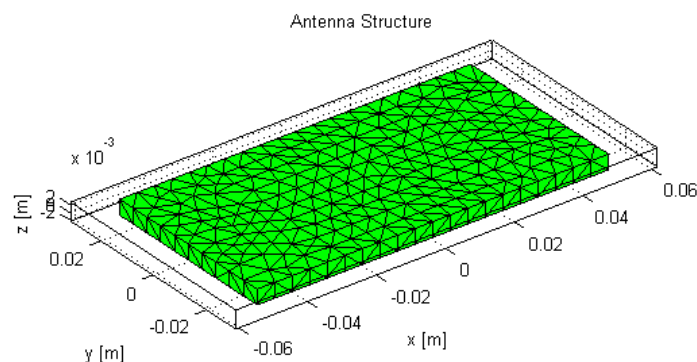


Figure 7.8: Antenna structure

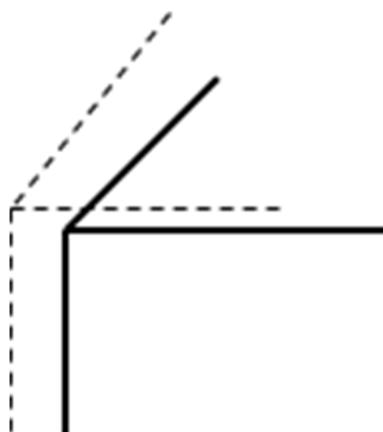


Figure 7.9: Antenna shape deformation

Dipole & Measurement point N#	Dipole Moment (x,y,z)	x[m]	y[m]	z[m]
1	(1,1,0) (1,1,0.5) (1,1,1) (1,1,2) (1,1,3) (1,1,5) (0,0,1)	0.25*lambda	0.125*lambda	5.0*lambda

Table 7.5: Incident dipole and measurement point

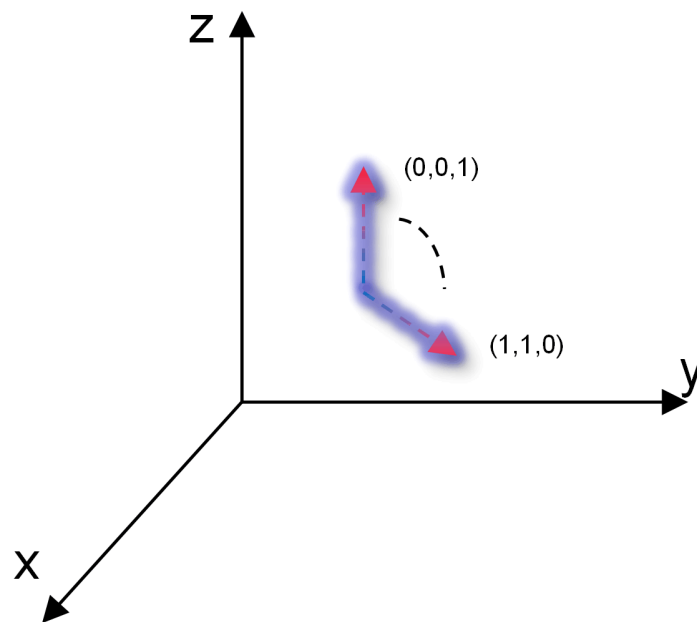


Figure 7.10: Moment of incident dipole

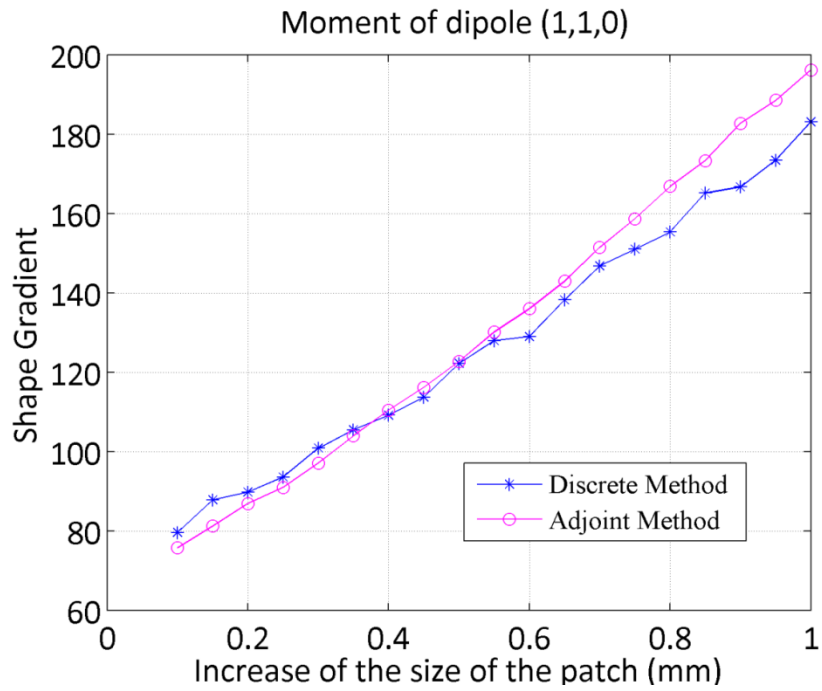


Figure 7.11a: Shape gradient

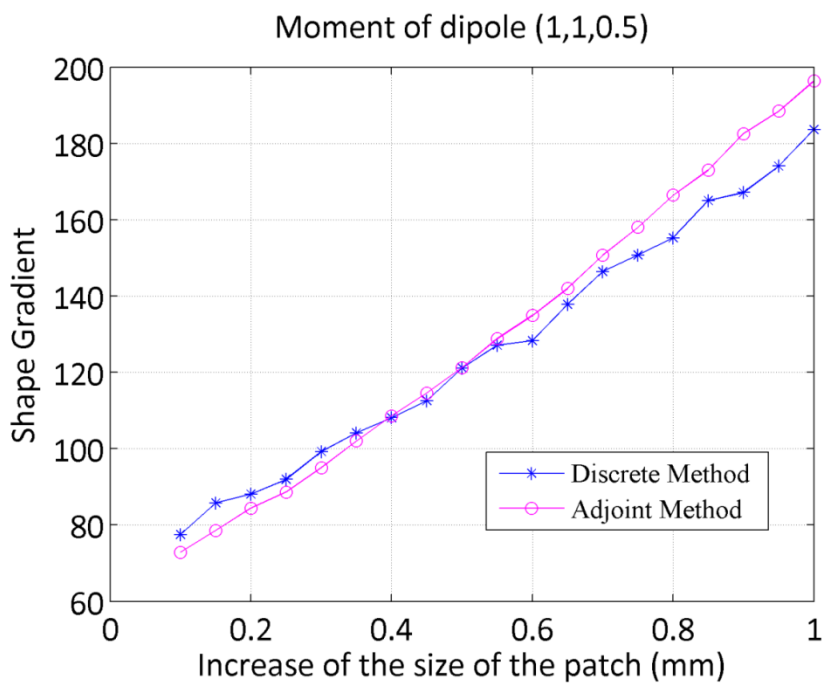


Figure 7.11b: Shape gradient

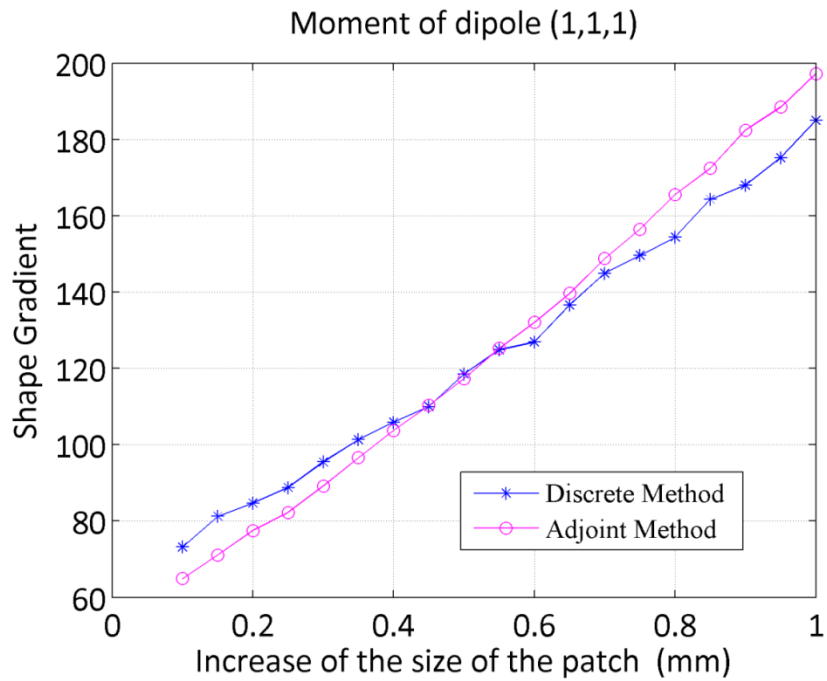


Figure 7.11c: Shape gradient

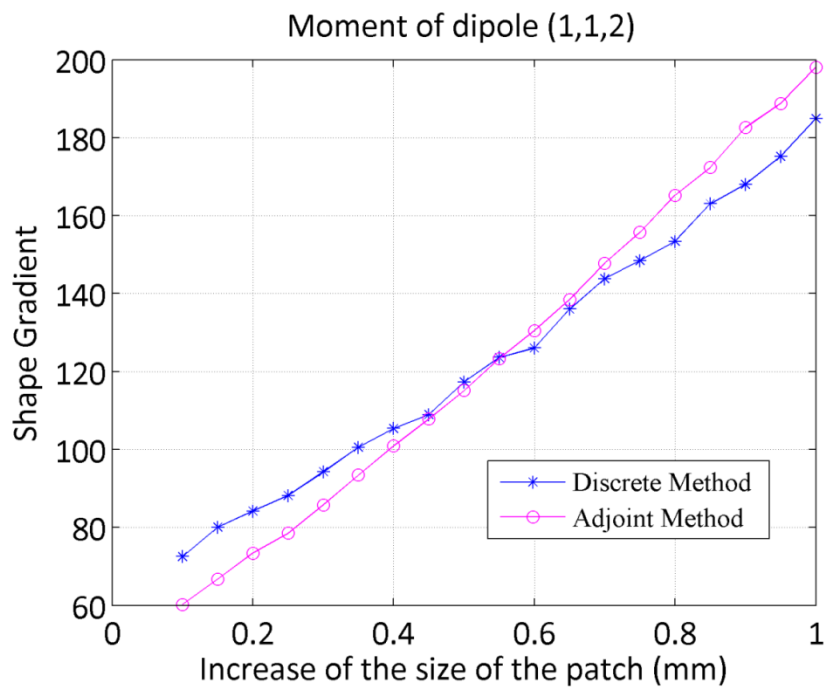


Figure 7.11d: Shape gradient

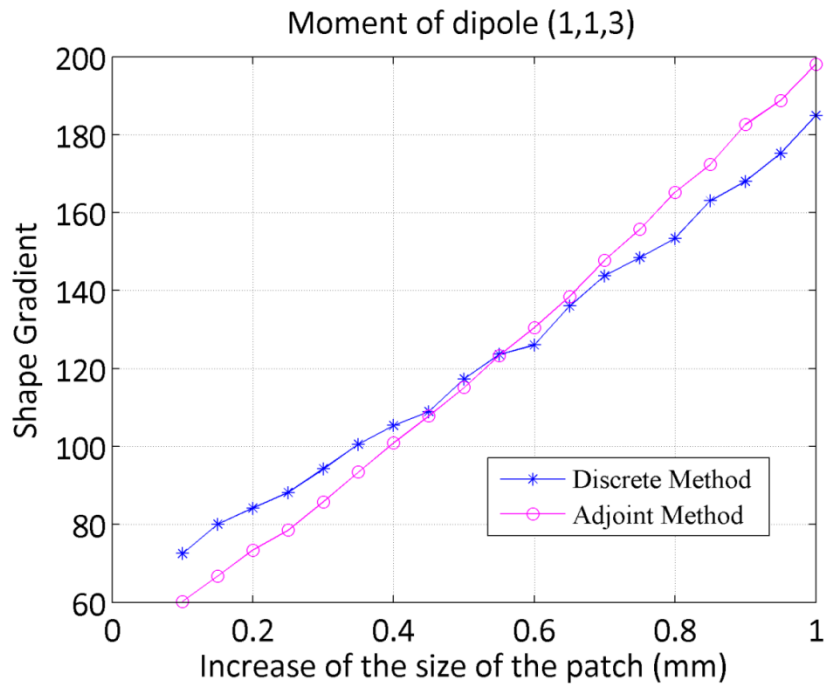


Figure 7.11e: Shape gradient

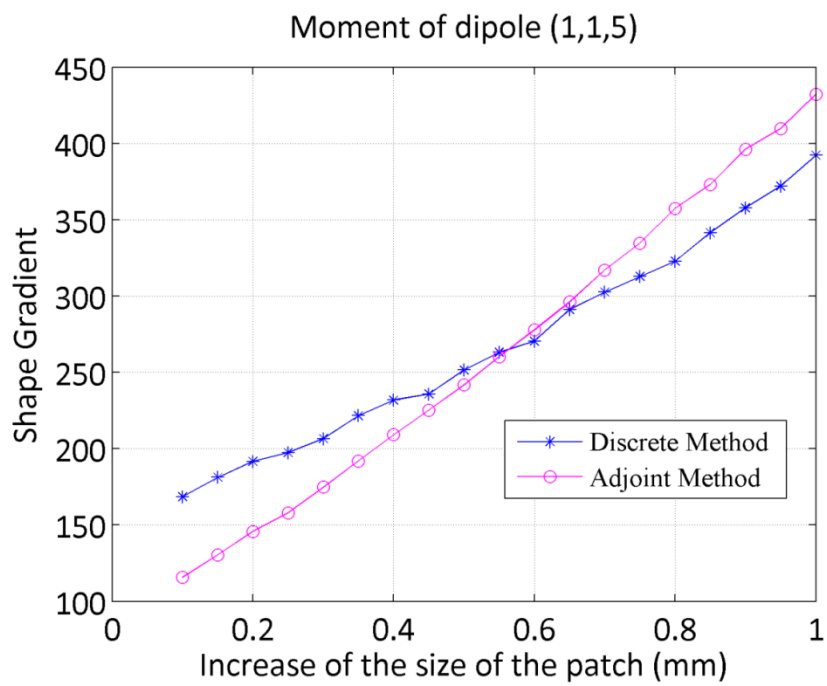


Figure 7.11f: Shape gradient

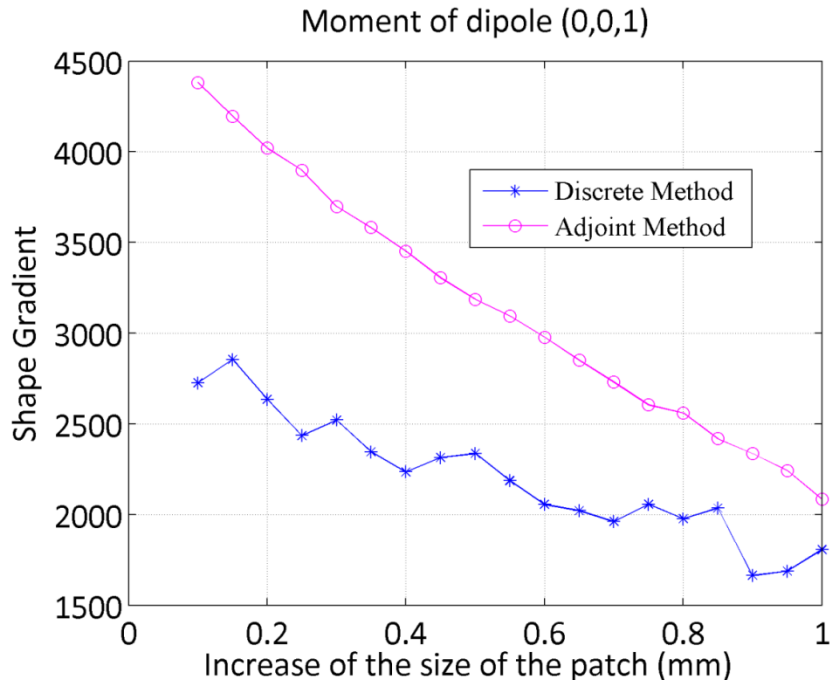


Figure 7.11g: Shape gradient

Figure 7.11 shows the shape gradients of enlarging the 3D antenna along the normal direction computed by using both adjoint and discrete method. From the results, we can see that there is a relationship between the moment of the incident wave and shape gradients. When the moment of incident dipole is turning close to +z direction, the shape gradient is becoming more and inaccurate when comparing the results given by the discrete method as the criterion, since the currents are more important on the thin edges of the antenna structure. When the moment of incident dipole is (0,0,1), the results of shape sensitivity given by discrete method and adjoint method are very different, as we consider the discrete method as the more accurate result.

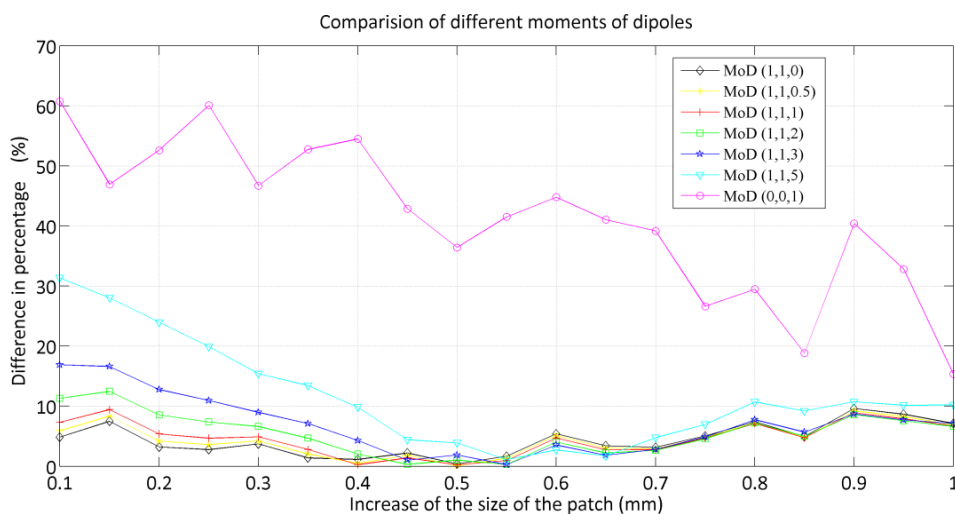


Figure 7.12 Comparison of adjoint and discrete methods

Figure 7.12 shows clear results of the differences on the shape gradients between the moments of dipole (MoD). When the MoD is $(1,1,0)$, the currents on the edge side of the antenna are very weak, while the currents on the top and bottom sides contribute more to the scattered fields and surface area of the antenna, so that we can obtain more accurate shape gradient when we are enlarging the antenna size along the normal direction of the surface, the highest value of the difference between the adjoint and discrete methods is about 8%. When the MoD is $(1,1,3)$, we have more currents distributed on the thin edge sides, in this case, the highest difference is about 17%. When the MoD is $(1,1,5)$, the currents on the top and bottom sides are becoming weaker, while the shape deformation of the antenna on the top and bottom sides does not change, we can see that the highest difference is about 32%. Finally, when we move the incident dipole vertical to the xOz plane, where the MoD is $(0,0,1)$, there is almost no currents distributed on the top and bottom of the antenna, in this case, we can see that the difference between the adjoint and discrete method is really high, about 61%.

7.4.2 Thin 3D Patch Antenna Enlarged Along +x Direction

Now, we change antenna moment to $(1,1,1)$, and the location of the incident dipole is shown in Table 7.6. In this situation, we compute the forward current density and adjoint current density. In addition, for the shape deformation of the antenna structure, we only enlarge the antenna along x direction. While by considering the dipole moment, the currents on the edge in green color shown in Figure 7.13 are considerable.

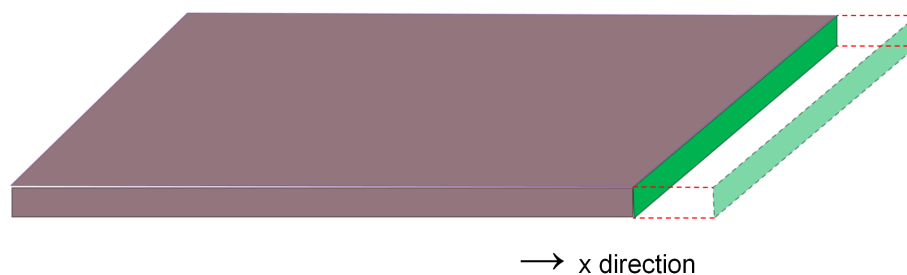


Figure 7.13: Antenna Shape deformations along x direction

Dipole & Measurement point N#	Dipole Moment	x [m]	y [m]	z [m]
1	$(1,1,1)$	$0.25*\lambda$	$0.125*\lambda$	$5.0*\lambda$

Table 7.6: Incident dipole and measurement point

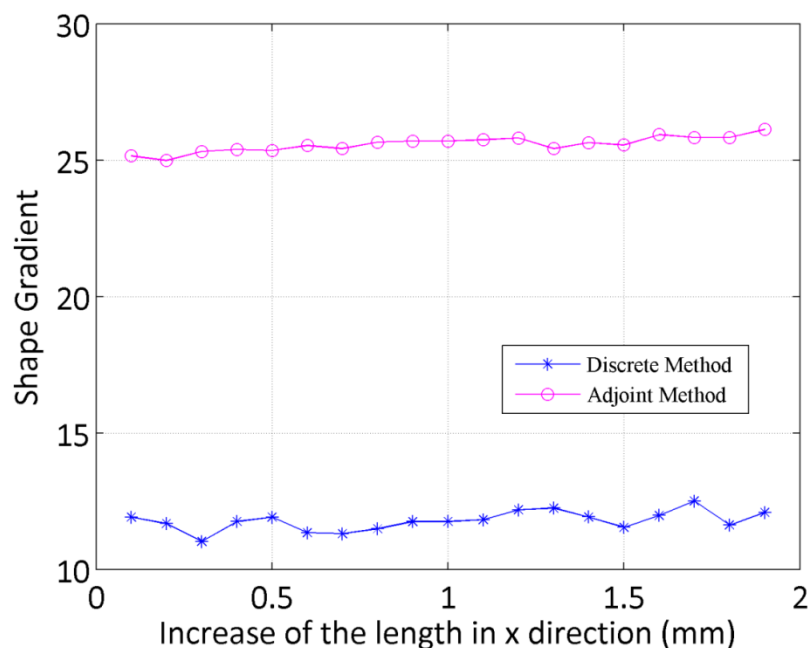


Figure 7.14: Shape gradient

The results in Figure 7.14 show that there are large differences of the shape gradient computed by adjoint and discrete method, the value of the shape gradients computed by the adjoint method are almost two times higher than the discrete method. However, the accurate current density on a very thin edge is hard to compute accurately due to thin edge effect and curse mesh.

7.4.3 Thick 3D Antenna Enlarged Along +x Direction

In order to avoid the effect of thin edge and curse mesh, we increase the height of antenna from $\lambda/50$ to $\lambda/4$, so that the current density on the edge can be computed more accurately, and then we do the same experiments as before. The new antenna structure is shown Figure 7.15, and the shape deformation in Figure 7.16

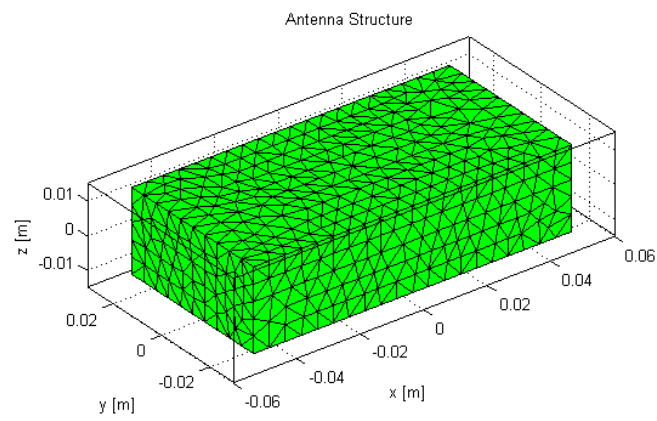


Figure 7.15: Antenna structure

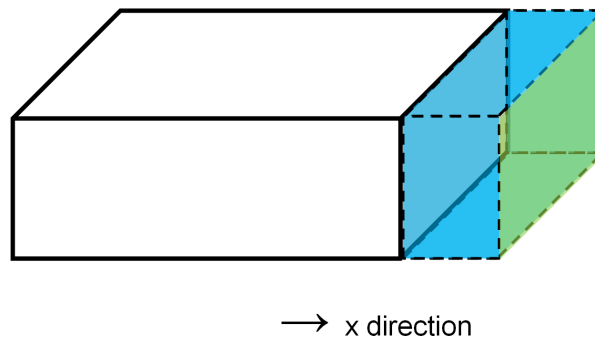


Figure 7.16: Antenna shape deformation

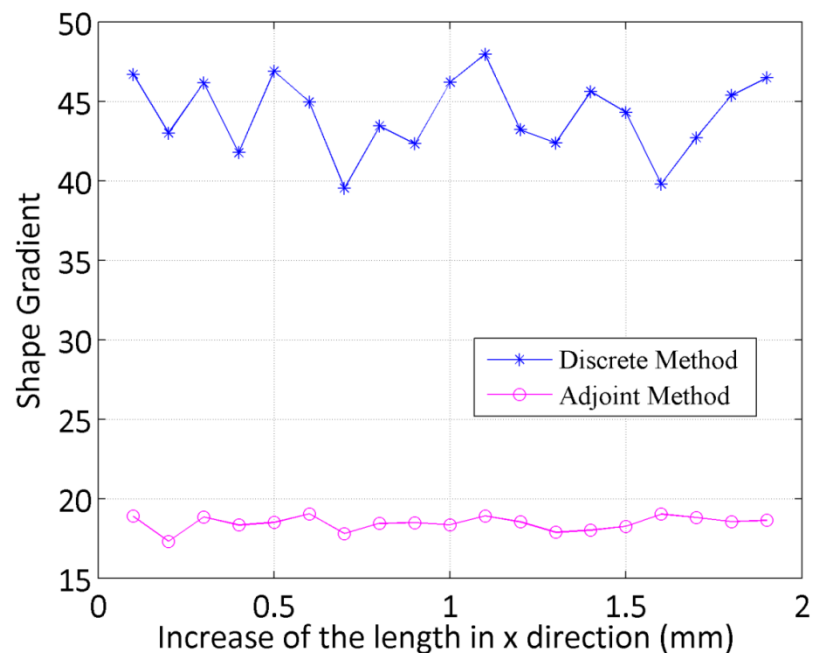


Figure 7.17: Shape derivative

From the results shown in Figure 7.17, we can also see large differences of shape gradient computed between the adjoint and discrete methods. Comparing the result of thin edge patch antenna, we can find that for both thin and thick 3D rectangular antenna structure, when we use the adjoint formula to compute the shape gradient of moving along a unique direction, we cannot obtain accurate values.

7.5 Shape Gradient Computation by Different Shape Deformations

In this study, we aim to investigate and validate the topological gradient method by comparing with the results using a geometrical modification method. We compute the shape gradient on a triangle on the edge of a circular antenna. The initial shape is a 10 cm radius circular antenna as shown in Figure 7.18, and the goal is a 5 cm radius circular antenna as shown in Figure 7.19.

We use one incident dipole illuminating from the far field, working at 3 GHz, and 72 measurements points to measure the scattered field. The moment of the incident dipole is $(0,1,0)$.

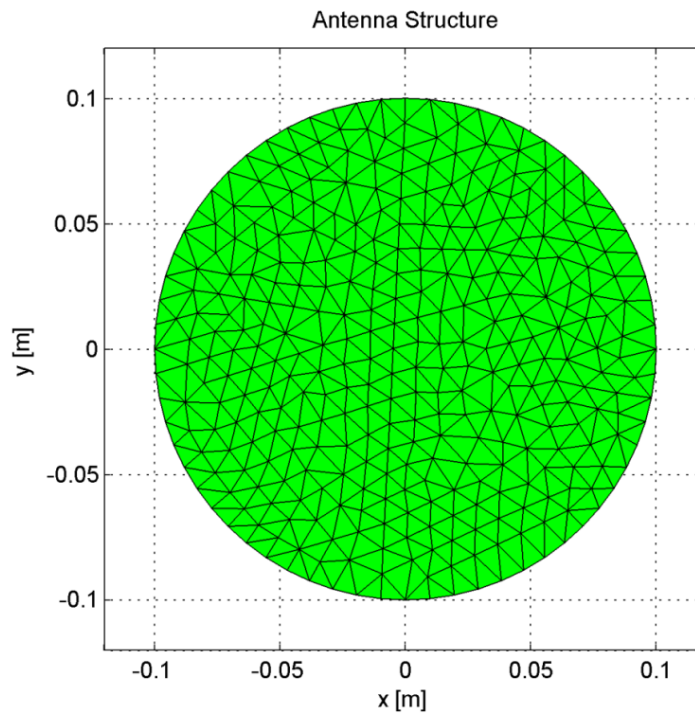


Figure 7.18: 10 cm radius circular antenna

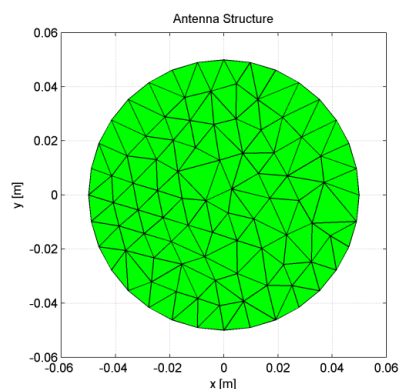


Figure 7.19: 5 cm radius circular antenna

We select the triangle #1 on the boundary to deform the shape of the initial guess as shown in Figures 7.20 and 7.21. The modification of the antenna geometry along the normal direction is associated with the length of segment on the boundary. For this case, we use $h=m*L$ to represent the maximum increase of h along the normal direction, m is a coefficient ranging from 0.05 to 0.5, with a step equal to 0.05, and L is 0.009814 m, the length of segment on the boundary. It means that the maximum of h is equal to half of the length of the segment on the boundary. The coordinates of the triangle summits are shown in Table 7.7.

Summit N#	x [m]	y [m]	z [m]
1	0.08467	-0.03389	0
2	0.09239	-0.03827	0
3	0.09569	-0.02903	0

Table 7.7: Summit Coordinates

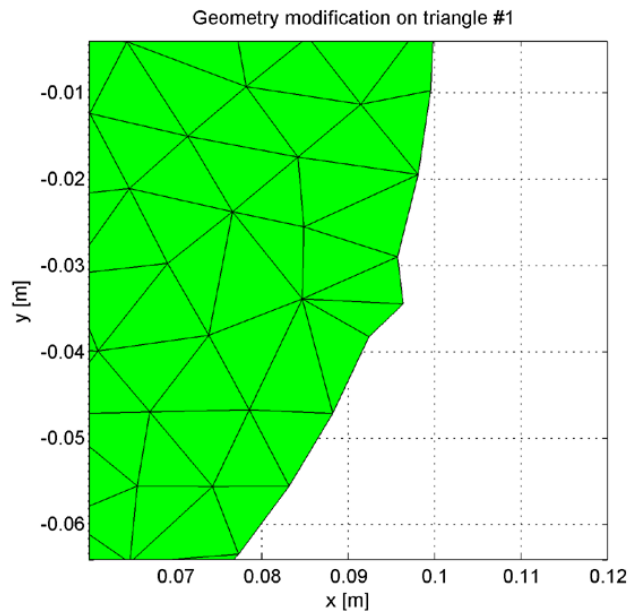


Figure 7.20: Geometry modification

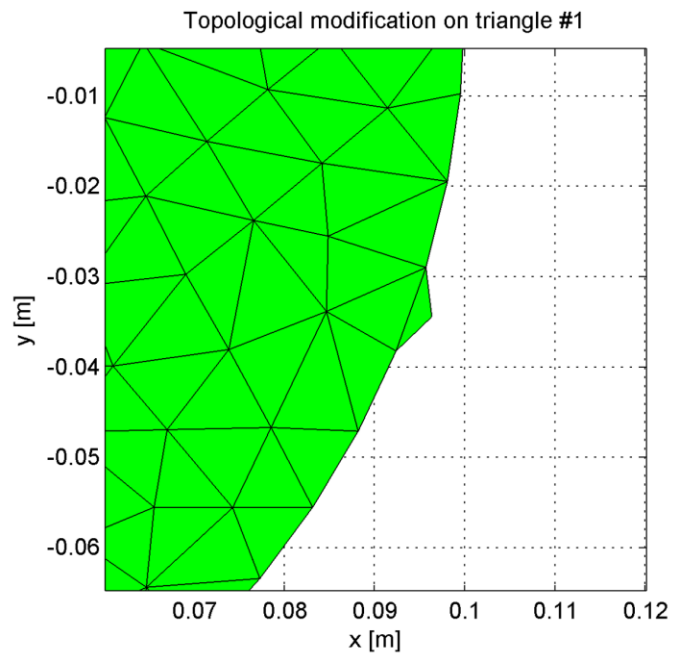


Figure 7.21 Topological modification

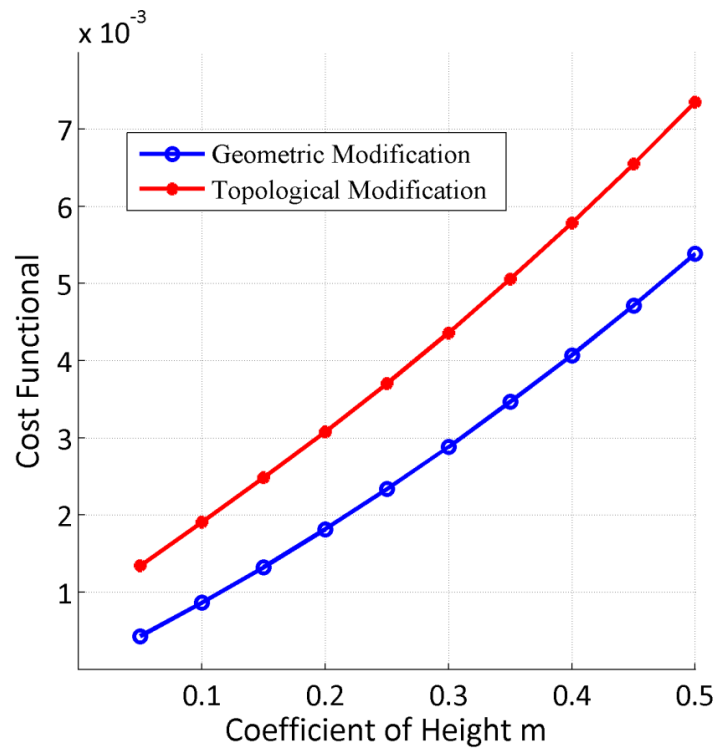


Figure 7.22 Cost functional versus Geometric and Topological Modification

The results in Figure 7.22 show when using geometric and topological modification, we have different values of the cost functional. In this case, the value of cost functional given by topological modification is always higher than the geometric one. However, as the shape gradient is related to the derivative of the cost functional, from the slope of the curve, we can find the shape gradients given by the topological and geometric are similar.

CHAPTER 8: NUMERICAL EXPERIMENTS

In this chapter, we present some numerical experiments of antenna optimization for different antenna configurations. The antennas and antenna arrays in these examples are illuminated by several dipoles from different locations with different incident moments, and measured at different points in the far or near-fields.

In the first optimization example, we use conjugate gradient method to optimize the antenna array location, and the location gradients for each element are computed by the analytical gradient method. Then, in order to perform the optimization capability, we optimize some shapes of single patch antenna and antenna arrays by using nodal point mesh derivation and topological gradient method. The optimization work contains:

1. Antenna array location optimization using conjugate gradient and analytical gradient method.
2. Shape Optimization of a single square patch antenna using nodal point mesh derivation.
3. Shape optimization of a single patch antenna.
4. Shape optimization of two rectangular patch antenna arrays using topological gradient.
5. Shape optimization of two circular patch antenna arrays.
6. Shape optimization of a single U-shape reflectarray element using topological gradient.

We also use multi-frequency and frequency-hopping techniques to implement different optimization strategies. In some examples, in order to test the robustness and accuracy of the optimization procedure, the algorithms are investigated with noise-corrupted data.

8.1 Antenna Array Location Optimization Using Conjugate Gradient and Analytical Gradient Methods

In this experiment, we optimize the location of 5*5 antenna arrays, and each patch element is defined with a $\lambda/4$ side. The original geometry is shown below in Figure 8.1.

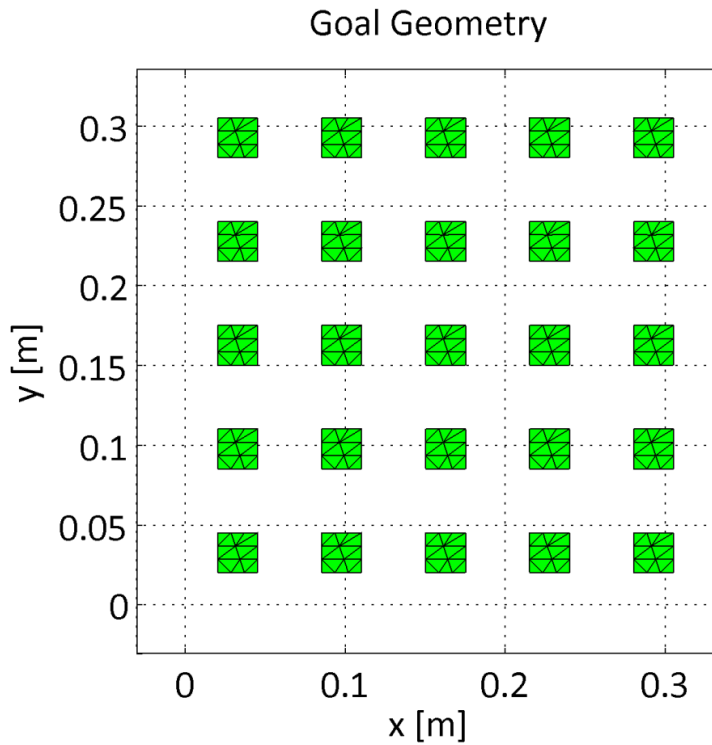


Figure 8.1: Goal Geometry

For the incident field, we use five electric dipoles with different moments defined in the Cartesian coordinates to illuminate the antenna array.

Dipole N#	Dipole Moment	x [m]	y [m]	z [m]
1	(0,1,0)	0.1625	0.1625	10
2	(0,1.732,1)	0.1625	-4.8375	8.66
3	(0,1,1.732)	0.1625	-8.4975	5
4	(0,1.732,-1)	0.1625	5.1625	8.66
5	(0,1,-1.732)	0.1625	8.8225	5

Table 8.1 Incident dipoles

In order to obtain uniform current densities over all the patches of the planar array, the dipoles are located in the far field. This experiment is aimed to

show the ability of the algorithm to optimize the location of antenna arrays. Meanwhile, we compare the differences between the single-frequency-single-incident wave and multi-frequency-multi-incident waves.

8.1.1 Illumination of Single-Frequency-Single-Incident Wave

First, we use five incident dipoles illuminating together, so that we obtain a single incident wave. The frequency of the incident is 3 GHz and we use a single frequency.

In order to define an initial guess, the patches have been moved away as shown in Figure 8.2, the initial guess is represented in red color, and the final geometry in blue color. The central element of the array is fixed during the optimization procedure.

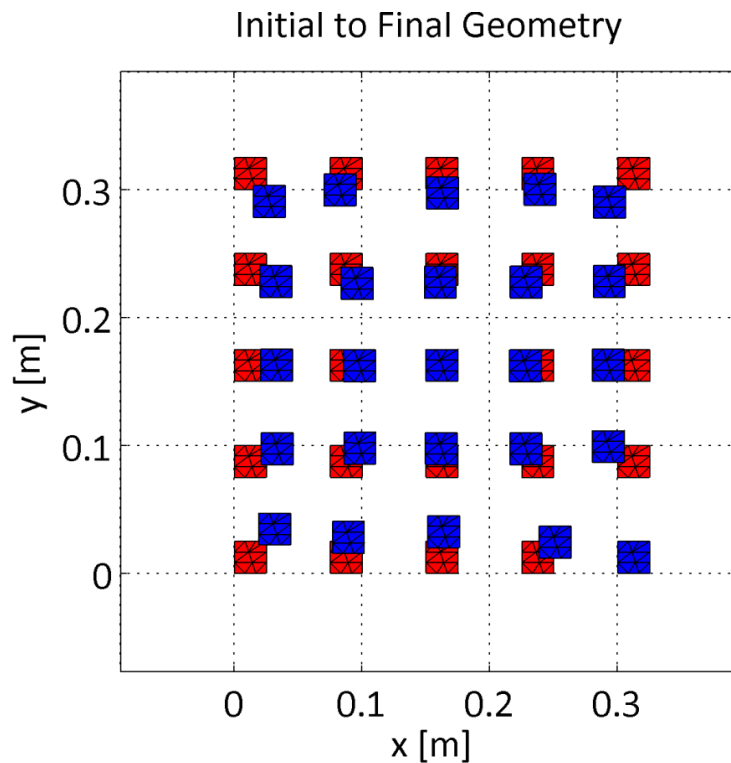


Figure 8.2: Initial and Final Geometry

The results illustrated in Figure 8.3 show that after 85 iterations, the value of the cost functional decreases to around 5.2×10^{-3} . However, from the final optimal geometry, the location of the initial guess cannot be fully optimized as the goal geometry, especially the element in the right corner is far from the goal.

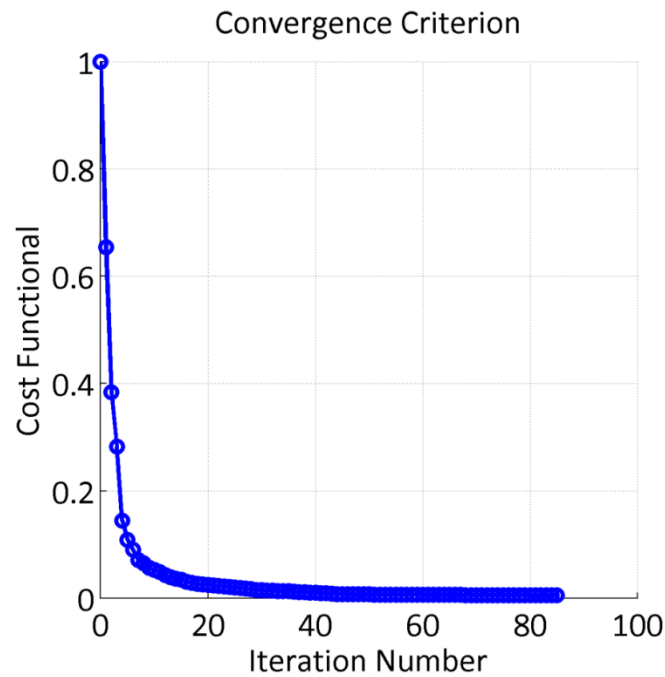


Figure 8.3a: Cost Functional vs. iteration number

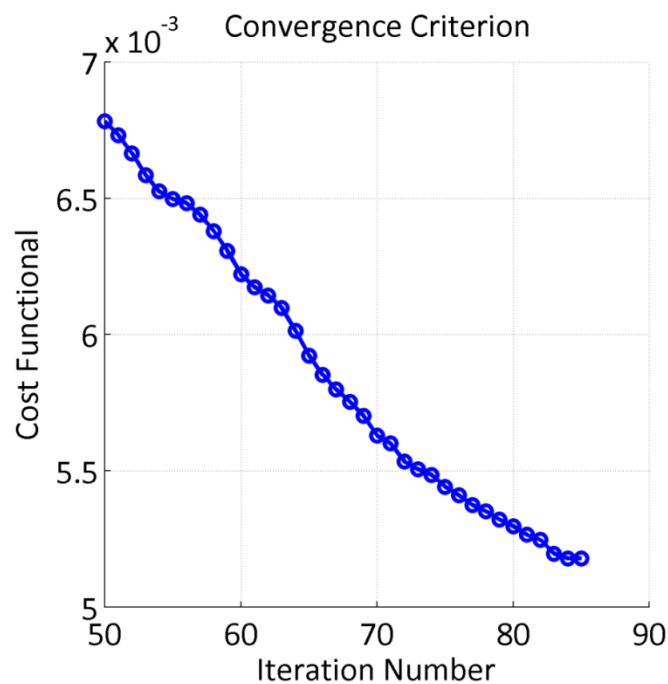


Figure 8.3b: Cost Functional vs. iteration number after 50 iterations

8.1.2 Illumination of Multi-Frequency-Multi-Incident Wave

For the second example, we utilize multi-frequency-multi-incident technique, and do not change the location and the moment of incident dipoles, but only the order, it means that the five incident dipoles illuminate separately, so that

we can obtain five different radiated patterns. Meanwhile, in this example, we also use five different incident frequencies as shown in Table 8.2 for different incident dipoles.

Dipole N#	Working Frequency (GHz)
1	3.0
2	2.8
3	2.6
4	3.2
5	3.4

Table 8.2 Working frequencies

From the final geometry given by Figure 8.4, we can find that the final geometry is very close to the goal geometry.

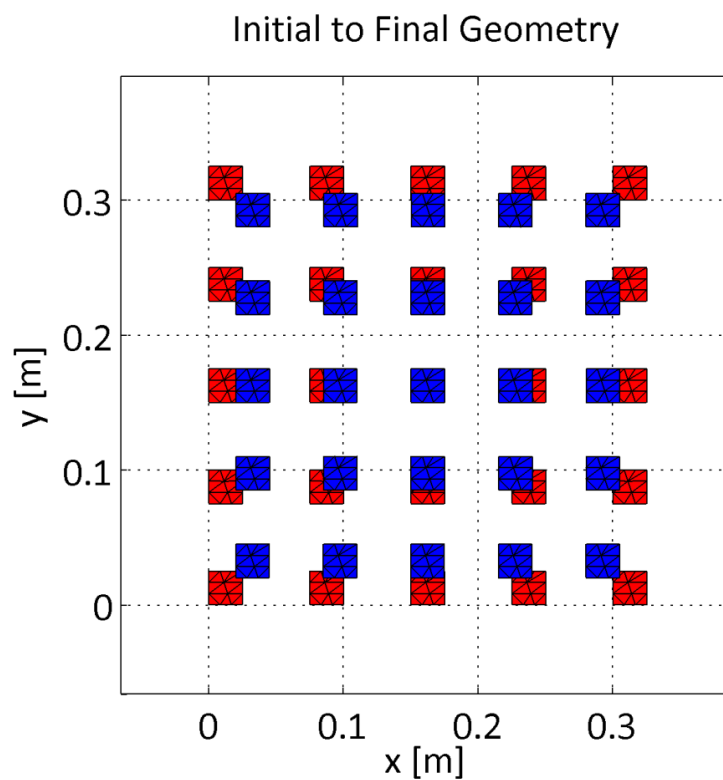


Figure 8.4: Initial and Final Geometry

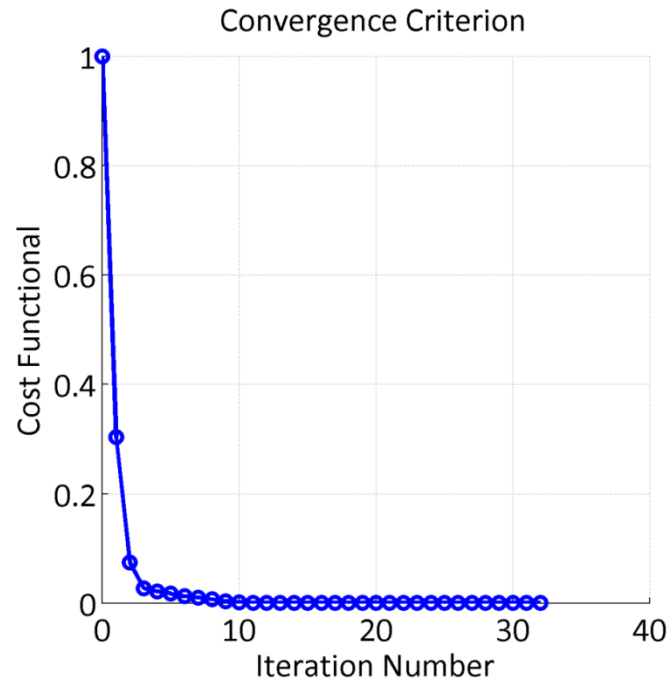


Figure 8.5a: Cost Functional vs. iteration number

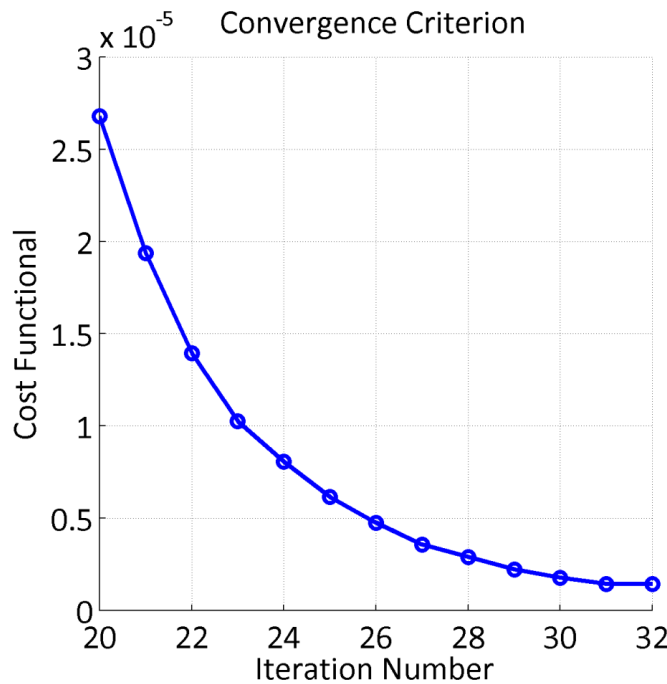


Figure 8.5b: Cost Functional vs. iteration number (after 20 iterations)

The results of convergence criterion in Figure 8.5 show that the criterion converges very fast. At the 32th iteration, the cost functional decreases to around 0.2×10^{-5} , which is more than 2500 times smaller than the value of cost functional at the 86th iteration using single-frequency-single-incident technique.

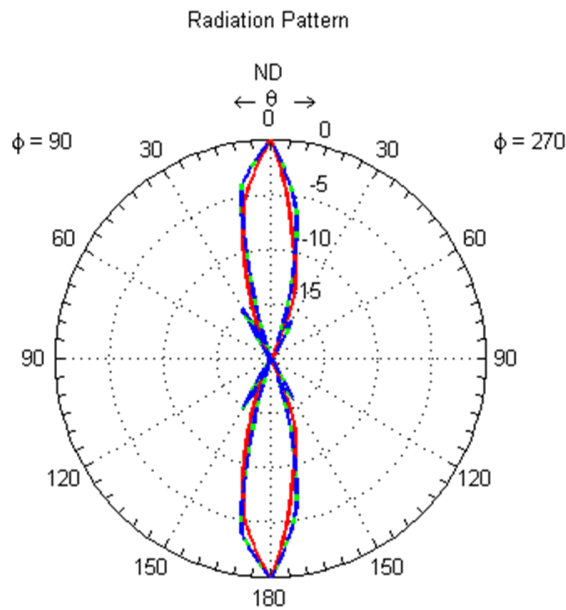


Figure 8.6a: Radiation Pattern

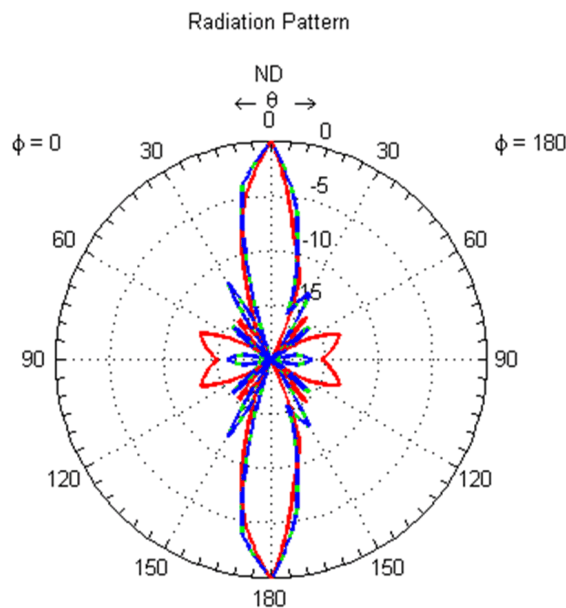


Figure 8.6b: Radiation pattern

The radiation pattern of the first incident dipole at 3 GHz in Figure 8.6 also shows that the scattered fields radiated by the final geometry and the goal are very close.

It can be concluded that when we optimize antenna or antenna arrays, multi-incident-multi-frequency is an important technique for accurate and fast

convergence optimization, because it contains more information and location sensitivity than a single-incident-single-frequency.

8.2 Shape Optimization of a Single Square Patch Antenna Using Nodal Point Mesh Derivation

In this study, we optimize a single 10 cm*10 cm square patch shown in Figure.8.7 from an initial guess. The shape gradient is computed by using nodal point mesh derivation.

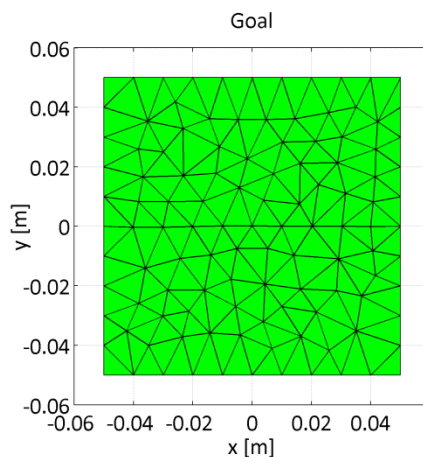


Figure 8.7: Goal Geometry

8.2.1 Shape Optimization from an Initial Guess in the Center

The initial guess is shown in Figure 8.8 with green mesh and the goal with blue line. The antenna is illuminated with 4 incident dipoles together, and optimized using a frequency hopping technique with two frequencies (1.5 and 3 GHz). With this illumination, the current on the antenna is more distributed close to the edge of antenna. 16 measurement points are selected to measure the electromagnetic field at the same distance from the origin of coordinate.

The results in Figures 8.9, and 8.10 show the performance of the algorithm. The optimization finally converges after 18 iteration steps at 3 GHz.

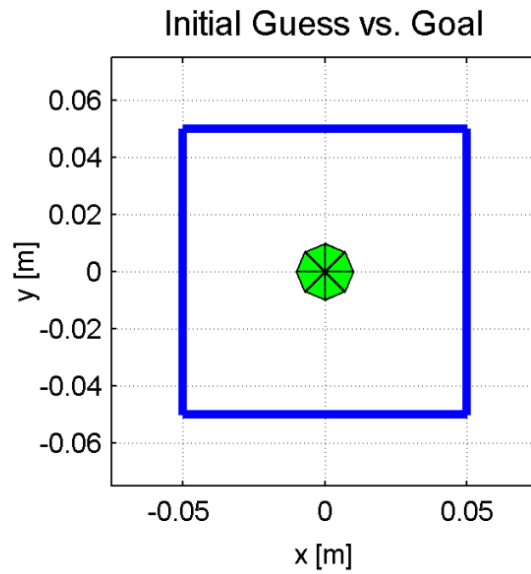


Figure 8.8: Initial guess vs. goal

Dipole N#	Dipole Moment	x [m]	y [m]	z [m]
1	(0,1,0)	0.25	0	0.25
2	(-1,0,0)	0	0.25	0.25
3	(0,-1,0)	-0.25	0	0.25
4	(1,0,0)	0	-0.25	0.25

Table 8.3: Incident dipoles

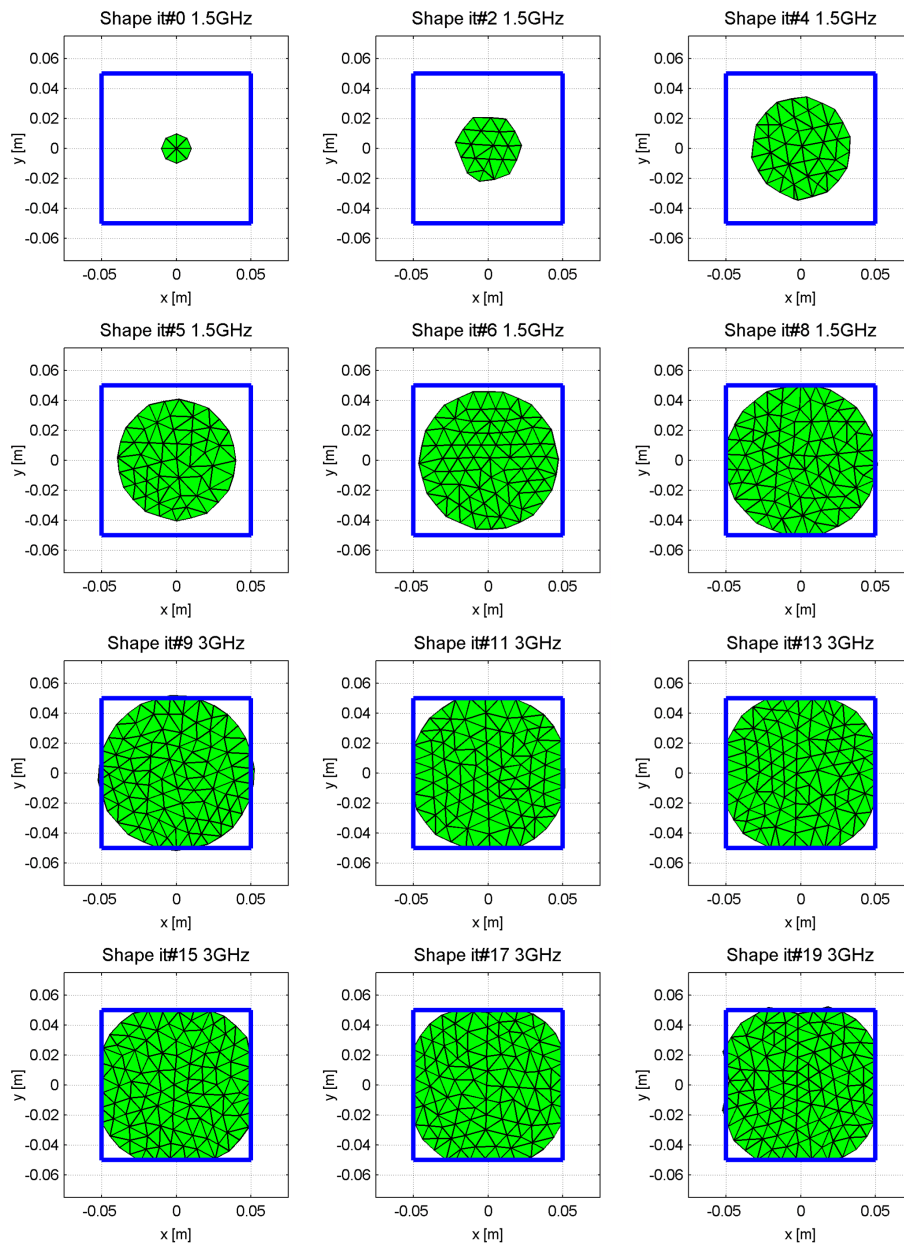


Figure 8.9: Shape evolutions using nodal point mesh derivation

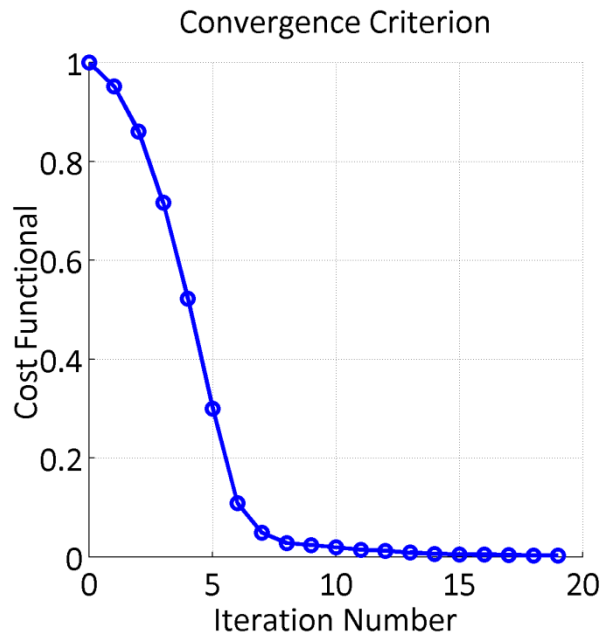


Figure 8.10: Cost Functional vs. iteration number

8.2.2 Shape Optimization from an Initial Guess in the Corner

Now, we move the initial guess from the center to the left corner of the goal (shown in Figure 8.13). We keep other information equivalently, while we change the first frequency to 750 MHz, and use other two frequencies (1.5 GHz and 3 GHz) with the frequency-hopping technique.

We can see from Figure 8.12 that after 26 iteration steps using frequency hopping technique with three frequencies (750 MHz, 1.5 and 3 GHz), the initial guess moves toward the center, and we can find the final shape very close to the goal geometry. After 15 iterations, the value of cost functional decreases to 0.26×10^{-2} .

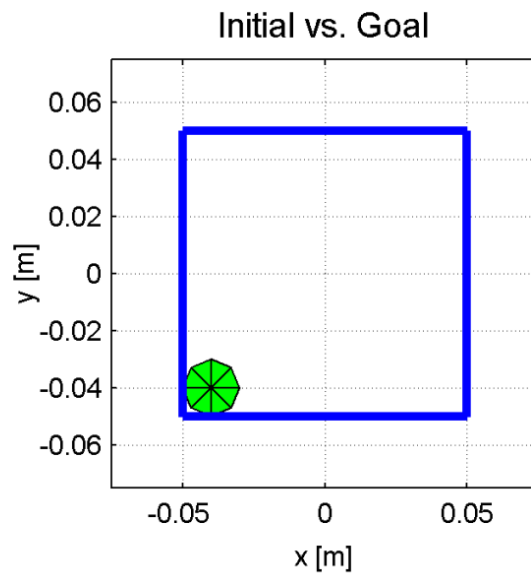


Figure 8.11: Initial Guess vs. Goal

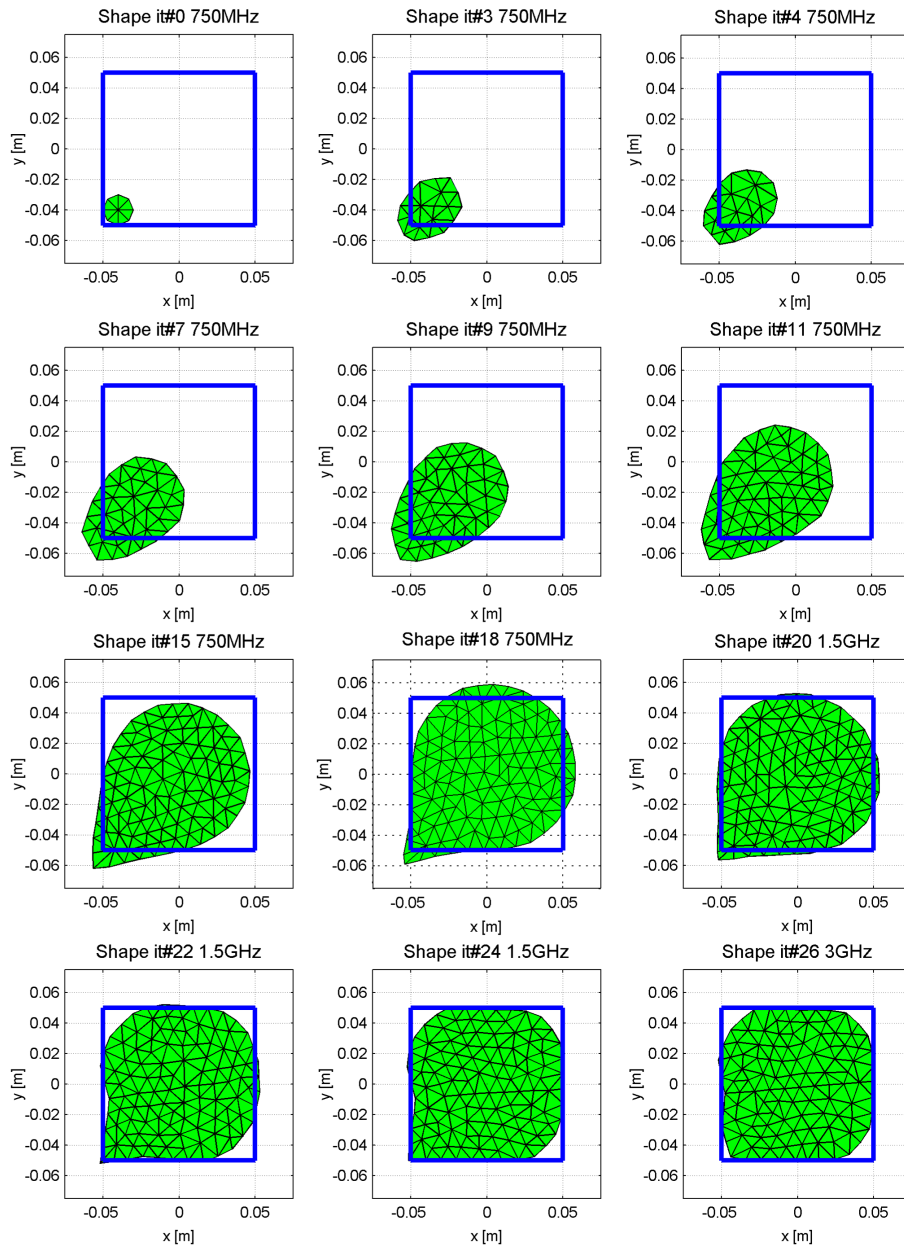


Figure 8.12: Shape evolution using nodal point mesh derivation

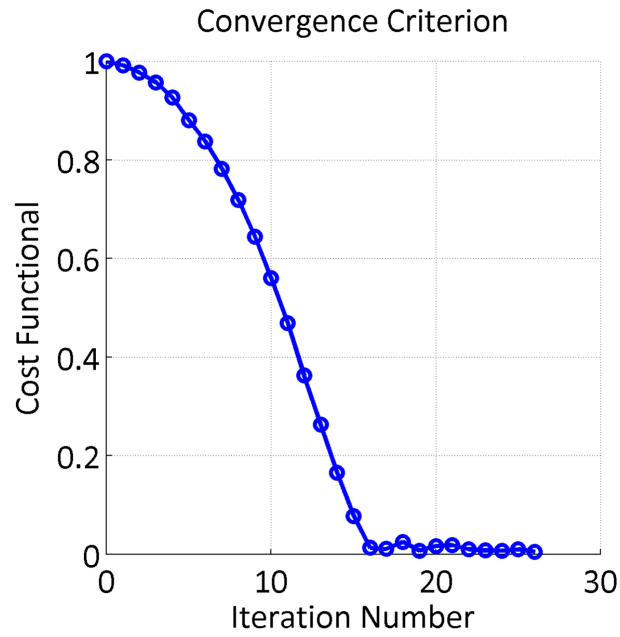


Figure 8.13a: Cost functional vs. iteration

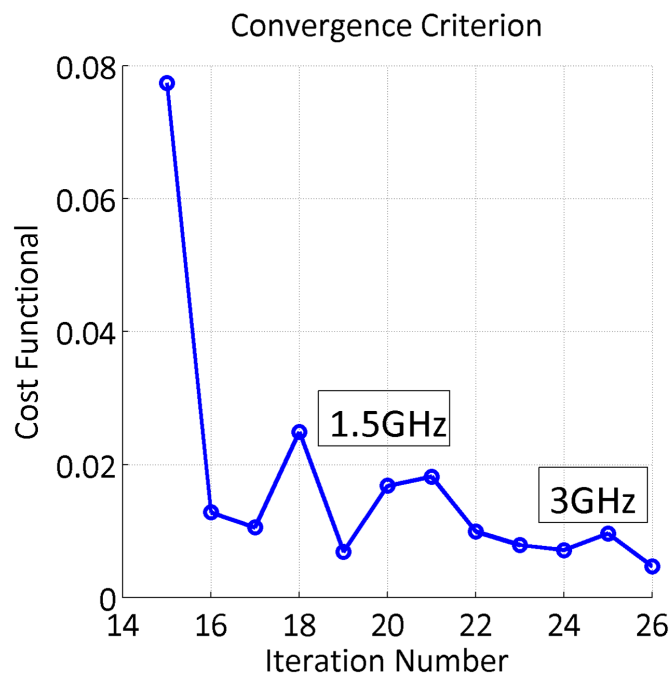


Figure 8.13b: Cost functional vs. iteration (from step 15)

The results of convergence criterion in Figure 8.13 show that the criterion converges finally. At the 15th iteration, the cost functional decreases to 0.47×10^{-2} .

8.3 Shape Optimization of a Single Patch Antenna

In this study, we optimize a single patch antenna shown in Figure.8.14. The antenna is illuminated by two incident dipoles as shown in Table 8.4, and the scatted fields are measured in the far field. The shape gradient is computed by using both nodal point mesh derivation and topological gradient method.

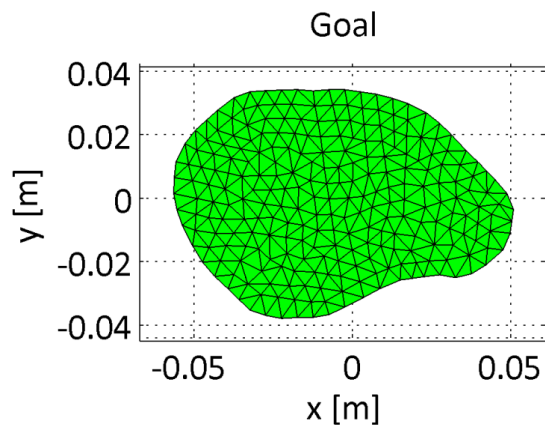


Figure 8.14: Goal Geometry

Dipole N#	Dipole Moment	x [m]	y [m]	z [m]
1	(0,1,0)	0	0	10
2	(1,0,0)	0	0	10

Table 8.4: Incident dipoles

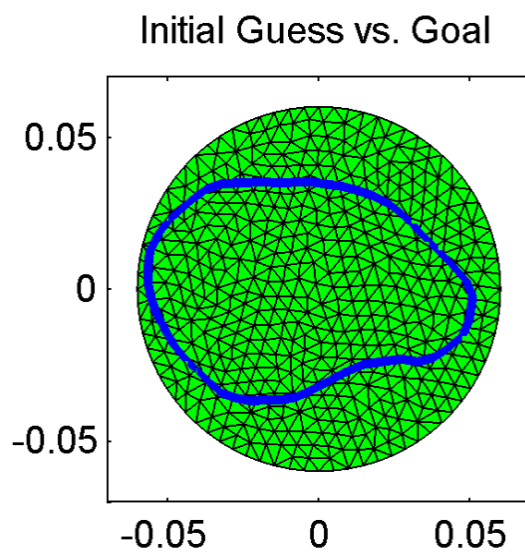


Figure 8.15: Initial Guess vs. Goal

The initial guess is a circular antenna shown with 12 cm diameter as shown with green mesh in Figure 8.15, and the goal is represented by a blue line.

8.3.1 Shape Optimization Using Nodal Point Mesh Derivation

We first use nodal point mesh derivation to compute the shape gradient. The results in Figures 8.16, and 8.17, show the performance of the algorithm for optimizing the shape of a single patch antenna of about 12 cm wide starting from the initial guess circle to the final result (after 11 iteration steps) using frequency hopping (1.5 GHz and 3 GHz).

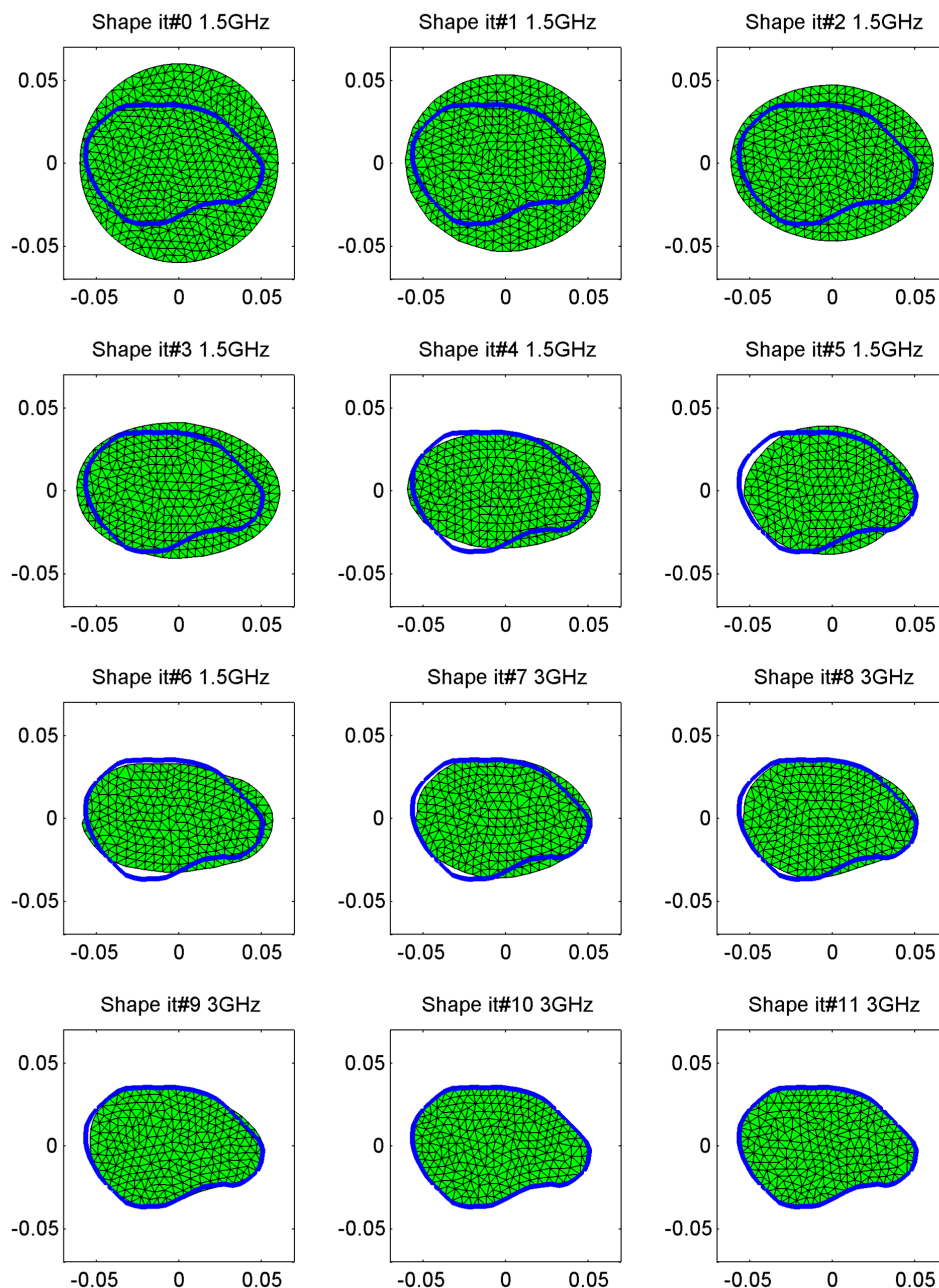


Figure 8.16: Shape evolution using nodal point mesh derivation

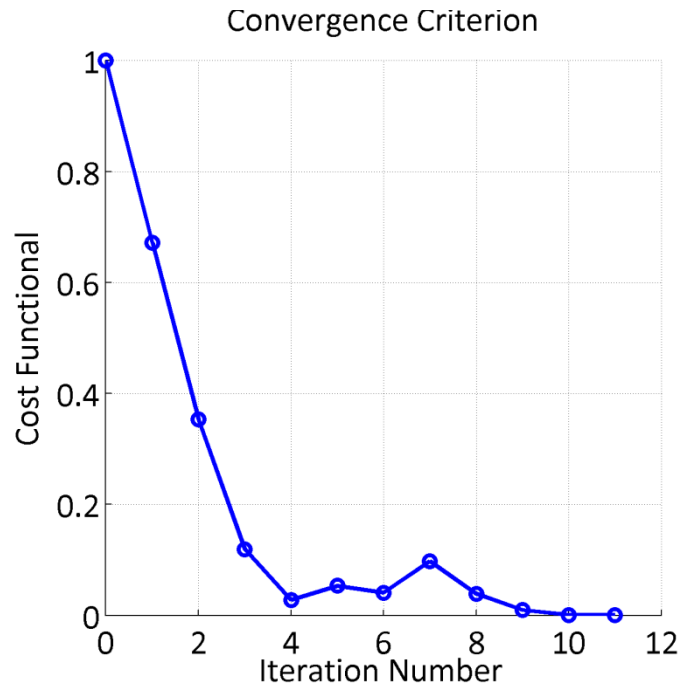


Figure 8.17a: Cost functional vs. iteration

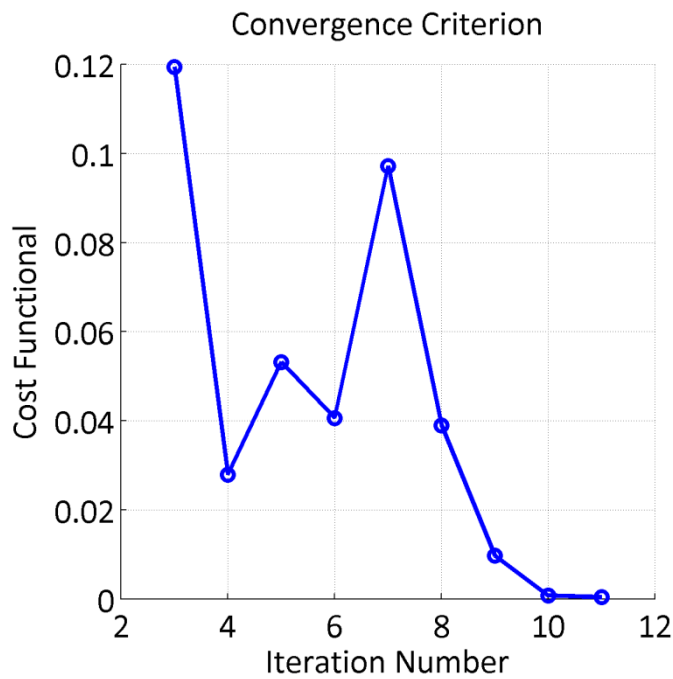


Figure 8.17b: Cost functional vs. iteration (from step 3)

The results of convergence criterion in Figure 8.17 show that the criterion converges very fast. At the 15th iteration, the cost functional decreases to 0.39×10^{-3} . At the 7th iteration, the value of cost functional increases as the frequency shifts from 1.5 GHz to 3 GHz.

8.3.2 Shape Optimization Using Topological Gradient without Noise

Now, we change our strategy to use the topological gradient method to compute the shape gradient. The results illustrated in Figures 8.18, and 8.19, show the performance of the algorithm for optimizing the shape of a single patch antenna of about 10 cm wide starting from the initial guess circle to the final result (after 18 iteration steps) using frequency hopping technique with two frequencies (1.5 and 3 GHz). Comparing the results by using nodal point mesh derivation, we can obtain almost the same optimal geometry.

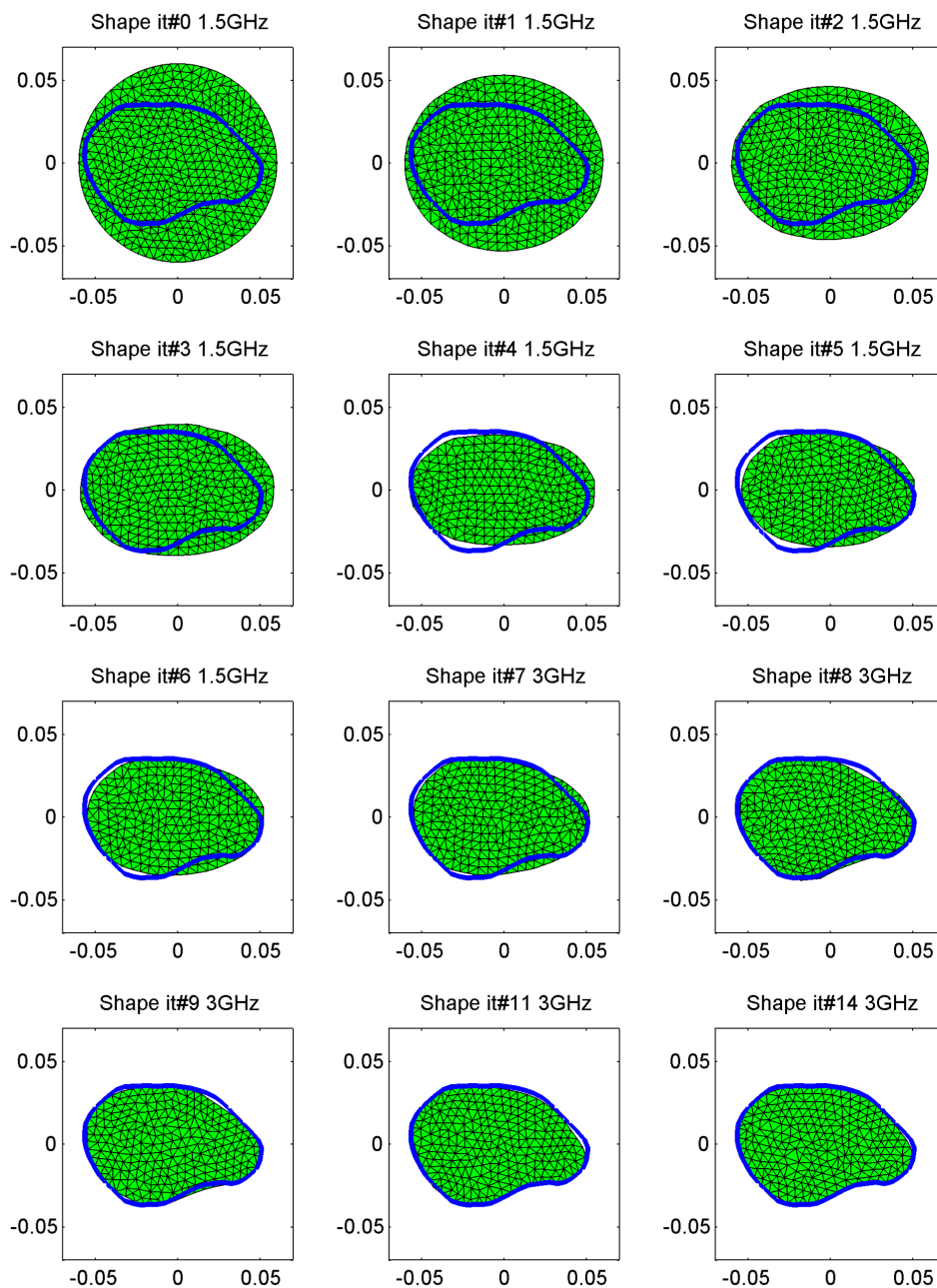


Figure 8.18: Shape evolution using topological shape gradient

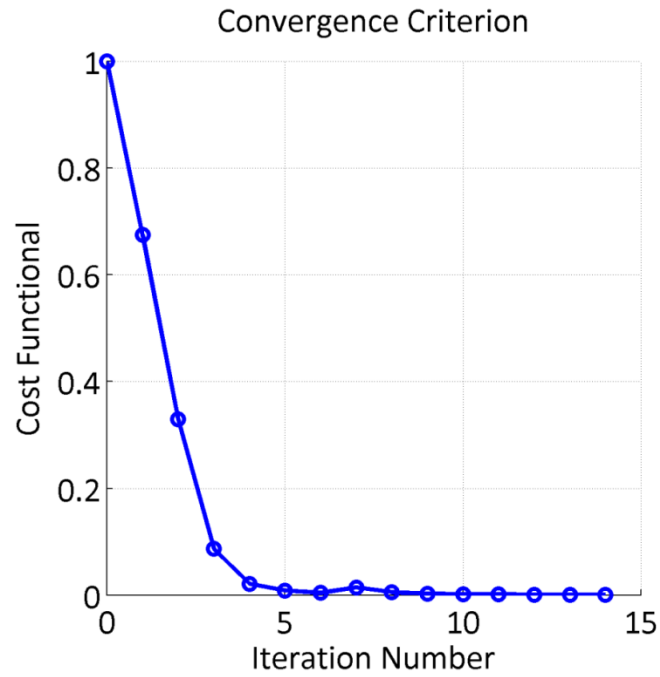


Figure 8.19a: Cost functional vs. iteration

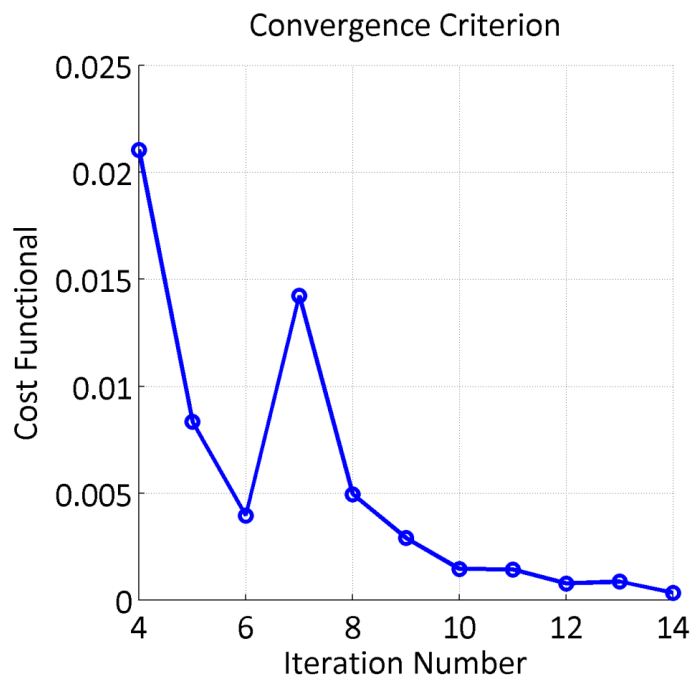


Figure 8.19b: Cost functional vs. iteration (from step 4)

The results of convergence criterion illustrated in Figure 8.19 show that the criterion converges very fast. At the 14th iteration, the cost functional decreases to 0.33×10^{-3} . At the 7th iteration, the value of cost functional increases as the frequency shifts from 1.5 GHz to 3 GHz.

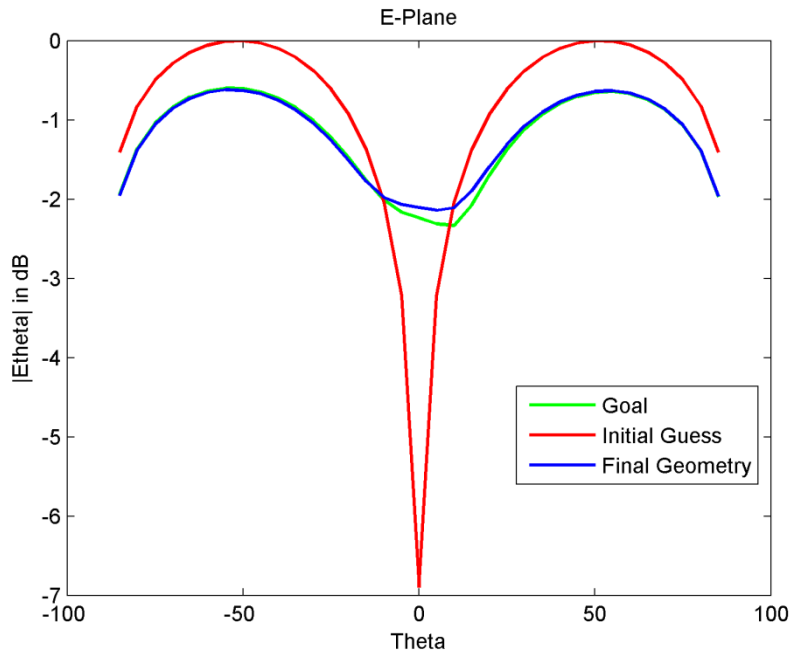


Figure 8.20a: Normalized radiation pattern of E-Plane

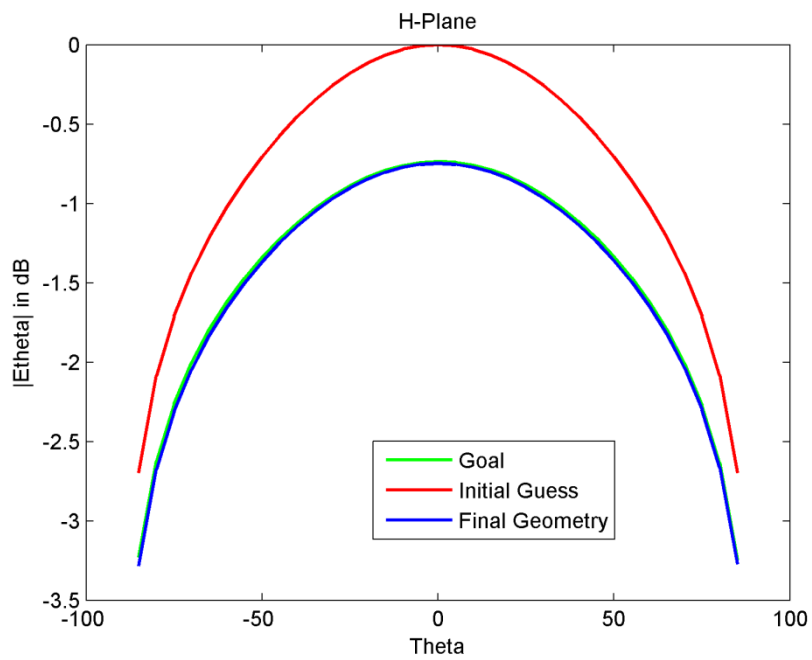


Figure 8.20b: Normalized radiation pattern of H-Plane

The radiation pattern of the first incident dipole at 1.5GHz in Figure 8.20 shows that the scattered fields radiated by the final geometry and goal are close.

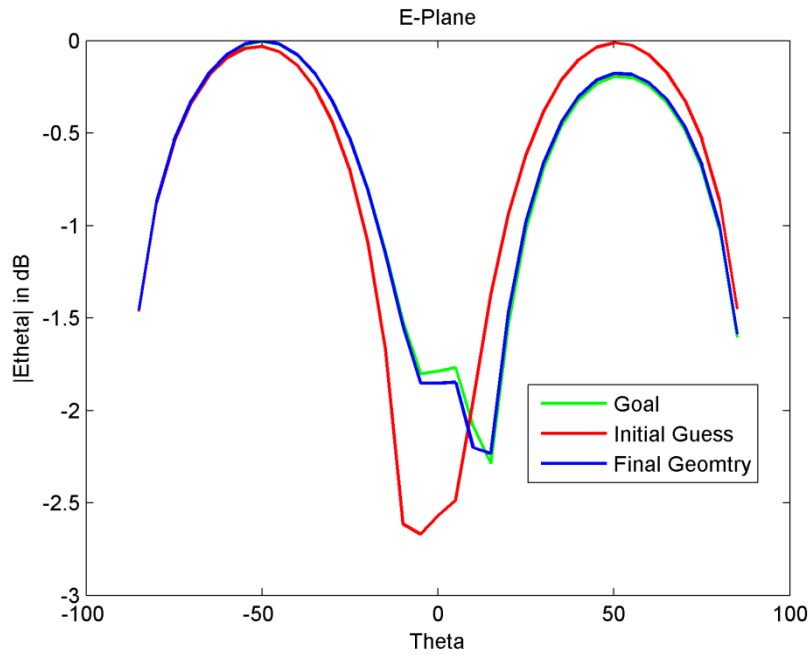


Figure 8.21a: Normalized radiation patter of E-Plane

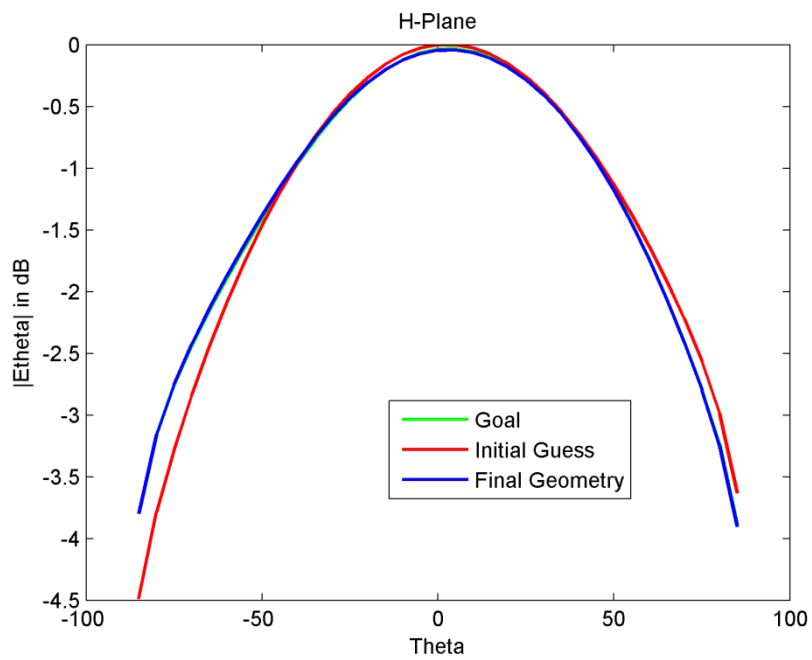


Figure 8.21b: Normalized radiation pattern of H-Plane

Figure 8.21 shows the scattered fields of the first incident dipole at 3 GHz radiated by the initial guess, final and goal geometry. After several iterations, the radiation pattern radiated by the goal can be found.

8.3.3 Shape Optimization Using Topological Gradient with 20 dB Noise

For the third example, we keep the same strategy for the optimization procedure, and start from the same initial guess, but 20 dB noise is added to the radiation of goal for a test of robustness. A frequency-hopping technique is used for the optimization procedure at 1.5 GHz and 3 GHz.

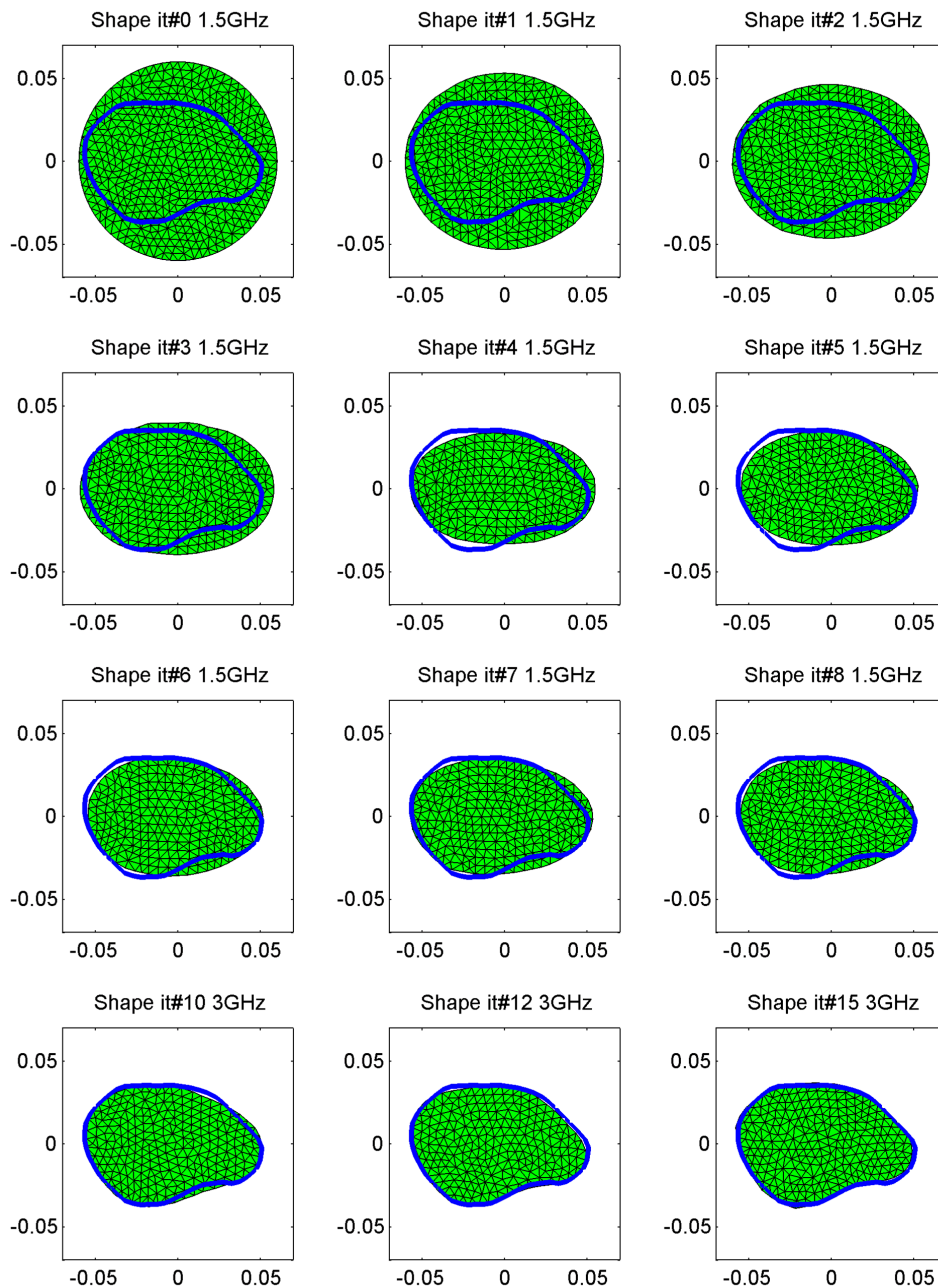


Figure 8.22: Shape evolution using topological shape gradient

From the figure 8.22, we can see that after 15 iterations, the patch antenna evolves to the final shape, and shows a good match comparing with the goal in blue line.

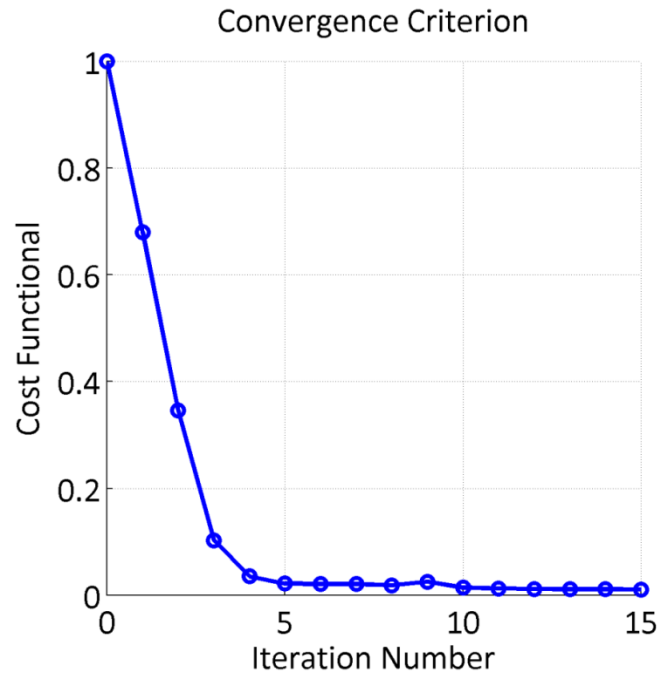


Figure 8.23a: Cost functional vs. iteration

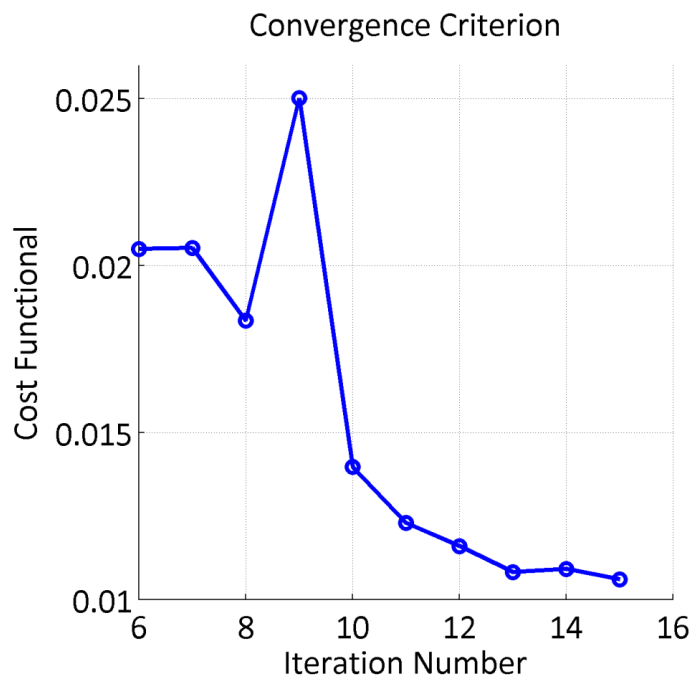


Figure 8.23b: Cost functional vs. iteration (from step 4)

The results of convergence criterion illustrated in Figure 8.23 show that the criterion converges very fast. At the 15th iteration, the cost functional decreases to 0.11×10^{-1} .

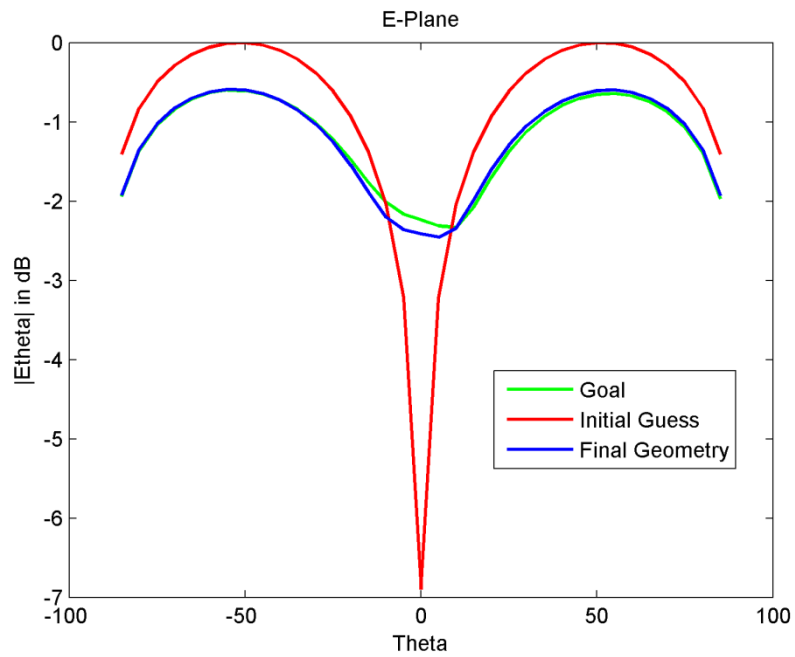


Figure 8.24a: Normalized radiation pattern of E-Plane

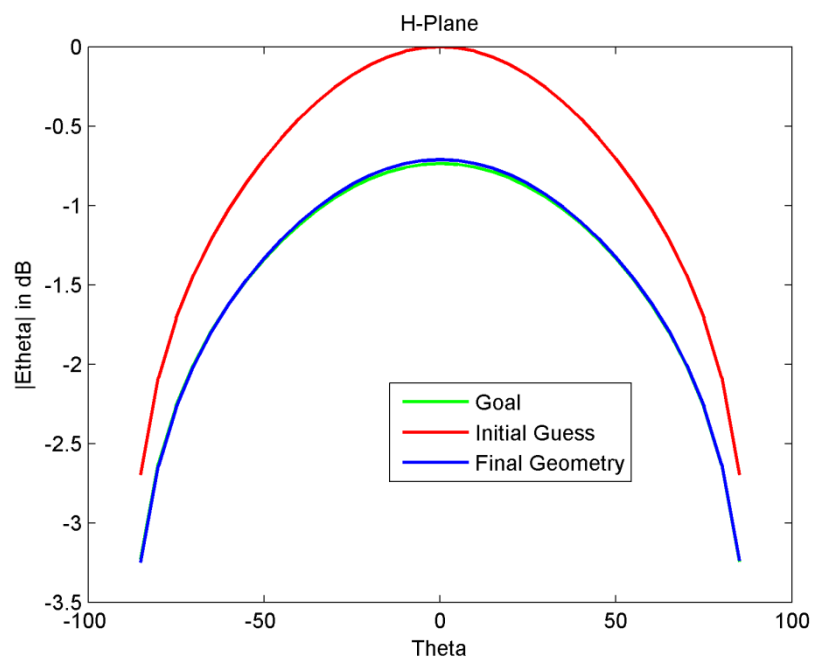


Figure 8.24b: Normalized radiation pattern of E-Plane

The radiation pattern of the first incident dipole at 1.5GHz in Figure 8.24 shows that the scattered fields radiated by the final geometry and goal are closed.

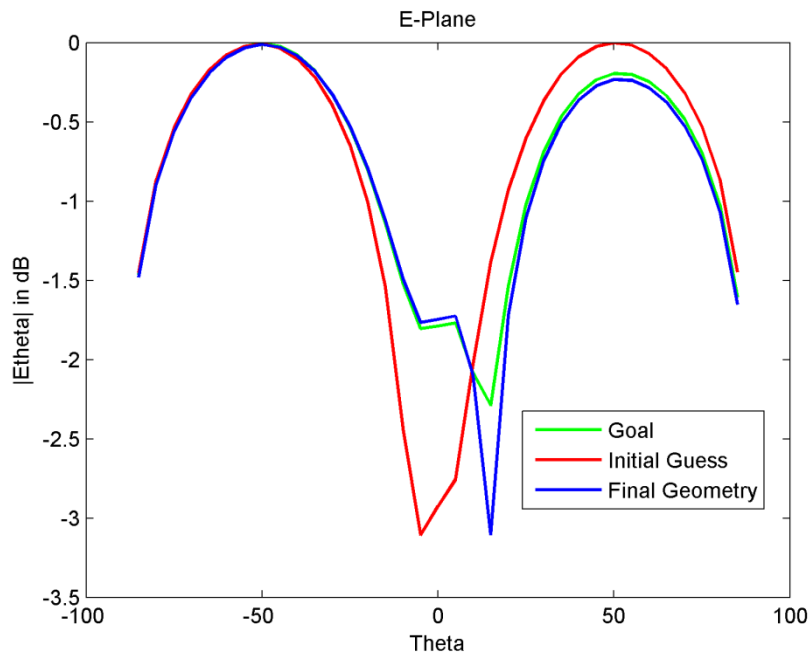


Figure 8.25a: Normalized radiation pattern of E-Plane

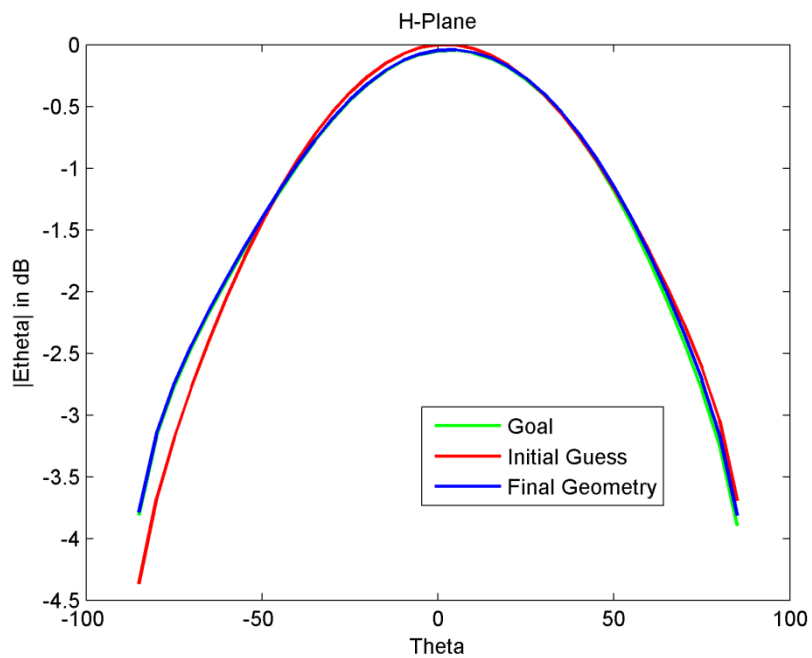


Figure 8.25b: Normalized radiation pattern of E-Plane

Figure 8.25 show the scattered fields of the first incident dipole at 3 GHz radiated by the initial guess, final and goal geometry. After several iterations, the radiation pattern radiated by the goal can be found finally. However, from Figure 8.25a, we can see some difference between the radiation pattern of the goal and final geometry.

8.3.4 Shape Optimization Using Topological Gradient with 10 dB Noise

Now, comparing with the last experiment, we keep the same strategy for the optimization procedure, and start from the same initial guess, but this time we add 10 dB to the radiation of goal for the robustness test. Frequency-hopping technique is also used for the optimization procedure at 1.5 GHz and 3 GHz.

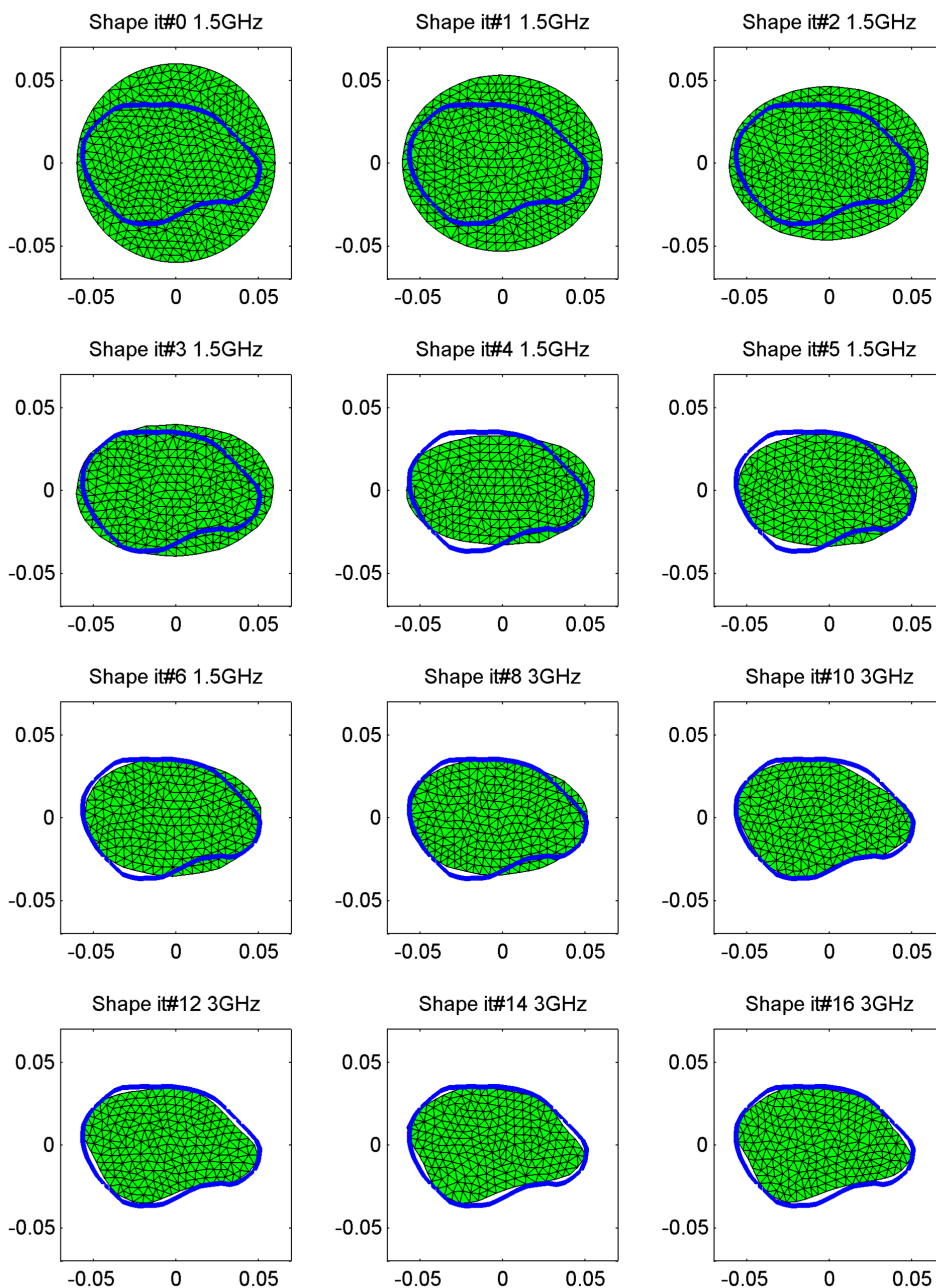


Figure 8.26: Shape evolution using topological shape gradient

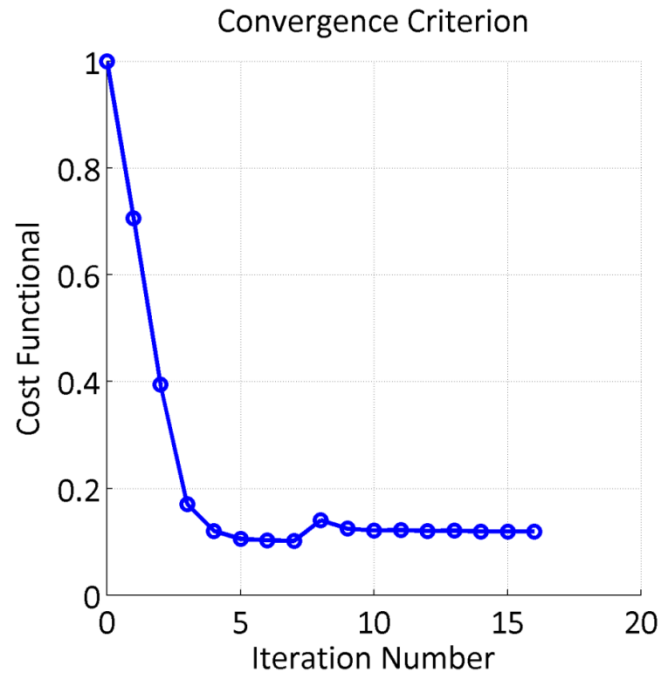


Figure 8.27a: Cost functional vs. iteration

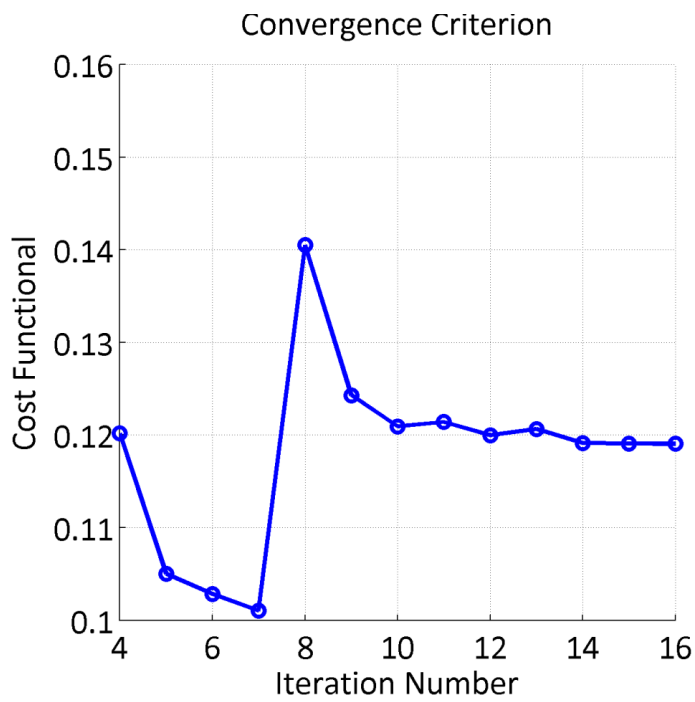


Figure 8.27b: Cost functional vs. iteration (from step 4)

The results of convergence criterion shown in Figure 8.27 illustrate that the criterion converges at 16th iteration, but the cost functional does not reach to a low value, but around 0.119.

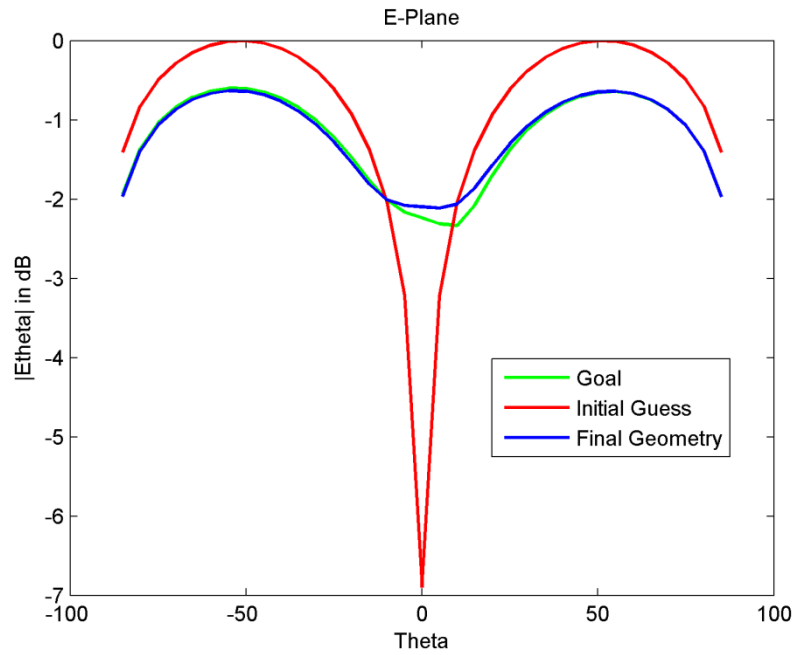


Figure 8.28a: Normalized radiation pattern of E-Plane

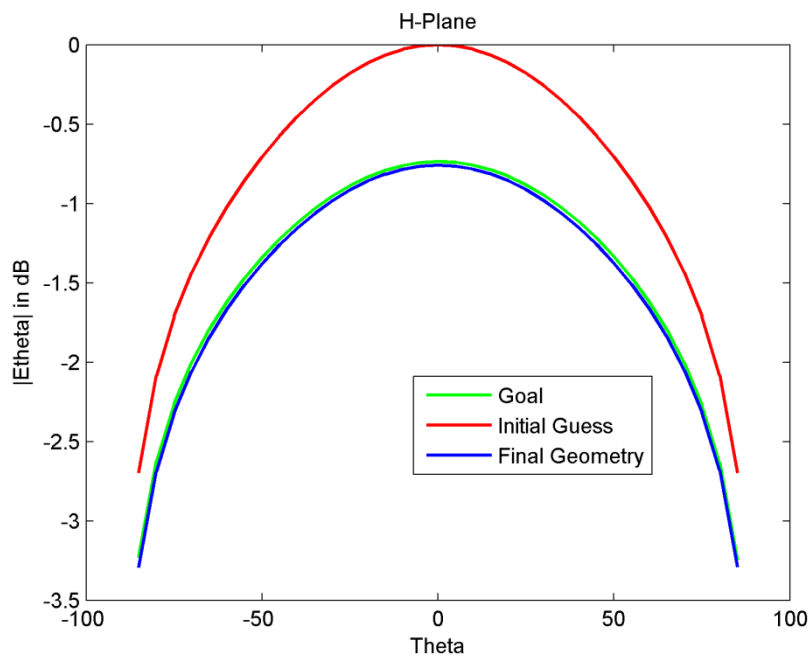


Figure 8.28b: Normalized radiation pattern of H-Plane

The radiation pattern of the first incident dipole at 1.5 GHz illustrated in Figure 8.28 shows that the scattered fields radiated by the final geometry and goal are close.

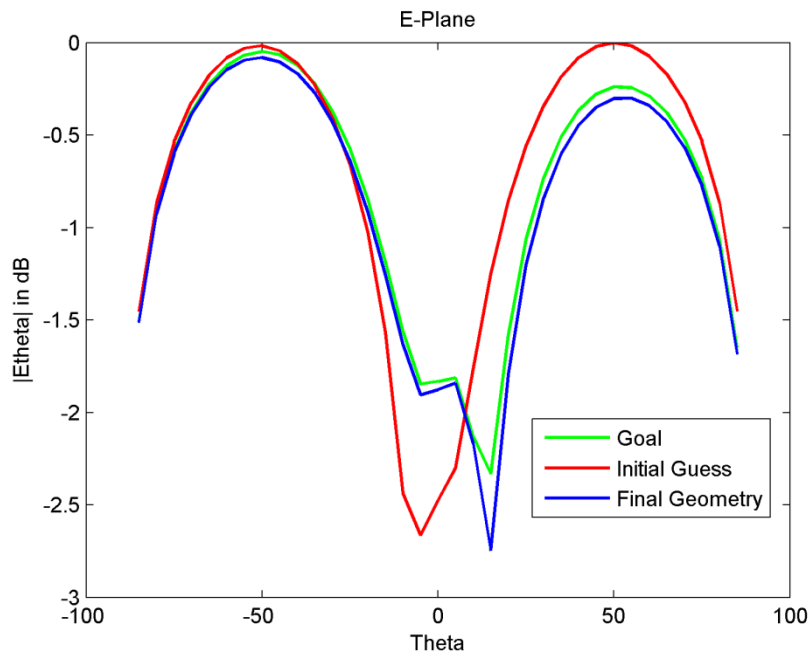


Figure 8.29a: Normalized radiation pattern of E-Plane

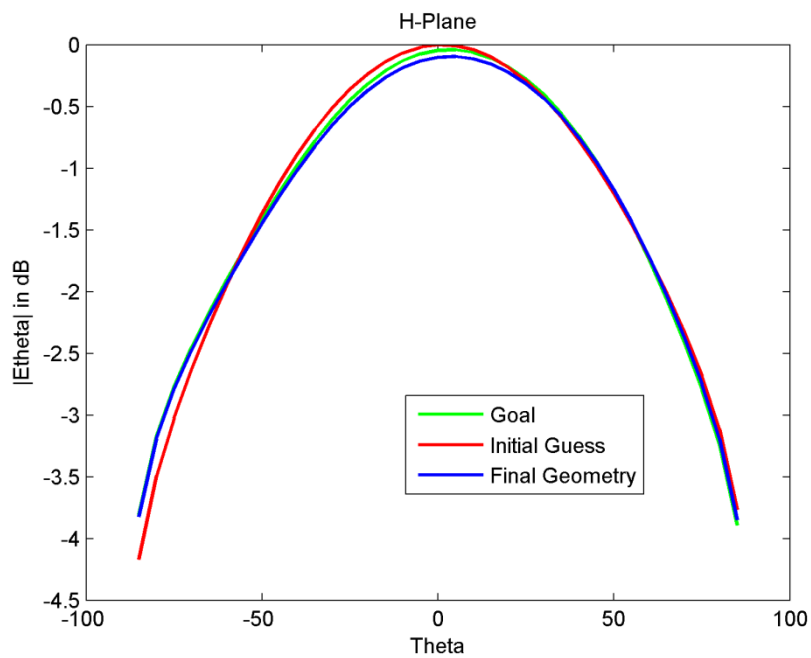


Figure 8.29b: Normalized radiation pattern of H-Plane

Figure 8.29 shows the scattered fields of the first incident dipole at 3 GHz radiated by the initial guess, final geometry and goal. After several iterations, the radiation pattern radiated by the goal and the final geometry shows some similarity, but they are not fully matching.

8.4 Shape Optimization of Two Rectangular Patch Antennas Using Topological Gradient

In this study, we optimize two rectangular patch antennas shown in Figure 8.30. The shape gradient is computed by using topological gradient method. The two antennas are illuminated by two incident dipoles working at a single frequency 3 GHz as shown in Table 8.4, and the scattered fields are measured in the far field.

Dipole N#	Dipole Moment	x [m]	y [m]	z [m]
1	(0,1,0)	0	0	10
2	(1,0,0)	0	0	10

Table 8.4: Incident dipoles

The initial guess is two circular antennas with 14 cm diameter and 40 cm far from each other as shown in Figure 8.31, and the goal is represented by blue line. The size of a single rectangular antenna is 5 cm*10 cm.

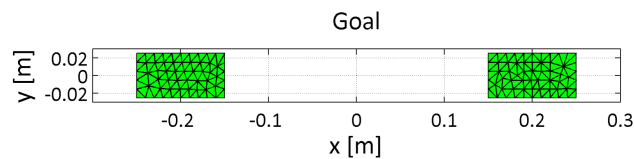


Figure 8.30: Goal Geometry

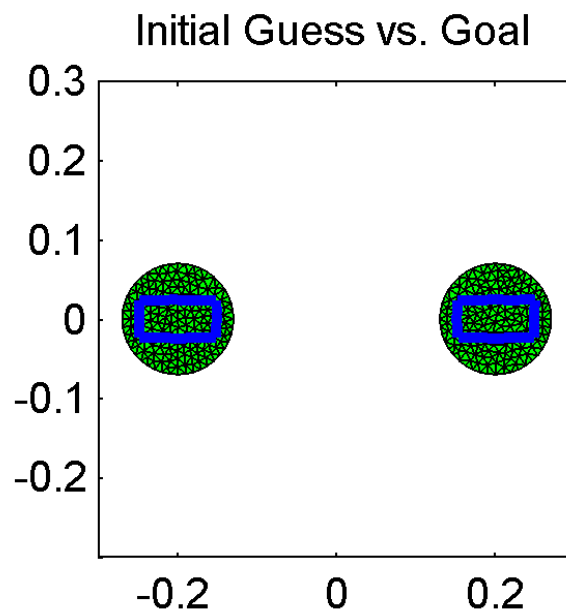


Figure 8.31: Initial Guess vs. Goal

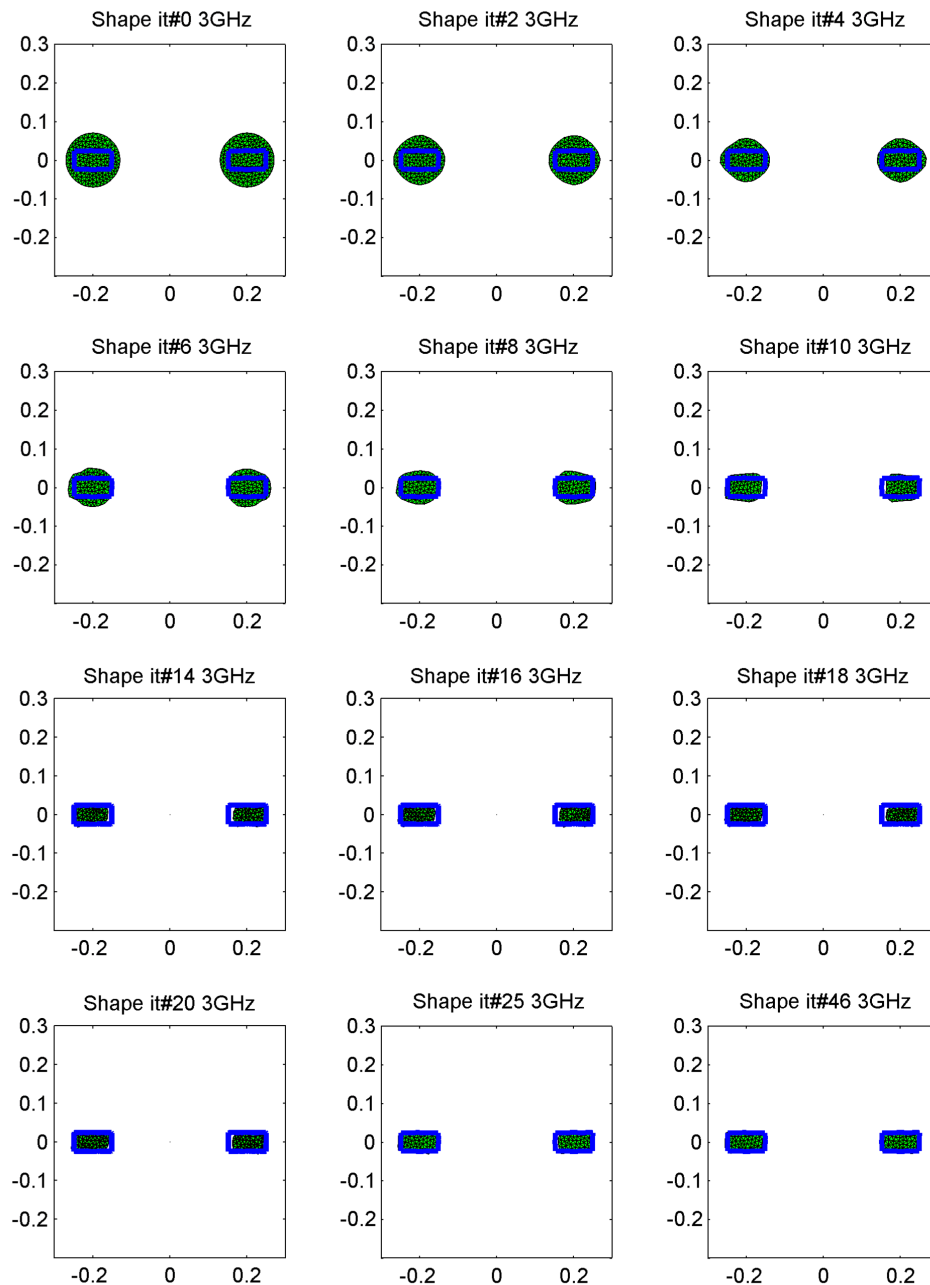


Figure 8.32: Shape evolution using Topological Gradient

The results illustrated in Figures 8.32 and 8.33 show the performance of the algorithm using topological gradient derivation for the optimization. We can see that after 46 iteration steps using just one single frequency at 3 GHz, the initial guess evolves from two circular antennas toward two rectangular antennas, and we can find the final optimized shape is similar to the goal geometry.

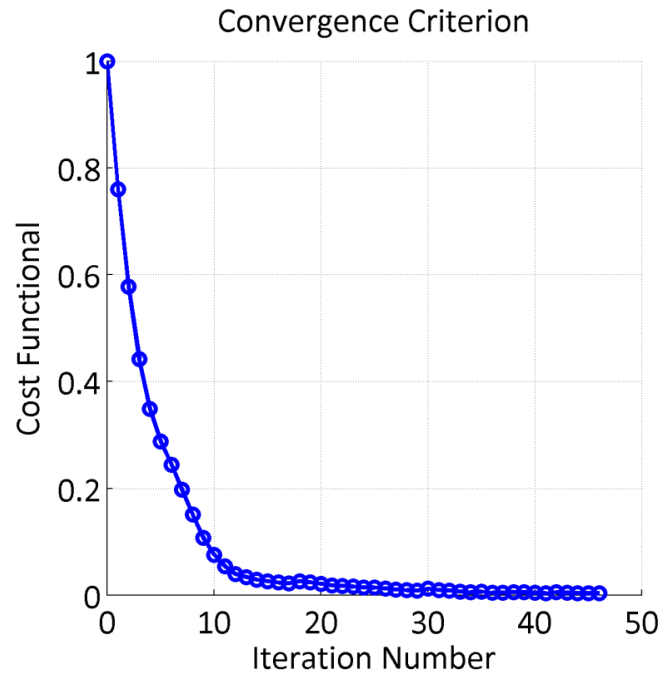


Figure 8.33: Cost functional vs. iteration

The results of convergence criterion illustrated in Figure 8.23 show that the criterion converges very fast. At the 46th iteration, the cost functional decreases to 0.42×10^{-2} .

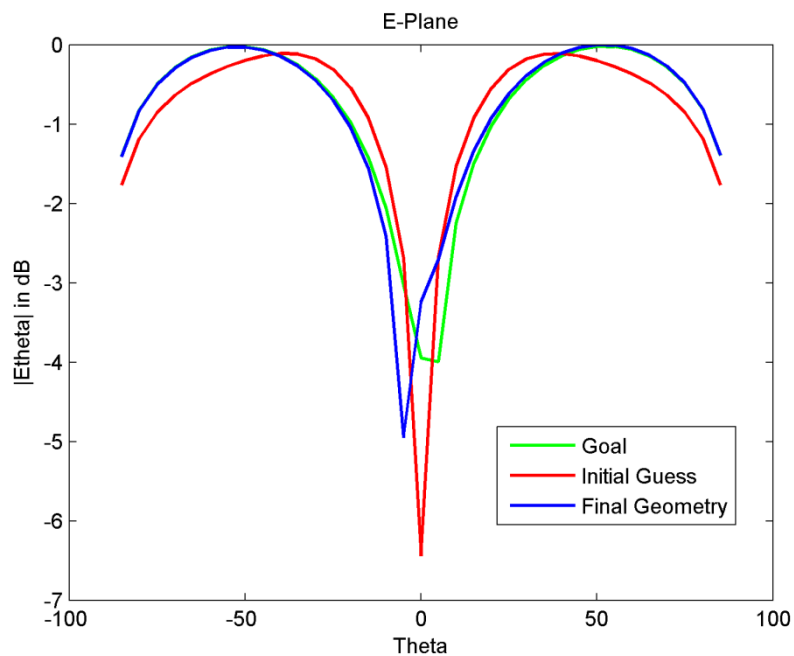


Figure 8.34a: Normalized radiation pattern of E-Plane

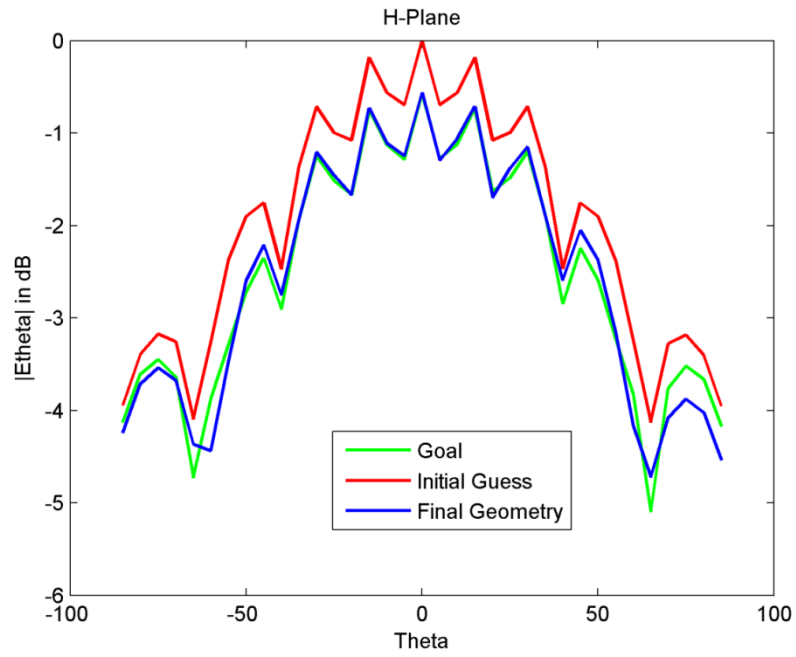


Figure 8.34b: Normalized radiation pattern of H-Plane

Figure 8.34 shows the scattered fields of the first incident dipole at 3 GHz radiated by the initial guess, final and goal geometry. After several iterations, the radiation pattern radiated by the goal can be found.

8.5 Shape Optimization of Two Circular Patch Antennas

In this study, we optimize two circle patch antennas (5 cm radius) shown in Figure 8.35. The initial guess starts from a rectangular patch in Figure 8.36 represented by the green mesh. We first use Frequency-hopping technique for the optimization procedure, and we compare the results with the multi-frequency technique. The two antennas are illuminated by two incident dipoles working at different frequencies as shown in Table 8.5, and the scatted fields are measured in the far field.

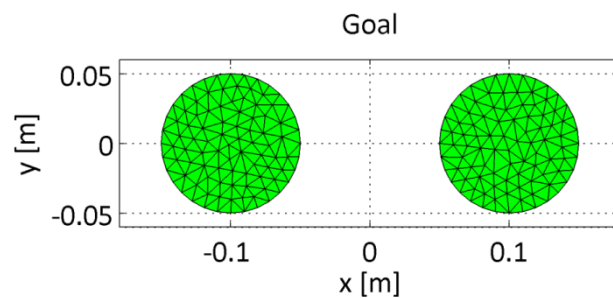


Figure 8.35: Goal Geometry

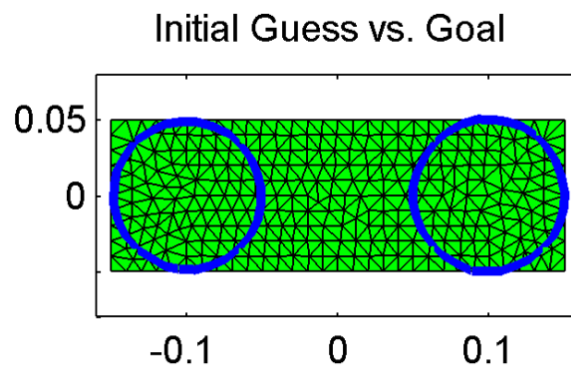


Figure 8.36: Initial Guess vs. Goal

Dipole N#	Dipole Moment	x [m]	y [m]	z [m]
1	(1,1,0)	0	0	10
2	(-1,1,0)	0	0	10
3	(0,1,0)	0	0	10

Table 8.5: Incident dipoles

8.5.1 Shape Optimization Using Frequency-Hopping Technique

a. Optimization Starting from 1 GHz Using Frequency-Hopping

We first optimize starting from 1 GHz. The figures 8.37 and 8.38 show that the two antennas cannot be optimized after 5 iterations as at the 5th iteration, the value of cost functional is around 0.73, and greater than the previous one.

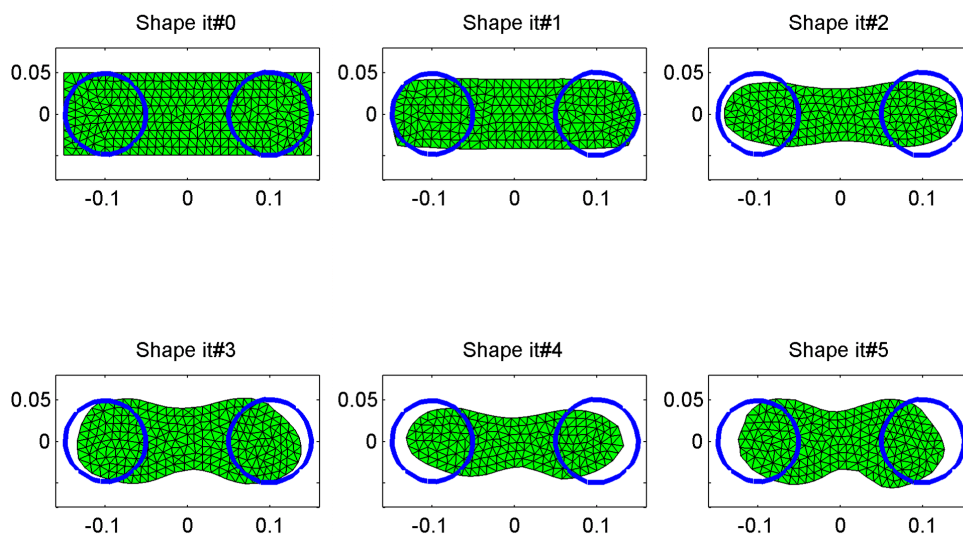


Figure 8.37: Shape evolution at 1 GHz

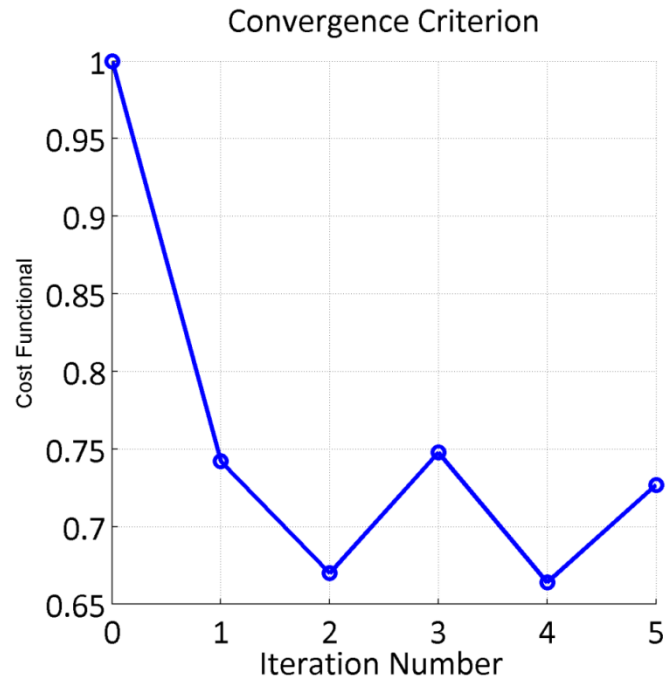


Figure 8.38: Cost functional vs. iteration

b. Optimization Starting from 500MHz Using Frequency-hopping

In order to avoid local minima, we decrease the first frequency to 500 MHz. From the figure 8.39 and 8.40, we can see that the antenna arrays cannot be optimized as the value of the cost functional increases significantly after 4 iterations, the lowest value of cost functional is around 0.72.

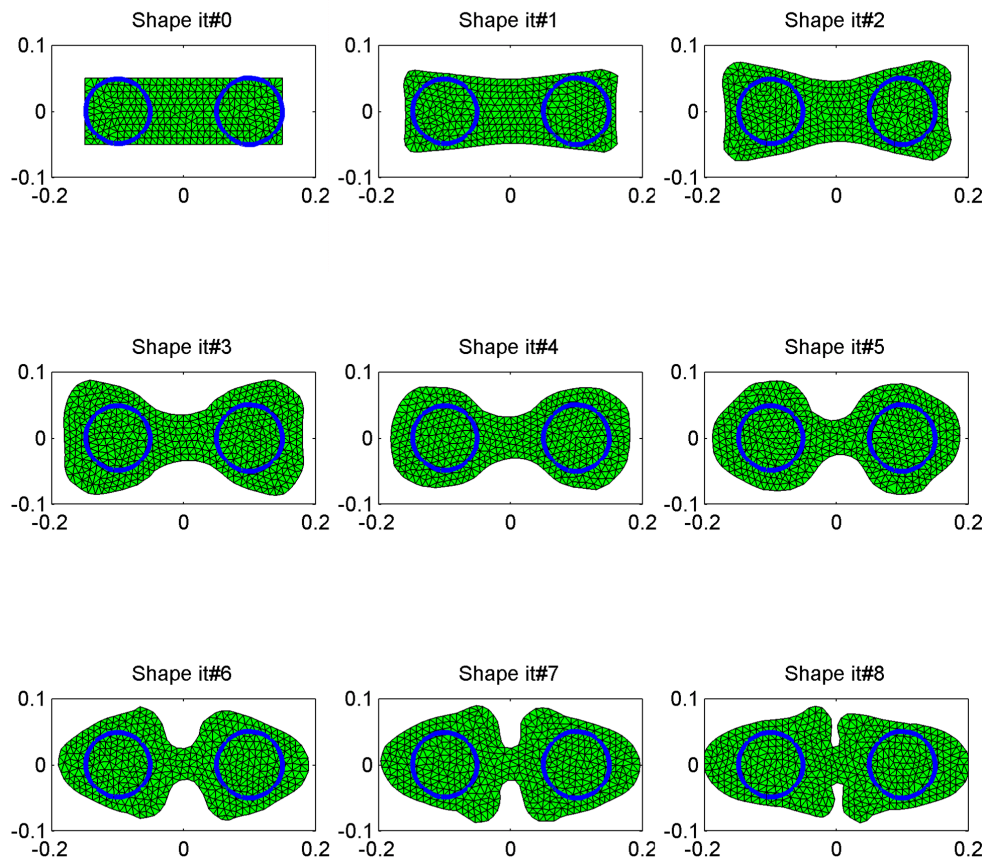


Figure 8.39: Shape evolution at 500 MHz

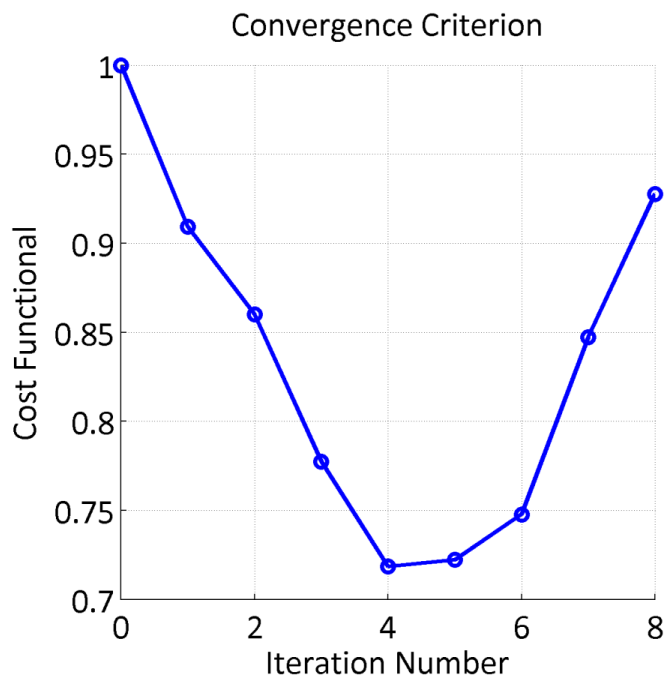


Figure 8.40: Cost functional vs. iteration

8.5.2 Shape Optimization using Multi-frequency Technique

Now, we use multi-frequency technique for the optimization strategy. Five working frequencies (shown in Table 8.6) and we use the same 3 incident dipoles as the previous study for the illumination.

Frequency #	Working frequency (GHz)
1	1.0
2	2.0
3	3.0
4	4.0
5	5.0

Table 8.6: Incident dipoles

a. Optimization with First Coefficients of Level Set

For the coefficients of the algorithm, the size of the level set pixels is 4 mm, the maximum of CFL coefficient α is 0.7, and the maximum number of evolutions is 3 at each iteration step. Therefore, the maximum distance for a point on the contour can move is 8.4 mm.

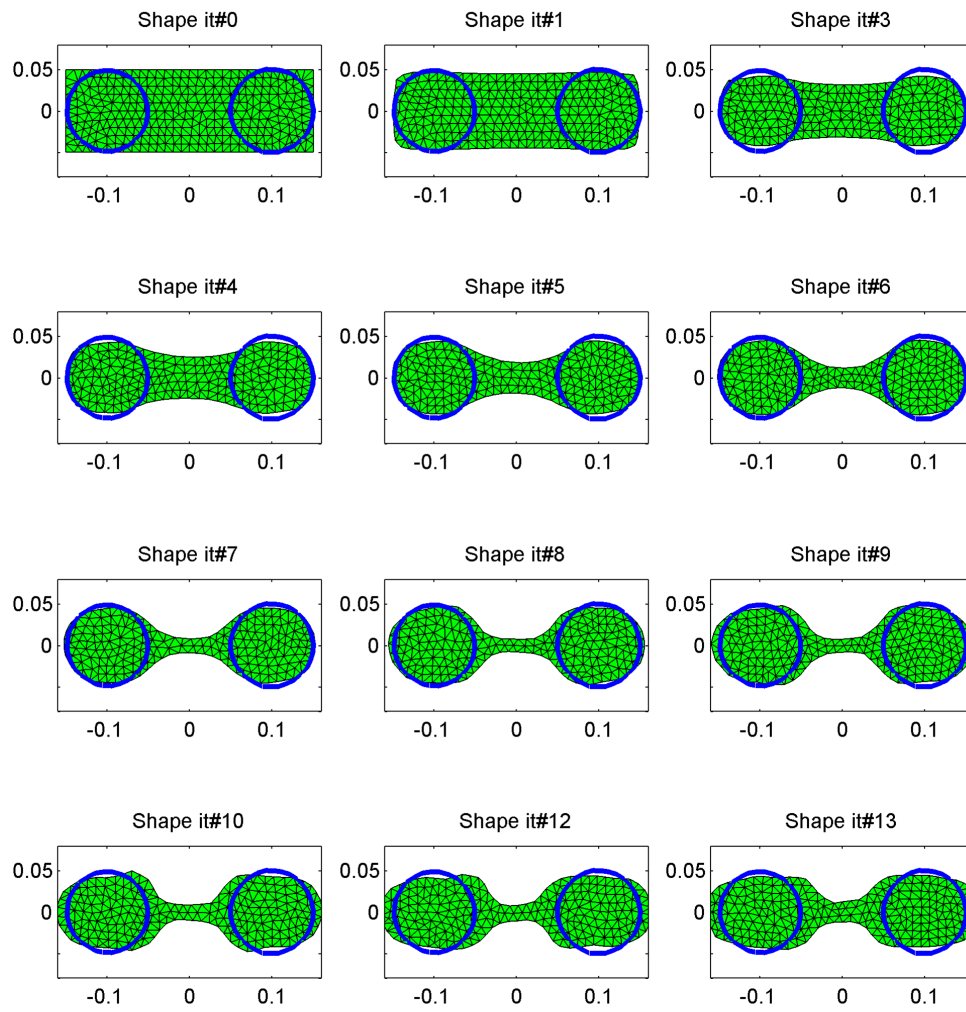


Figure 8.41: Shape evolution using multi-frequency technique

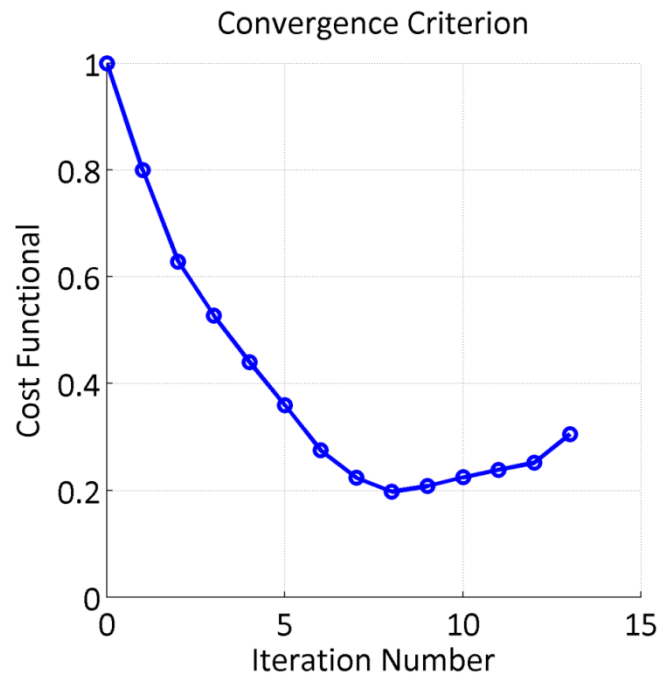


Figure 8.42: Cost functional vs. iteration

We can see from the Figures 8.41 and 8.42 that for these optimization coefficients, the criterion cannot converge. After the 8th iteration, the value of cost functional increases to higher values around 0.2.

b. Optimization with Second Coefficients of Level Set

Now, we keep the same coefficient for the strategy for the first 7 iterations. However, at the 8th iteration, we change the number of evolutions to 6, and the CFL coefficient α to 0.7. It means that the maximum of distance for a point on the contour can move is 16.8 mm. We can see the results from Figures 8.43 and 8.44 that the criterion converges finally after 15 iterations, and at 8th iteration, the antenna shape is splitted. At the 15th iteration, we can obtain the optimized shape.

Comparing with the last experiment we have done, the distance we move at the 8th iteration is an important factor, which can allows the optimization to go over a local minimum.

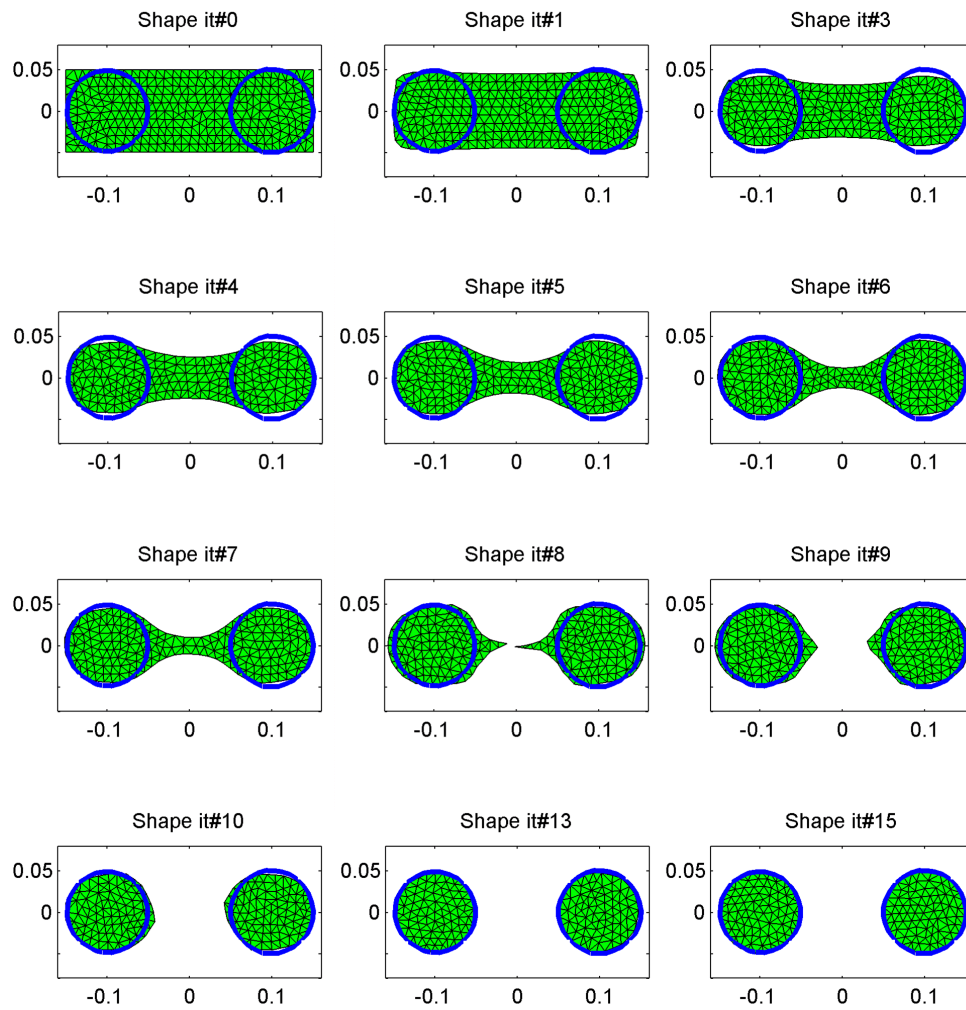


Figure 8.43: Shape evolution using multi-frequency technique

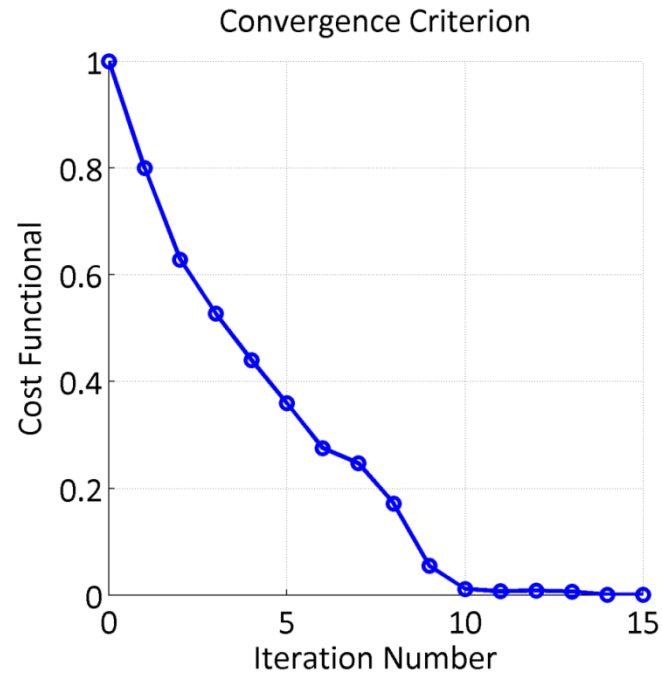


Figure 8.44: Cost functional vs. iteration

The results of convergence criterion illustrated in Figure 8.44 show that the criterion converges very fast. At the 15th iteration, the cost functional decreases to 0.41×10^{-3} .

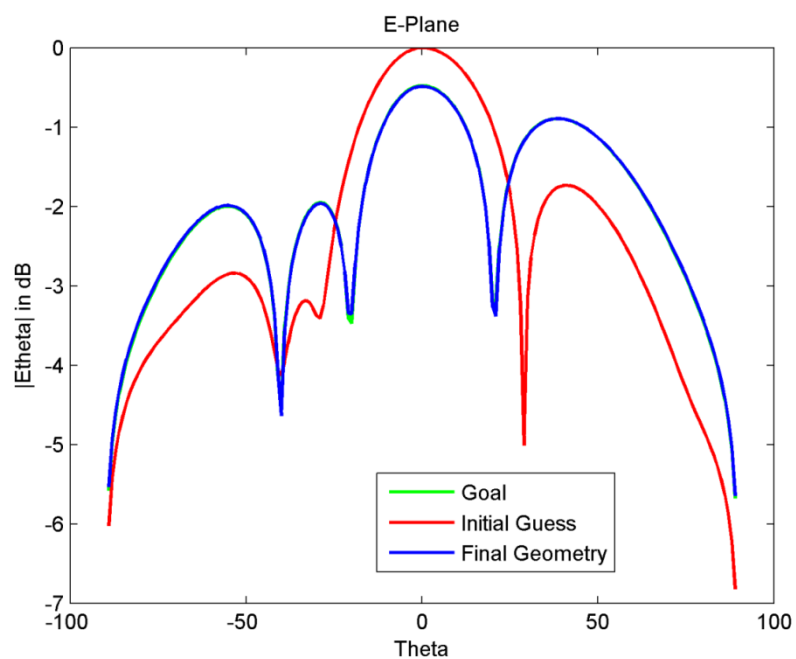


Figure 8.45a: Normalized radiation pattern of E-Plane

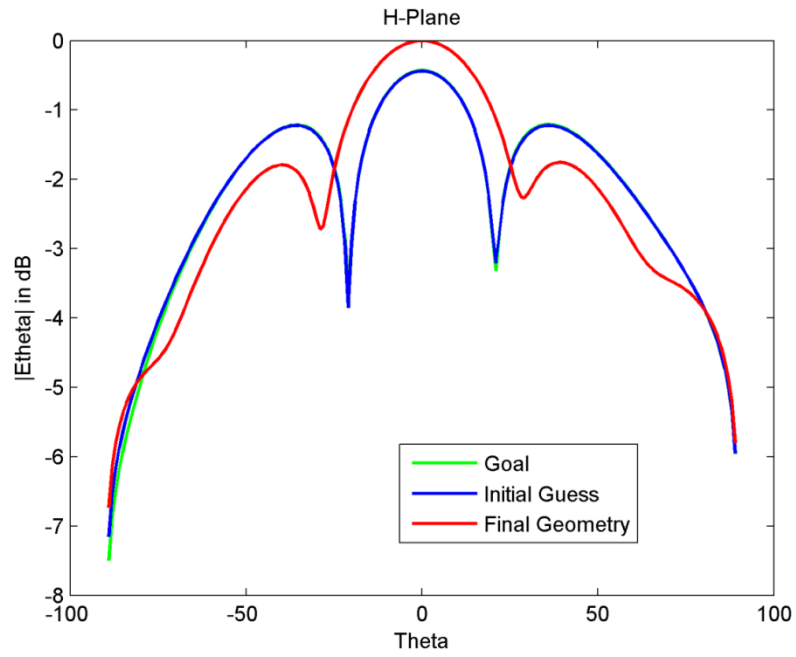


Figure 8.45b: Normalized radiation pattern of H-Plane

Figure 8.45 shows the scattered fields of the first incident dipole at 3 GHz radiated by the initial guess, final geometry and goal. After several iterations, the radiation pattern radiated by the goal can be found.

8.6 Shape Optimization of a Single U-shape Reflectarray Element Using Topological Gradient

In this study, we optimize a single U-shape reflectarray element shown in Figure 8.46 of about 10 cm outer diameter and 6 cm internal diameter. The shape gradient is computed by using the topological shape gradient method. We use different optimization techniques to implement the optimization procedure. The reflectarray element is illuminated by two incident dipoles working at different frequencies as shown in Table 8.7, and the scattered fields are measured in the far field.

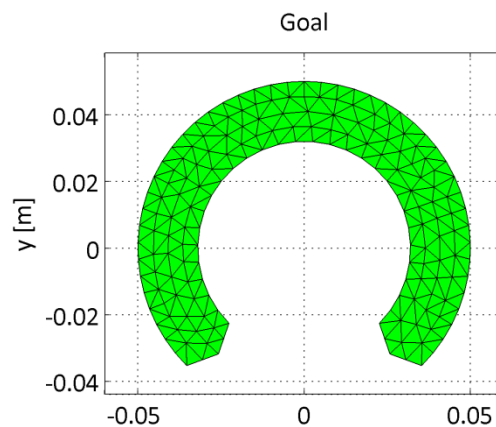


Figure 8.46: Goal

8.6.1 Optimization From an Initial Guess of a Larger Size Element

We first use the frequency-hopping technique for the optimization strategy. For each single frequency, we use 2 incident dipoles to illuminate independently.

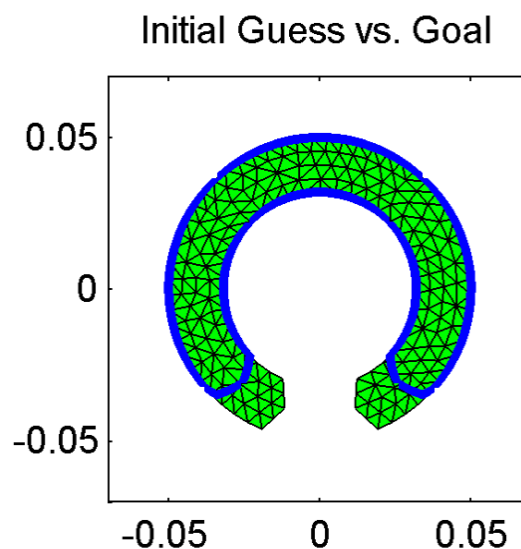


Figure 8.47: Initial Guess vs. Goal

Dipole N#	Dipole Moment	x [m]	y [m]	z [m]
1	(1,1,0)	0	0	10
2	(-1,1,0)	0	0	10

Table 8.7: Incident dipoles

We start from 3.5 GHz, and obtain an optimal shape at the 3rd iteration, and then we increase the frequency to 6 GHz, and finally obtain the result at the 6th iteration. In Figure 8.48, we can see that the size of the initial guess is decreased at each iteration step thanks to the optimization algorithm. The convergence criterion illustrated in Figure 8.49 shows that the value of the cost functional decreases to about 0.48.

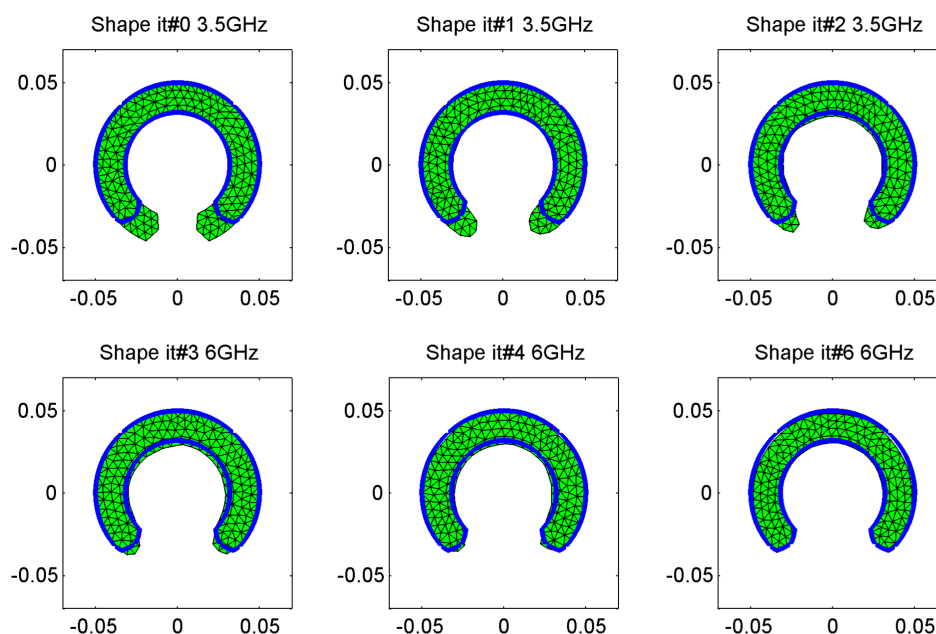


Figure 8.48: Shape evolution using frequency-hopping technique

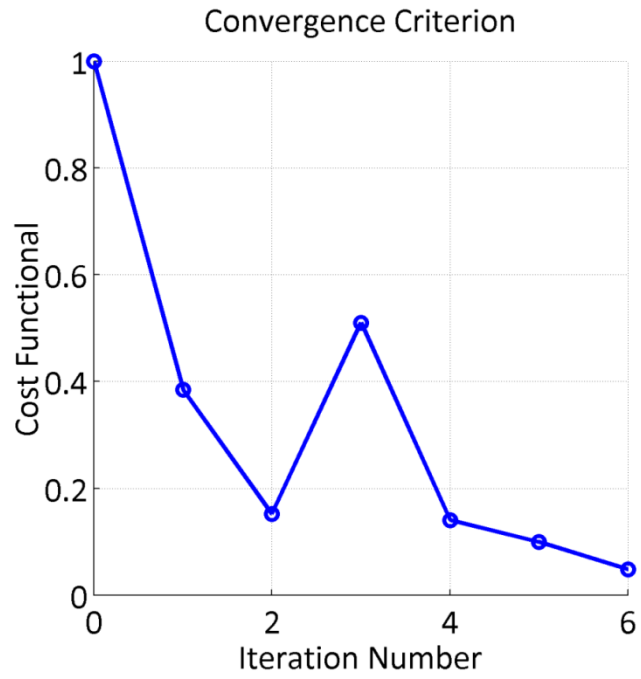


Figure 8.49: Cost functional vs. iteration

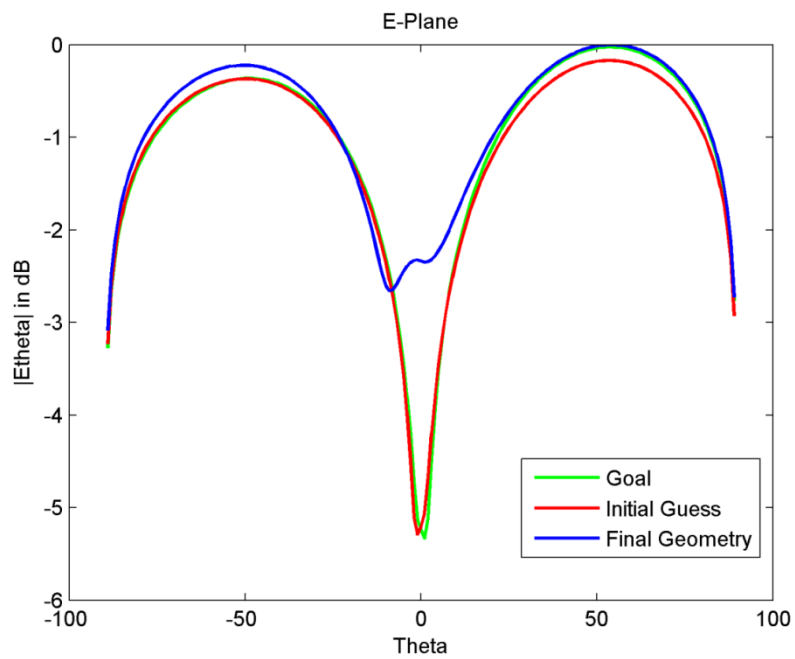


Figure 8.50a: Normalized radiation pattern of E-Plane at 3.5 GHz

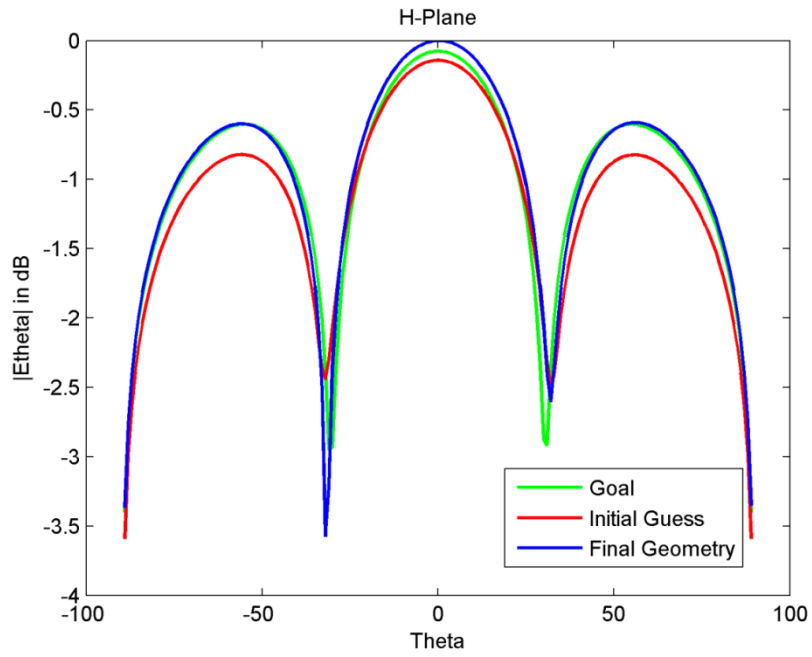


Figure 8.50b: Normalized radiation pattern of H-Plane at 3.5 GHz

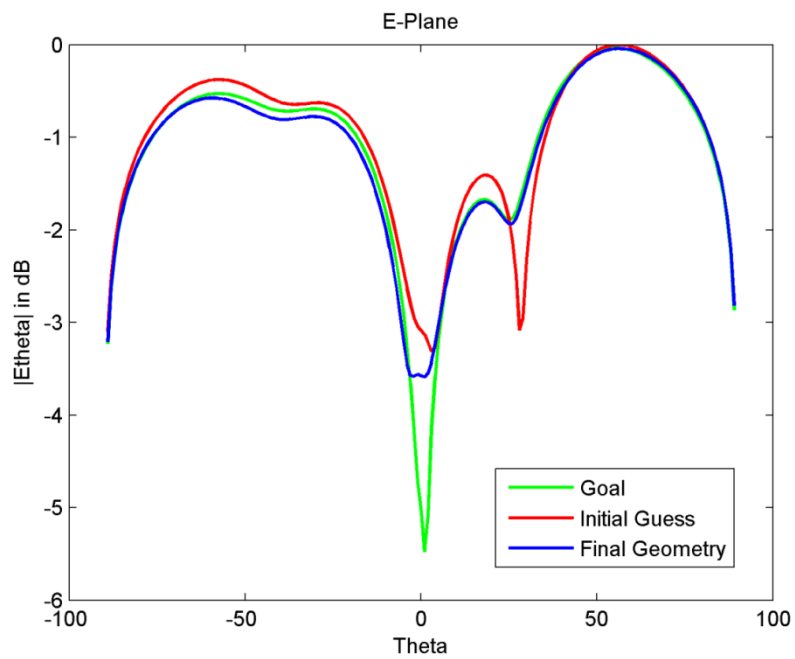


Figure 8.51a: Normalized radiation pattern of E-Plane at 6.0 GHz

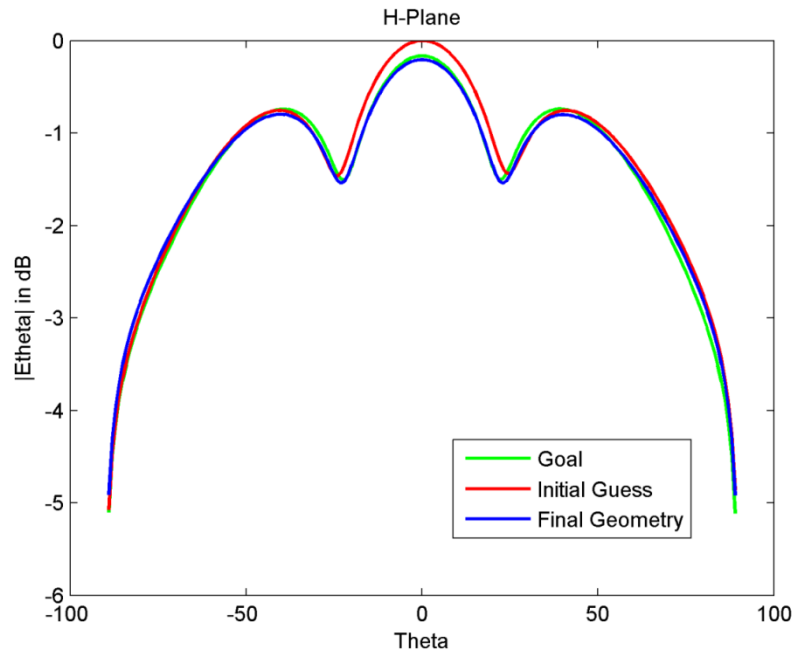


Figure 8.51b: Normalized radiation pattern of H-Plane at 6.0 GHz

Figure 8.50 and 8.51 show the scattered fields of the first incident dipole at 3.5 GHz and 6.0 GHz radiated by the initial guess, final geometry and goal. After several iterations, the radiation pattern radiated by the goal can be found finally.

8.6.2 Optimization From an Initial Guess of a Smaller Size Element

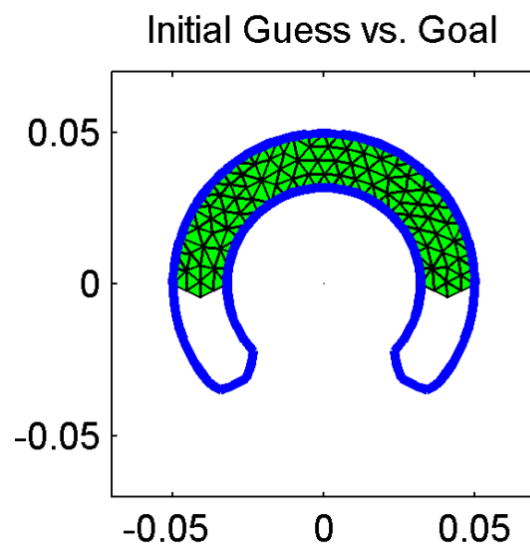


Figure 8.52: Initial Guess vs. Goal

a. Shape Optimization Using Frequency-Hopping Technique

Now, we keep the same coefficients of optimization procedure and frequency-hopping strategy as for the last experiment to optimize the antenna element. The starting frequency is 3.5 GHz. From Figures 8.53 and 8.54, we can find that the reflectarray element shape cannot be optimized, and the criterion cannot converge. At the 7th iteration, the smallest value of cost function is about 0.34, and after the value is increasing. It means that we need to change the optimization strategy with this initial shape.

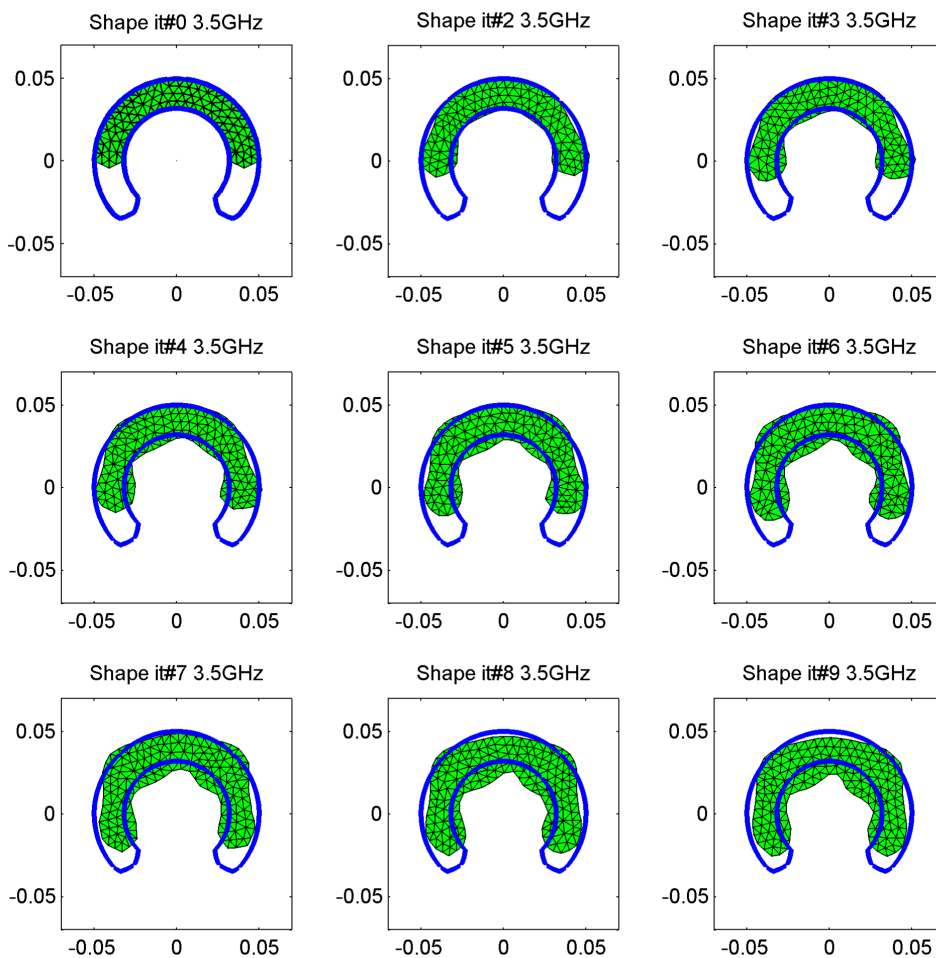


Figure 8.54: Shape evolution using frequency-hopping technique

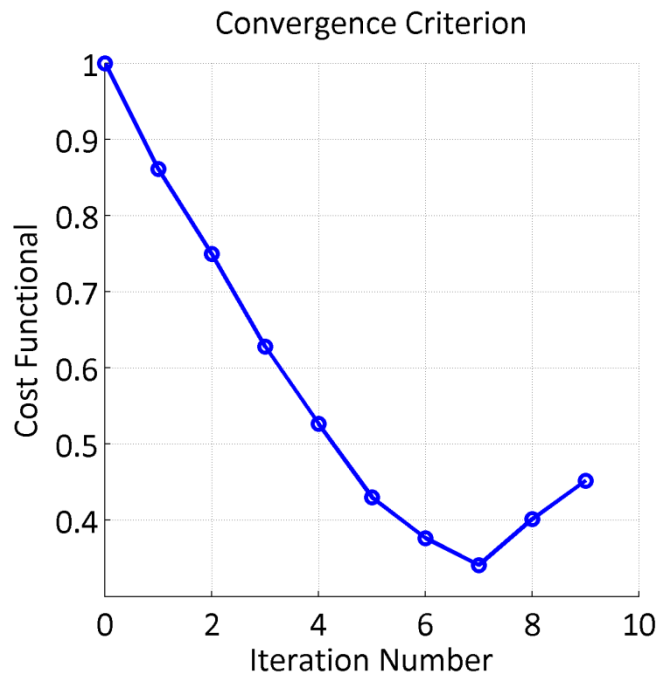


Figure 8.53: Cost functional vs. iteration

b. Shape Optimization Using Multi-Frequency Technique Without Velocity Limitation

Now, we use a multi-frequency technique for the optimization strategy. Three frequencies and four incident dipoles as shown in Table 8.8 and 8.9 are used for the simulation.

Dipole N#	Dipole Moment	x [m]	y [m]	z [m]
1	(1,1,0)	0	0	10
2	(-1,1,0)	0	0	10
3	(0,1,0)	0	0	10
4	(-1,1,0)	0	0	10

Table 8.8: Incident dipoles

Frequency #	Working Frequency (GHz)
1	3.5
2	4.8
3	6.0

Table 8.9: Working frequencies

Figures 8.55 and 8.56 show the velocity obtained by the topological gradient at 3.5 GHz, and with the multi-frequency, respectively. Comparing these two figures, we can find the difference at the topside part of the antenna element (indicated with a red line) that the velocity given by 3.5 GHz is stronger than with the multi-frequency, and we hope this velocity can be small enough for the optimization. It means that we obtain more information when using multi-frequency than with a single frequency and the local minimum shown in the figure 8.54 can be avoided.

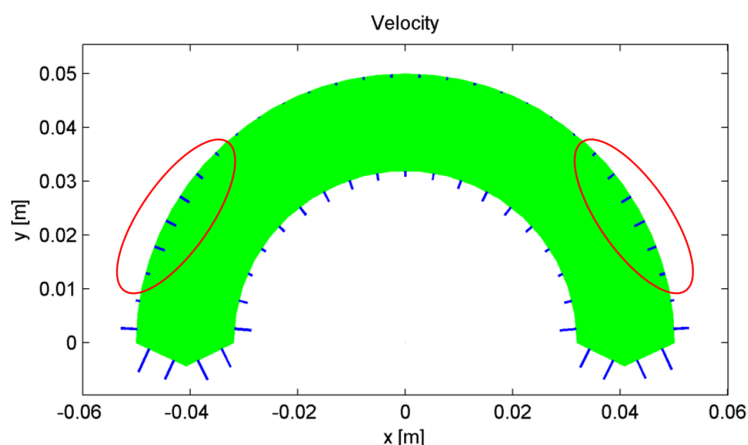


Figure 8.55: Velocity at 3.5 GHz

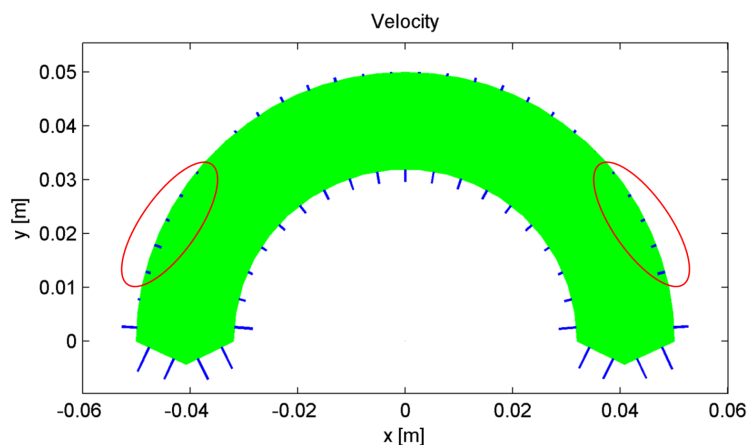


Figure 8.56: Velocity with multi-frequency

However, there are still some technical constraints for this example. The results illustrated in Figure 8.57 show that using a multi-frequency technique, after 11 iterations, we can obtain a better shape than using a frequency-hopping technique. However, from the final shape at the 11th iteration, we can see that the final geometry does not totally match with the goal, especially for the external part of the element. The Figure 8.56 for the convergence criterion also shows that it cannot converge at the final iteration. We need to find another solution.

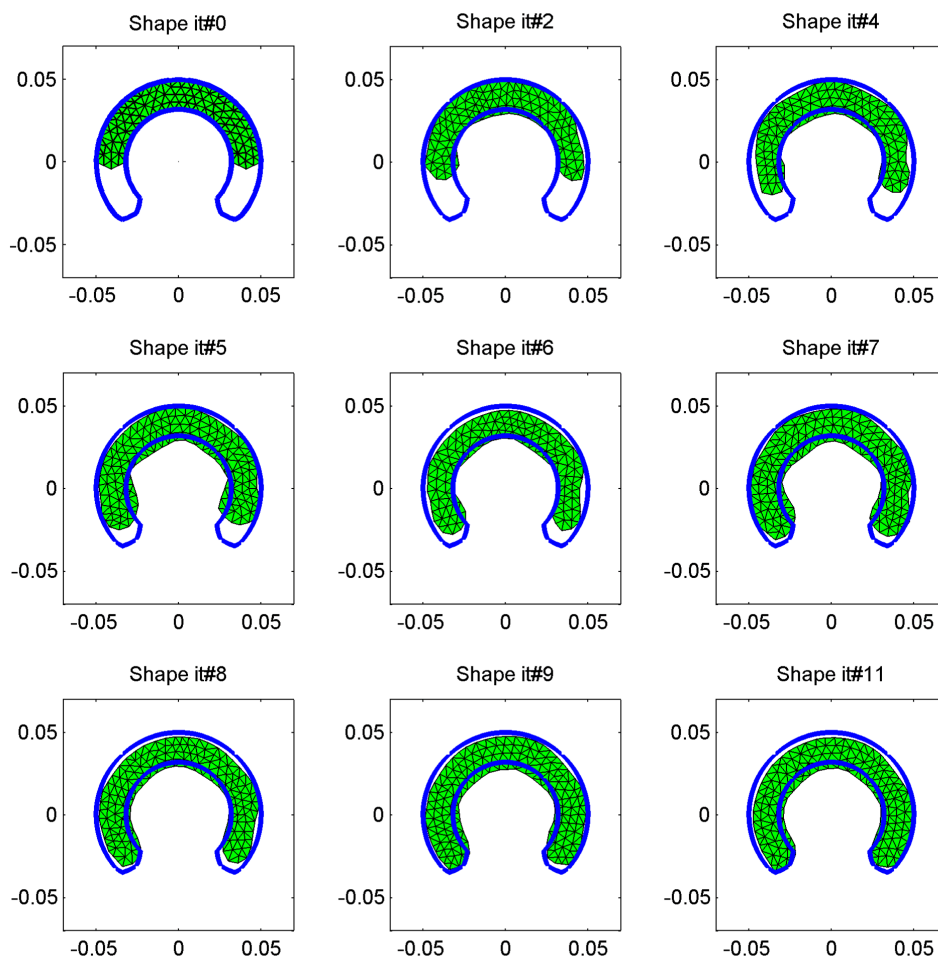


Figure 8.57: Shape evolution using multi-frequency technique

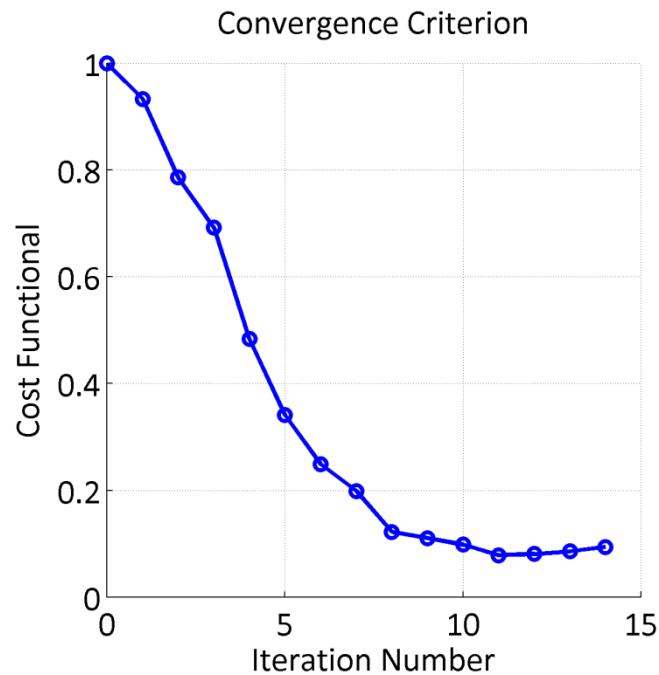


Figure 8.58: Cost functional vs. iteration

c. Shape Optimization Using Multi-Frequency Technique With Velocity Limitation

Now, we keep the same multi-frequency technique, but we need to find a better optimization technique for this problem. The main idea is that for the first several iterations, we will only evolve the antenna shape where we have the higher gradient values. At each iteration step, we have to find the highest gradient values, and then by comparing with this value, we determine the values to evolve. From the initial guess to the 2nd iteration, we only consider the values that are greater than 60% of the highest gradient, and for 3rd iteration to the 5th iteration, 40% of the highest gradient. From 6th iteration, we consider the entire shape gradients we have obtained.

From the Figure 8.59, we can find that by controlling the evolving velocity, we can achieve smoother and more regular shapes rather than keeping all the velocities. At 11th iteration, we can almost obtain an optimal shape compared to the goal geometry.

For the convergence criterion shown in Figure 8.60, we can see that the optimization procedure finally converges at the 11th iteration.

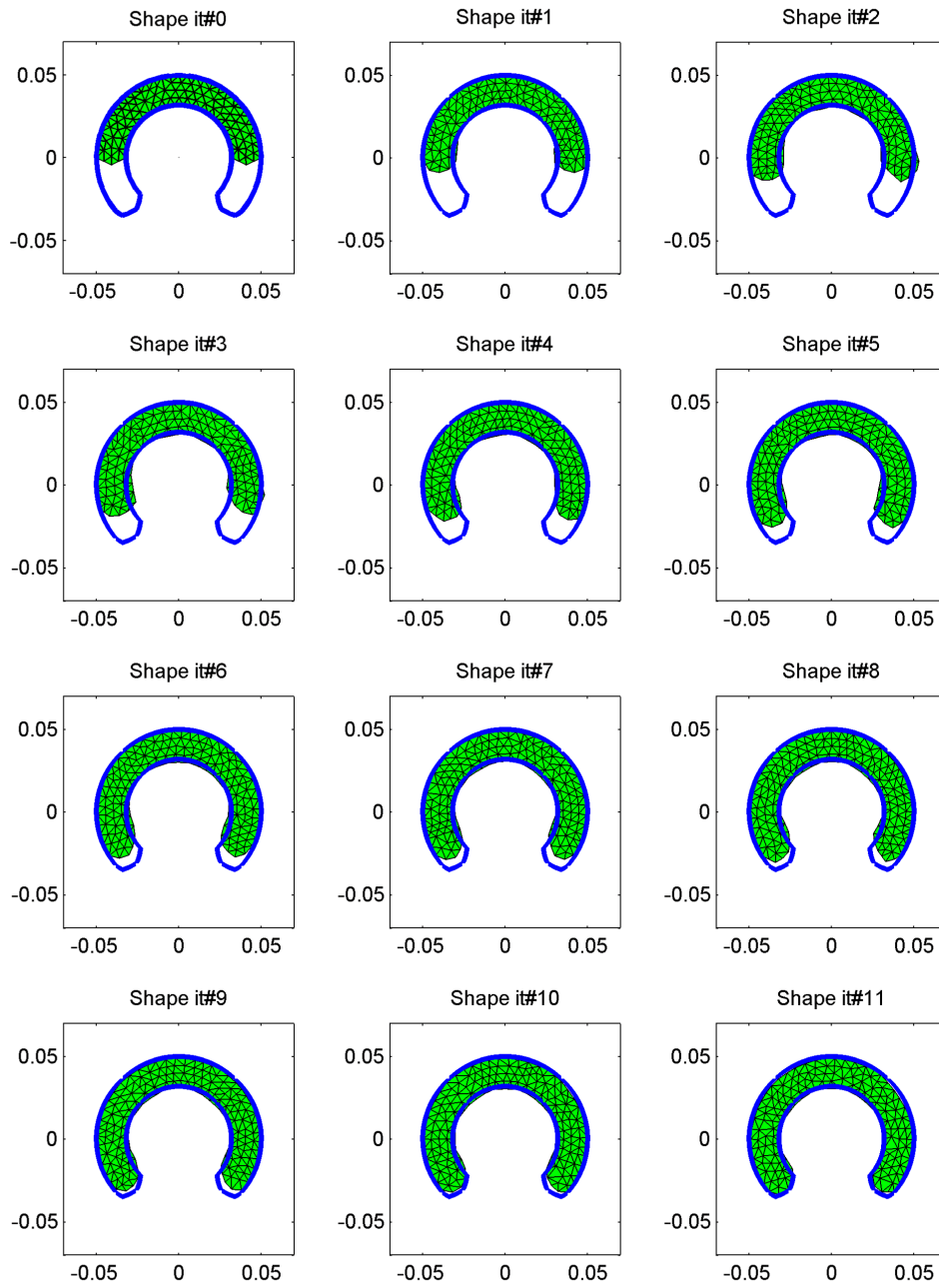


Figure 8.59: Shape evolution using multi-frequency technique

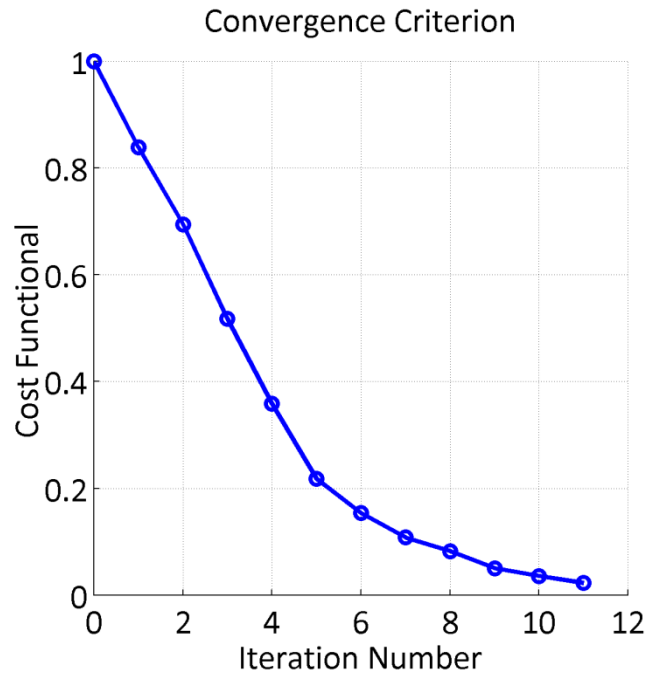


Figure 8.60: Cost functional vs. iteration

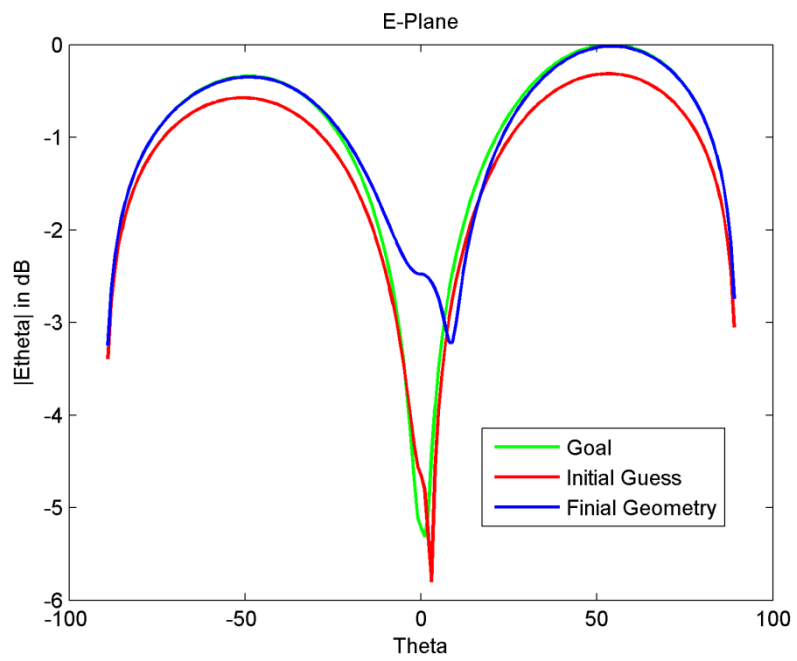


Figure 8.61a: Normalized radiation pattern of E-Plane at 3.5GHz

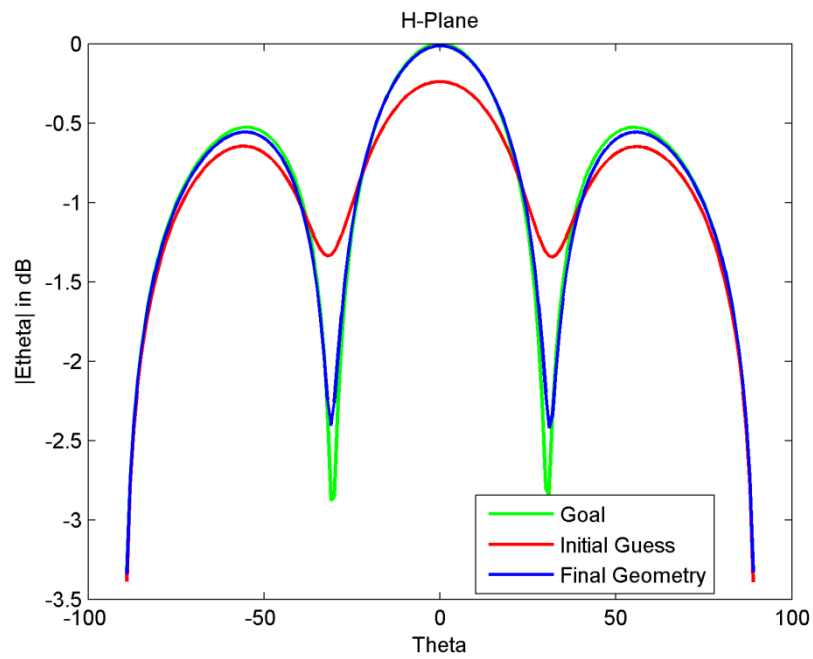


Figure 8.61b: Normalized radiation pattern of H-Plane at 3.5GHz

Figure 8.61 shows the scattered fields of the first incident dipole at 3.5 GHz radiated by the initial guess, final and goal geometry. We can see that after several iterations, the radiation pattern radiated by the goal can be found finally.

GENERAL CONCLUSION

In this work, an inverse scattering method based on an integral formulation of the electromagnetic problem has been proposed and developed. The aim of this work is to find the optimal shape of planar antennas and planar array elements from given or imposed radiation patterns.

As shown with the results in Chapter 8, we have successfully developed an efficient and accurate optimization algorithm. The optimization framework can be applied to general planar antennas and arrays.

The inversion shape optimization algorithm is based on a level set method. In order to obtain the velocity for the level set evolution, we have found the corresponding shape gradient (or shape deformation) versus radiation pattern modification taking into account the modeling of the antenna (for the finite element mesh). In this thesis, some new methods have been proposed and developed:

- First, an analytical shape gradient method has been proposed. The main idea focuses on the computation of the derivation of the coupling matrix and currents versus geometry. With this method, we have directly access to the sensitivity of the cost function versus parameters. Meanwhile, based on the derivation we have obtained, a conjugate gradient method for the optimizing the location of antenna array elements.

- Second, we have also developed a classic adjoint method to compute the shape gradient. This method mainly aims for computing the adjoint current on the antenna boundary, and can be used especially for 3D object optimization. However, the adjoint formula is not valid for 2D shape planar antennas or antenna arrays where the outward-pointing normal cannot be continuously defined everywhere. In Chapter 7, we have shown some demonstrations of constraints of the adjoint formula by comparing it with the discrete and analytical method for both 2D and 3D antenna shapes.

- Third, in order to compute the shape gradient efficiently, we have given a new sense to the shape gradient versus an edge deformation (or transformation) in 3D for metallic layers with limited surfaces. The shape gradient is computed by means of a topological deformation method, which is solved by adding a small triangular element to an edge on the contour, and obtaining a new flux, based on a linear system transformation. We can use this derived numerical model to study planar structures with the notion of metallic layer with a 2D outward normal direction. Moreover, a finite differential method based on nodal point mesh derivation with an infinitesimal modification of the triangular elements on the contour along the outward

normal direction has been proposed as a technical criterion, and we can still use it to optimize the shape of antennas as it is an accurate method.

Finally, a narrow band level set method has also been developed to implement the optimization algorithm. By using level set method and combining some shape gradient computation methods we discussed above, some demonstrations for the shape optimization of planar antennas have been carried out. Frequency hopping and multi-frequency techniques have been used to different antenna configurations for optimizing the shape within a frequency band. Different cases have been studied for investigating the performance of the inverse algorithm and optimization procedure.

Annex 1 - Spherical Coordinate System

A Cartesian coordinate system can be defined by an original point O and three orthogonal axes (Ox , Oy , Oz) as shown in Figure A1.1. The unit vectors of the axes are: $\hat{e}_x, \hat{e}_y, \hat{e}_z$. For example, a point M in the space can be represented by the three components of vector \vec{r} :

$$\vec{r}(x, y, z) = x\hat{e}_x + y\hat{e}_y + z\hat{e}_z \quad (\text{A1.1})$$

And M' is the projection of M on the plane xOy , and M'' is the projection of M on z axis.

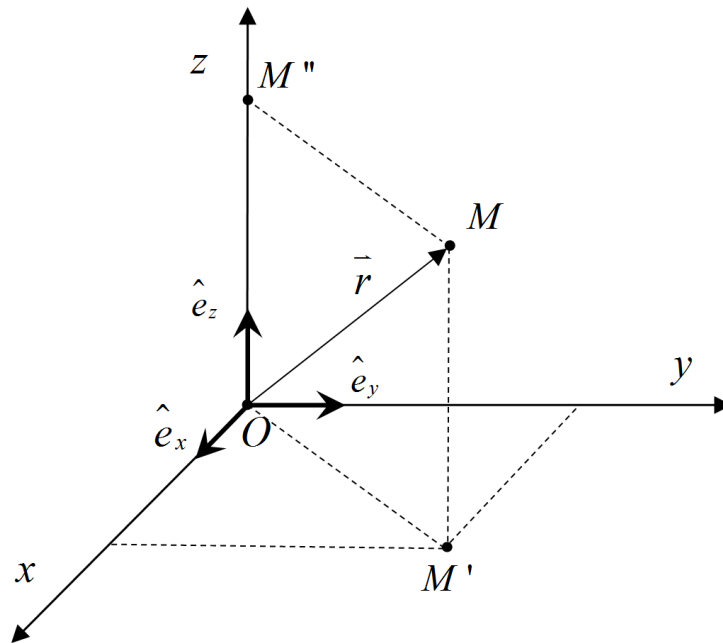


Figure A1.1 Cartesian coordinate system

In a spherical coordinates system, a point M in the space is considered as a point on a sphere that has a center as the original point O .

We can define also the Cartesian coordinate by using the spherical coordinate system:

$$\begin{aligned} x &= r \sin \theta \cos \phi \\ y &= r \sin \theta \sin \phi \\ z &= r \cos \theta \end{aligned} \quad (\text{A1.2})$$

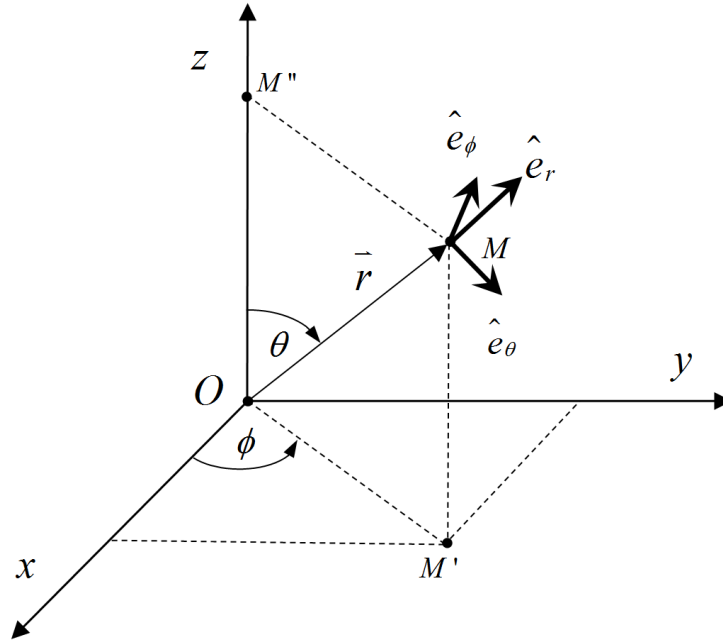


Figure A1.2 Spherical coordinate system

For a spherical system, a vector $\vec{E}(M)$ for a point $M(\vec{r})$ is represented by three components (E_r, E_θ, E_ϕ) , and can be written as:

$$\vec{E}(M) = E_r \hat{e}_r + E_\theta \hat{e}_\theta + E_\phi \hat{e}_\phi \quad (\text{A1.3})$$

The transformation from Cartesian coordinate system to spherical coordinate system can be written as:

$$\begin{pmatrix} \hat{e}_r \\ \hat{e}_\theta \\ \hat{e}_\phi \end{pmatrix} = \begin{pmatrix} \sin \theta \cos \phi & \sin \theta \sin \phi & \cos \theta \\ \cos \theta \cos \phi & \cos \theta \sin \phi & -\sin \theta \\ -\sin \phi & \cos \phi & 0 \end{pmatrix} \begin{pmatrix} \hat{e}_x \\ \hat{e}_y \\ \hat{e}_z \end{pmatrix} \quad (\text{A1.4})$$

For a scattering problem, let assume the polarization of the incident electric field is along y axis, and the antenna is located at the original point O in xOy plane. We can define the zOy plane ($\phi = 90^\circ$) as the E-plane, then we can simplify the transformation as:

$$\begin{pmatrix} \hat{e}_r \\ \hat{e}_\theta \\ \hat{e}_\phi \end{pmatrix} = \begin{pmatrix} 0 & \sin\theta & \cos\theta \\ 0 & \cos\theta & -\sin\theta \\ -1 & 0 & 0 \end{pmatrix} \begin{pmatrix} \hat{e}_x \\ \hat{e}_y \\ \hat{e}_z \end{pmatrix} \quad (\text{A1.5})$$

If the zOx plane ($\phi = 0^\circ$) is the H-Plane, the transformation system can be defined as:

$$\begin{pmatrix} \hat{e}_r \\ \hat{e}_\theta \\ \hat{e}_\phi \end{pmatrix} = \begin{pmatrix} \sin\theta & 0 & \cos\theta \\ \cos\theta & 0 & -\sin\theta \\ 0 & 1 & 0 \end{pmatrix} \begin{pmatrix} \hat{e}_x \\ \hat{e}_y \\ \hat{e}_z \end{pmatrix} \quad (\text{A1.6})$$

Annex 2 - Calculation of Scattering Field

Let S be an aperture (in Figure A2.1), illuminated by a plane wave such as:

$$\begin{aligned}\bar{E}_i &= |\bar{E}_i| \cdot \bar{e}_x \\ \bar{H}_i &= |\bar{H}_i| \cdot \bar{e}_y \\ |\bar{E}_i| &= \eta |\bar{H}_i| \\ \eta &= 120\pi\end{aligned}\tag{A2.1}$$

We want to calculate the field at point M radiated by S , with $r = |\overline{OM}|$ the distance from the original point to the measured point.

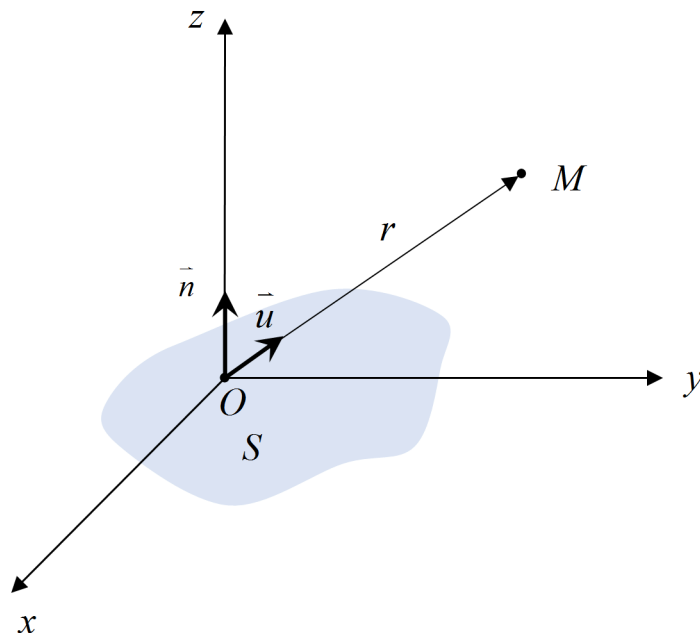


Figure A2.1 Radiating aperture

Let assume as shown in Figure A2.2, that we have an electric current \bar{J} inside a volume V ,

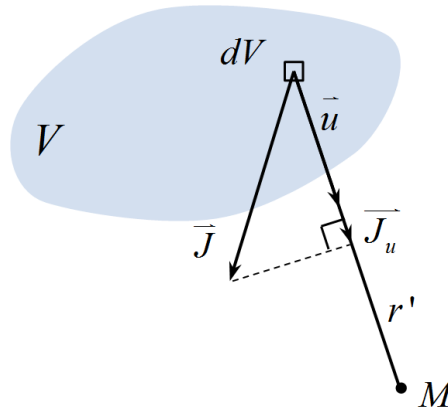


Figure A2.2 Radiation of a current J inside a volume V

Then, we can write the scattered field at the point M as:

$$\begin{aligned}\bar{E} &= \frac{1}{4\pi j\epsilon\mu} \int_V \left[(3 + 3jkr' - k^2 r'^2) \cdot \bar{J}_u - (1 + jkr' - k^2 r'^2) \cdot \bar{J} \right] \frac{e^{-jkr'}}{r'^3} dV \\ \bar{H} &= \frac{1}{4\pi} \int_V \left[(1 + jkr') \cdot (\bar{J} \wedge \bar{u}) \frac{e^{-jkr'}}{r'^2} \right] dV\end{aligned}\quad (\text{A2.2})$$

In the far-field region, and by considering:

$$\frac{k^2}{\omega\epsilon} = k\eta, \quad (\bar{J} \wedge \bar{u}) \wedge \bar{u} = \bar{J}_u - \bar{J}\quad (\text{A2.3})$$

The formula A2.2 can be written as:

$$\begin{aligned}\bar{E} &= \frac{jk}{4\pi} \eta \int_V \left[(\bar{J} \wedge \bar{u}) \wedge \bar{u} \right] \frac{e^{-jkr'}}{r'} dV \\ \bar{H} &= \frac{jk}{4\pi} \int_V (\bar{J} \wedge \bar{u}) \frac{e^{-jkr'}}{r'} dV\end{aligned}\quad (\text{A2.4})$$

We can simplify again the formula A2.4 by choosing an original point O in the antenna region as shown in Figure A2.3.

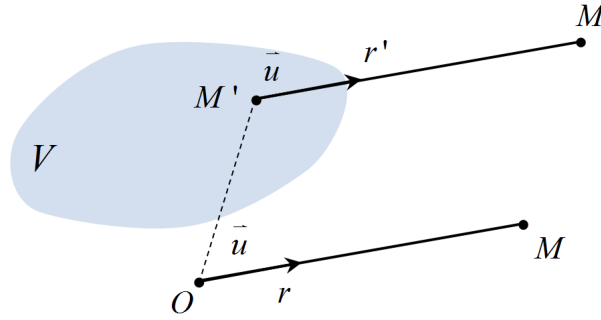


Figure A2.3 Modified scattering system

M' is a point in the volume V . We have the relationship of vector:

$$\begin{aligned} r' &= r - \vec{u} \cdot \overline{OM'} \\ \frac{e^{-jkr'}}{r'} &\approx \frac{e^{-jkr}}{r} e^{jk(\vec{u} \cdot \overline{OM'})} \end{aligned} \quad (\text{A2.5})$$

Then we can write the formula A2.4 as:

$$\begin{aligned} \bar{E} &= 30jk \frac{e^{-jkr}}{r} \int_V \left[(\bar{J} \wedge \vec{u}) \wedge \vec{u} \right] e^{jk(\vec{u} \cdot \overline{OM'})} dV \\ \bar{H} &= 30jk \frac{e^{-jkr}}{r} \int_V \frac{(\bar{J} \wedge \vec{u})}{\eta} e^{jk(\vec{u} \cdot \overline{OM'})} dV \end{aligned} \quad (\text{A2.6})$$

In order to obtain a general formula, by considering the magnetic currents, we can write the formula as:

$$\begin{aligned} \bar{E} &= 30jk \frac{e^{-jkr}}{r} \int_V \left[(\bar{J} \wedge \vec{u}) \wedge \vec{u} - \frac{\bar{M} \wedge \vec{u}}{\eta} \right] e^{jk(\vec{u} \cdot \overline{OM'})} dV \\ \bar{H} &= 30jk \frac{e^{-jkr}}{r} \int_V \left[\frac{\bar{J} \wedge \vec{u}}{\eta} + (\bar{M} \wedge \vec{u}) \wedge \vec{u} \right] e^{jk(\vec{u} \cdot \overline{OM'})} dV \end{aligned} \quad (\text{A2.7})$$

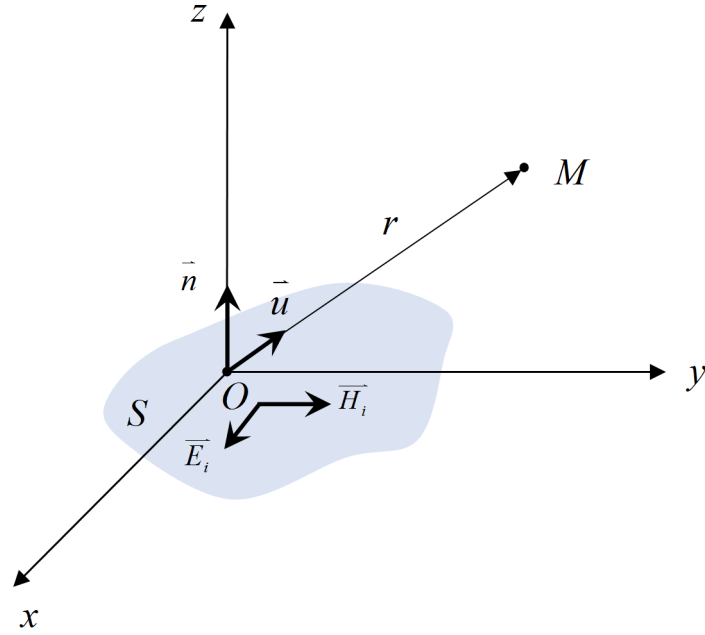


Figure A2.4 Scattering system and incident fields

By using the Kirchhoff approximation and Huygens principle, we have:

$$\begin{aligned}\bar{J} &= -\bar{H}_i \wedge \bar{n} \\ \bar{M} &= \bar{E}_i \wedge \bar{n}\end{aligned}\quad (\text{A2.8})$$

Then we obtain:

$$\begin{aligned}\bar{J} &= -H_i \bar{e}_y \wedge \bar{n} = -H_i \bar{e}_x \\ \bar{M} &= \eta H_i \bar{e}_x \wedge \bar{n} = -\eta H_i \bar{e}_y\end{aligned}\quad (\text{A2.9})$$

where $H_i = |\bar{H}_i|$

We can write the scattered electric field as:

$$\bar{E} = 30jk \frac{e^{-jkr}}{r} H_i \int_S (\bar{e}_y - \bar{e}_x \wedge \bar{u}) e^{jk(\bar{u} \cdot \bar{OM})} dx' dy' \quad (\text{A2.10})$$

If we use spherical coordinate system, we have:

$$\bar{E} = 30jk \frac{e^{-jkr}}{r} H_i (1 + \cos\theta) (\cos\phi \bar{e}_\theta - \sin\phi \bar{e}_\phi) \int_S e^{jk(\bar{u} \cdot \bar{OM})} dx' dy' \quad (\text{A2.11})$$

Now, we consider a scattering system radiated by a rectangular planar antenna, as shown in Figure A2.5

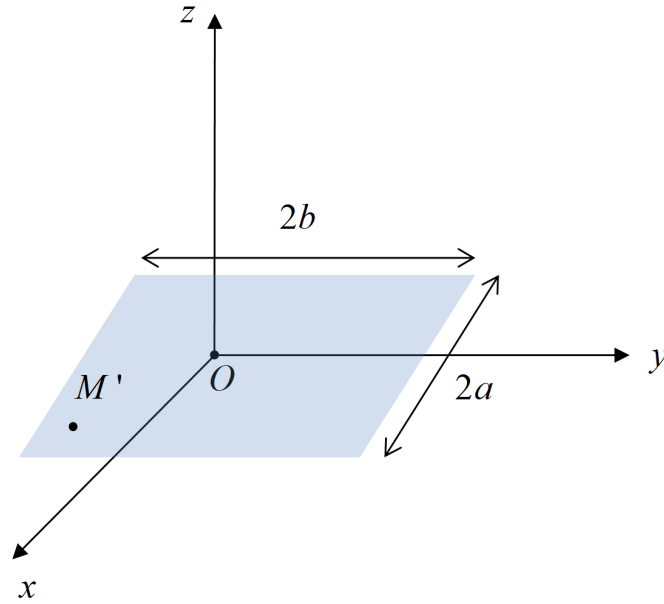


Figure A2.5 Scattering system of a rectangular antenna

We can write the kernel expression of formula A2.11 as:

$$\begin{aligned}
 \int_S e^{jk(\vec{r}-\vec{OM}')} dx' dy' &= \int_{x=-a}^{x=+a} \int_{y=-b}^{y=+b} e^{jk\vec{u}(x'\vec{e}_x+y'\vec{e}_y)} dx' dy' \\
 &= \int_{x=-a}^{x=+a} e^{jkx'\sin\theta\cos\phi} dx' \int_{y=-b}^{y=+b} e^{jky'\sin\theta\sin\phi} dx' dy' \quad (A2.12) \\
 &= 4ab \frac{\sin(ka\sin\theta\cos\phi)}{ka\sin\theta\cos\phi} \cdot \frac{\sin(ka\sin\theta\sin\phi)}{ka\sin\theta\sin\phi}
 \end{aligned}$$

$$\text{with: } \sin\theta\cos\phi = \frac{x}{r} \quad \sin\theta\sin\phi = \frac{y}{r}$$

For a typical circular antenna, we need to consider the scattering system, as shown in Figure A2.6

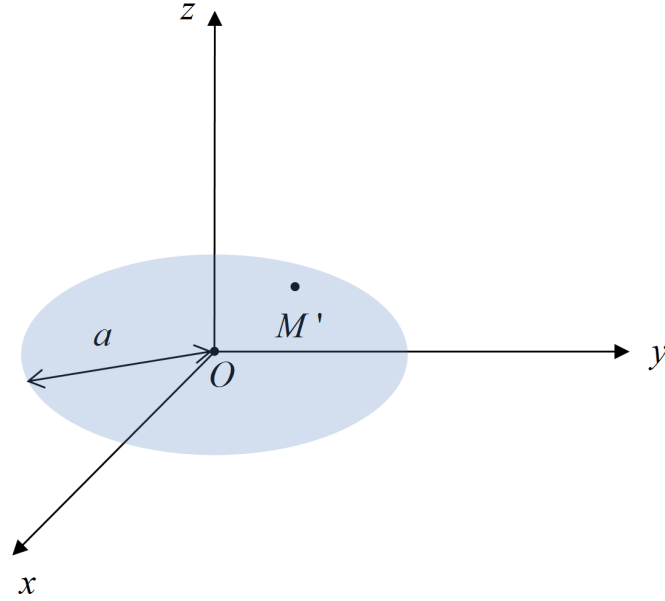


Figure A2.6 Scattering system of a circular antenna

Let:

$$\begin{aligned} x_{M'} &= r' \cos \phi' \\ y_{M'} &= r' \sin \phi' \end{aligned} \quad (\text{A2.13})$$

Then we have:

$$\begin{aligned} \vec{u} \cdot \overline{OM'} &= \sin \theta \cos \phi r' \cos \phi' + \sin \theta \sin \phi r' \sin \phi' \\ &= r' \sin \theta (\cos \phi \cos \phi' + \sin \phi \sin \phi') \end{aligned} \quad (\text{A2.14})$$

The kernel expression of formula A2.11 can be obtained as:

$$\int_S e^{jk(\vec{u} \cdot \overline{OM'})} dS' = \int_{\phi'=0}^{2\pi} \int_{r'=0}^a e^{jk r' \sin \theta \cos(\phi-\phi')} d\phi' r' dr' \quad (\text{A2.15})$$

We can define:

$$J_0(z) = \frac{1}{2\pi} \int_0^{2\pi} e^{jz \cos \phi} d\phi \quad (\text{A2.16})$$

Then we get the final expression:

$$\int_S e^{jk(\vec{u} \cdot \overline{OM'})} dS' = \int_0^a 2\pi J_0(kr' \sin \theta) r' dr' = 2\pi a^2 \frac{J_1(ka \sin \theta)}{ka \sin \theta} \quad (\text{A2.17})$$

Annex 3 - Signal-to-noise ratio for Robustness test

The signal-to-noise ratio is a measure used in science and engineering that compares the level of a desired signal to the level of background noise. It is defined as the ratio of signal power to the noise power:

$$SNR = 10 \log_{10} \frac{P_s}{P_n} \quad (A3.1)$$

P_s and P_n are the power of signal and noise respectively.

The signal power can be defined as:

$$P_s = \lim_{T \rightarrow 0} \frac{1}{2T} \int_{-T}^{+T} [s(t)]^2 dt \quad (A3.2)$$

For a sinusoidal signal we can write it as:

$$s(t) = S \cos(\omega_0 t + \phi) = S \cos \phi \cos \omega_0 t - S \sin \phi \sin \omega_0 t \quad (A3.3)$$

We can represent the noise by:

$$\begin{aligned} n(t) &= N(t) \cos(\omega_0 t + \phi + \varphi(t)) \\ &= N(t) \cos(\phi + \varphi(t)) \cos(\omega_0 t) - N(t) \sin(\phi + \varphi(t)) \sin(\omega_0 t) \end{aligned} \quad (A3.4)$$

If we write it in an exponential form, we have:

$$\begin{aligned} N_c &= N(t) e^{j(\phi + \varphi(t))} \\ &= N(t) \cos(\phi + \varphi(t)) + jN(t) \sin(\phi + \varphi(t)) \end{aligned} \quad (A3.5)$$

And we obtain:

$$\begin{aligned} r(t) &= \text{Re}[N_c] = N(t) \cos(\phi + \varphi(t)) \\ i(t) &= \text{Im}[N_c] = N(t) \sin(\phi + \varphi(t)) \end{aligned} \quad (A3.6)$$

(A3.

We have:

(A3.

$$n(t) = r(t) \cos \omega_0 t - i(t) \sin \omega_0 t \quad (\text{A3.7})$$

Then the power of the noise can be represented by:

$$P_n = \lim_{T \rightarrow \infty} \frac{1}{2T} \int_{-T}^{+T} [n(t)]^2 dt = \langle n^2(t) \rangle \quad (\text{A3.8})$$

$n(t)$ is a random signal in time domain, we can also consider it as a density function for a fixed time. If the process is ergodic, then the average of the signal in time domain will be the statistical average, and the process will be stationary.

$$\begin{aligned} P_n &= \langle n^2(t) \rangle = E[n^2(t)] \\ &= \int_{-\infty}^{+\infty} \int_{-\infty}^{+\infty} (r(t) \cos \omega_0 t - i(t) \sin \omega_0 t)^2 f_{ri} dr di \\ &= \int_{-\infty}^{+\infty} \int_{-\infty}^{+\infty} (r^2 \cos^2 \omega_0 t - 2ri \cos \omega_0 t \sin \omega_0 t + i^2 \sin^2 \omega_0 t) f_{ri} dr di \end{aligned} \quad (\text{A3.9})$$

Suppose r and i are independent:

$$f_{ri} = f_r \cdot f_i \quad (\text{A3.10})$$

Then we have:

$$\begin{aligned} P_n &= \cos^2 \omega_0 t \int_{-\infty}^{+\infty} r^2 f_r dr + \sin^2 \omega_0 t \int_{-\infty}^{+\infty} i^2 f_i di \\ &= -2 \cos \omega_0 t \sin \omega_0 t \int_{-\infty}^{+\infty} r f_r dr \cdot \int_{-\infty}^{+\infty} i f_i di \end{aligned} \quad (\text{A3.11})$$

We suppose:

$$f_r = f_i \quad (\text{A3.12})$$

Then the formula in A3.11 can be written as:

$$P_n = \int_{-\infty}^{+\infty} r^2 f_r dr - \sin 2\omega_0 t \left[\int_{-\infty}^{+\infty} i f_i di \right]^2 \quad (\text{A3.13})$$

The statistical average of $n(t)$ is given by:

$$\begin{aligned} E[n(t)] &= \int_{-\infty}^{+\infty} \int_{-\infty}^{+\infty} (r \cos \omega_0 t - i \sin \omega_0 t) f_r f_i dr di \\ &= (\cos \omega_0 t - i \sin \omega_0 t) \int_{-\infty}^{+\infty} r f_r dr \end{aligned} \quad (\text{A3.14})$$

And we have,

$$E[n(t)] = 0 \text{ if } E[r] = \int_{-\infty}^{+\infty} r f_r dr = 0 = E[i] \quad (\text{A3.15})$$

Then the variance of the noise can be written as:

$$P_n = \int_{-\infty}^{+\infty} r^2 f_r dr = \sigma_r^2 = \sigma_i^2 \quad (\text{A3.16})$$

The signal-to-noise ratio is given by:

$$SNR = 10 \log_{10} \frac{|S_c|^2}{2\sigma_r^2} \quad (\text{A3.17})$$

BIBLIOGRAPHY

-
- [1] G. Allaire, F. Jouve, and A.-M. Toader, "A level-set method for shape optimization," *C. R. Acad. Sci. Paris Ser. I Math.*, vol. 334, no. 12, pp. 1125–1130, 2002.
- [2] R. Ferrayé, J.Y. Dauvignac, and Ch. Pichot, "An inverse scattering method based on contour deformations by means of a level set method using frequency hopping technique". *IEEE Trans. Antennas Propag.*, Vol. 51, No. 5, pp. 1100-1113, May 2003.
- [3] S. Zhou, W. Li, and Q. Li, "Level-set based topology optimization for electromagnetic dipole antenna design", *J. Comput. Physics*, 229 (19), pp. 6915-6930, 2010.
- [4] J. Kataja, S. Järvenpää, J. Toivanen, R. Mäkinen, and P. Ylä-Oijala, "Shape sensitivity analysis and gradient-based optimization of large structures using MLFMA", *IEEE Trans. Antennas Propag.*, vol. 62, no. 11, pp. 5610-5618, Nov. 2014.
- [5] Y. Zhang, N.K. Nikolova, M.K. Meshram, "Design Optimization of Planar Structures Using Self-Adjoint Sensitivity Analysis", *IEEE Trans. Antennas Propag.*, vol. 60, no. 6, pp. 3060 -3066, June 2012
- [6] J.I., Toivanen, R.A.E. Mäkinen, J. Rahola, S. Järvenpää, P. Ylä-Oijala, "Gradient-based shape optimisation of ultra-wideband antennas parameterized using splines", *Microwaves, Antennas & Propagation, IET* , vol. 4, no. 9, pp. 1406 - 1414, Sep. 2010
- [7] N.K. Nikolova, R. Safian, E.A. Soliman, M.H. Bakr, J.W. Bandler, "Accelerated gradient based optimization using adjoint sensitivities" , *IEEE Trans. Antennas Propag.*, vol. 52, no. 8, pp. 2147 - 2157, Aug. 2014
- [8] M. El-Shenawee, O. Dorn, M. Moscoso, "An Adjoint-Field Technique for Shape Reconstruction of 3-D Penetrable Object Immersed in Lossy Medium", *IEEE Trans. Antennas Propag.*, vol. 57, no. 2, pp. 2147 - 2157, Feb. 2009
- [9] Y. Rahmat-Samii, E. Michielssen, *Electromagnetic optimization by genetic algorithms*, Wiley, 1999.
- [10] D. Marcano, "Synthesis of antenna arrays using genetic algorithms", *IEEE Trans. Ant. Propagat.*, Vol. 42, pp. 12-20, 2000.

- [11] M. Ohira, H. Ban, M. Ueba, "Evolutionary generation of subwavelength planar element loaded monopole antenna", *IEEE Ant. Wirel. Propagat. Lett.*, Vol. 10, pp. 1559-1562, 2011.
- [12] R. Ouedraogo, E. Rothwell, A. Diaz, S-Y Chen, A. Temme, K. Fuchi, "In-Situ optimization of metamaterial-inspired loop antennas", *IEEE Ant. Wirel. Propagat. Lett.*, Vol. 9, pp. 75-78, 2010.
- [13] F. Namin, T. Spence, D. Werner, E. Semouchkina, "Broadband, miniaturized stacked-patch antennas for L-band operation based on magneto-dielectric substrates", *IEEE Trans. Ant. Propagat.*, Vol. 58, N°9, pp. 2817–2822, September 2010.
- [14] Z. Bayraktar, D. Werner, P. Werner, "Miniature meander-line dipole antenna, designed via an orthogonal-array-initialized hybrid particle-swarm optimizer", *IEEE Ant. Propagat. Mag.*, Vol. 53, N°3, pp. 42-59, June 2011.
- [15] M. Shahpari, D. Thiel, A. Lewis, "An investigation into the Gustafsson limit for small planar antennas using optimization", *IEEE Trans. Ant. Propagat.*, Vol. 62, N°2, pp. 950–955, February 2014.
- [16] S. Karimkashi, A. Kishk, "Invasive weed optimization and its features in electromagnetics", *IEEE Trans. Ant. Propagat.*, Vol. 58, N°4, pp. 594–603, March 2007.
- [17] Z. Li, Y. Erdemli, J. Volakis, P. Papalambros, "Design optimization of conformal antennas by integrating stochastic algorithms with the hybrid finite-element method", *IEEE Trans. Ant. Propagat.*, Vol. 50, N°5, pp. 676–684, May 2012.
- [18] E. Hassan, E. Wadbro, M. Berggren, "Topology optimization of metallic antennas", *IEEE Trans. Ant. Propagat.*, Vol. 62, N°5, pp. 2488–2500, May 2014.
- [19] M.P. Bendsoe, O. Sigmund, *Topology optimization. Theory, methods and applications*. Springer, Berlin, 2003.
- [20] S. Kouloudiris, D. Psychoudakis, J. Volakis, "Multiobjective optimal antenna design based on volumetric material optimization", *IEEE Trans. Ant. Propagat.*, Vol. 55, N°3, pp. 1269–1278, April 2010.

-
- [21] S. Zhou, W. Li, Q. Li, "Level-set based topology optimization for electromagnetic dipole antenna design", *J. Comput. Phys.*, Vol. 229, pp. 6915-6930, 2010.
- [22] A. Erentok and O. Sigmund, "Topology optimization of sub-wavelength antennas," *IEEE Trans. Antennas Propag.*, vol. 59, no. 1, pp. 58 –69, Jan. 2011.
- [23] N. Uchida, S. Nishiwaki, K. Izui, M. Yoshimura, T. Nomura, and K. Sato, "Simultaneous shape and topology optimization for the design of patch antennas," in *EuCAP 2009*, Mar. 2009, pp. 103–107.
- [24] T. Nomura, K. Sato, K. Taguchi, T. Kashiwa, and S. Nishiwaki, "Structural topology optimization for the design of broadband dielectric resonator antennas using the finite difference time domain technique," *Int. J. Num. Meth. Eng.*, vol. 71, pp. 1261–1296, 2007.
- [25] G. Kiziltas, D. Psychoudakis, J. Volakis, and N. Kikuchi, "Topology design optimization of dielectric substrates for bandwidth improvement of a patch antenna," *IEEE Trans. Antennas Propag.*, vol. 51, no. 10, pp. 2732 – 2743, Oct. 2003.
- [26] E. Hassan "Topology Optimization of Antennas and Waveguide Transitions", Ph.D thesis, Umeå University, 2015
- [27] P. Jacobsson, T. Rylander, "Gradient-based shape optimisation of conformal array antennas", *Microwaves, Antennas & Propagation, IET* , vol. 4, no. 2, pp. 200 - 209, Feb. 2010
- [28] P. Dubois, C. Dedeban, J.-P. Zolesio, "Antenna's shape optimization and reconstruction by level-set 3D", 2006 *IEEE-AP-S*, July 2006, pp. 581-584.
- [29] S.Osher, R. Fedkiw , "Level Set Methods and Dynamic Implicit Surfaces" Springer, New York, 2003
- [30] D. Oliver, E. L. Miller, and C. M. Rappaport, "A shape reconstruction method for electromagnetic tomography using adjoint fields and level sets", *Inverse Problems*, 16(5):1119, 2000.

- [31] S.Larnier, J.Fehrenbach and Mohamed Masmoudi, "The Topological Gradient Method: From Optimal Design to Image Processing" Milan Journal of Mathematics, 80(2). s00032-012-0196-5, 12/2012
- [32] H. Yigit, "Topology Optimization Procedure to Minimize Radar Cross Section of Perfectly Electric Conductive Structures", PIERS Proceedings, Kuala Lumpur, Malaysia, March 27-30, 2012
- [33] V.Komkov, "The Optimization of the Domain Problem. I. Basic Concepts", Journal of Mathematical Analysis and Applications 82, 317-333, 1981
- [34] S. Jehan-Besson, M. Barlaud, G. Aubert, "Shape Gradients for Histogram Segmentation using Active Contours", Proceedings of the Ninth IEEE International Conference on Computer Vision (ICCV 2003) 2-Volume Set, 2003
- [35] E. A. Soliman, "Semi-Analytical Calculation for Sensitivities of the Method of Moments Impedance and Excitation Matrices", mmce.20251, Published online 30 August 2007 in Wiley InterScience
- [36] D. M. LeVine, R. Meneghini, R. H. Lang, S. S. Seker "Scattering from arbitrarily oriented dielectric disks in the physical optics regime", J. Opt. Soc. Am., Vo. 73, No. 10, pp. 1255-1262, October 1983
- [37] D. Hodge, "Scattering by Circular Metallic Disks", IEEE Trans. Antennas Propag., vol. 28, no. 5, pp. 707-712, Sep. 1980.
- [38] A. Lakhal, "Resolution of Inverse Scattering Problems for the full three-dimensional Maxwell-Equations in Inhomogeneous Media Using the Approximate Inverse", Ph.D thesis, University of Saarlandrs, 2006
- [39] M. Heinkenschloss, R. H.W. Hoppe, V.Schulz, "Numerical Techniques for Optimization Problems with PDE Constraints", Mathematics Subject Classification, Vol. 3, no. 1, pp. 585–652, 2006
- [40] H. Gómez-Sousa, O. Rubiños-López, J. A. Martínez-Lorenzo "Junction Modeling for Piecewise Non-Homogeneous Geometries Involving Arbitrary Materials", 2014 IEEE AP-S & USNC/URSI, July 2014, pp.2196-2197.
- [41] N. K. Georgieva, S. Glavic, M. H. Bakr, J. W. Bandler, "Feasible Adjoint Sensitivity Technique for EM Design Optimization", IEEE Transactions on Microwave Theory and Techniques, Vol. 50, No. 12, Dec 2002

- [42] N.H.Kim , Y.Chang,“Eulerian shape design sensitivity analysis and optimization with a fixed grid”, Computer Methods in Applied Mechanics and Engineering, Vol. 194, no. 30–33, pp. 3291–3314, Aug 2005.
- [43] A. Paganini , “Approximate Shape Gradients for Interface Problems”, Seminar for Applied Mathematics, Research Report No. 2014-12, Mar 2014
- [44] J. Kataja, J. Toivanen, “An elementary formula for computing shape derivatives of EFIE system matrix”, arXiv preprint arXiv:1206.2161,2012
- [45] D. Jones, “A critique of the variational method in scattering problems”, IEEE Trans. Ant. Propagat. IRE., Vol. 4, N°3, pp. 297–301, Jan 2003.
- [46] L.W. Li, P.S. Kooi, Y.L. Qiu, T.S. Yeo, M.S. Leong, “Analysis of electromagnetic scattering of conducting circular disk using a hybrid method”, Journal of Electromagnetic Waves and Applications, Vol.12 No. 9, 1998.
- [47] C. A. Balanis, “Advanced Engineering Electromagnetics”. John Wiley & Sons, 1989.
- [48] M. N. Sadiku, “Numerical Techniques in Electromagnetics”, 2nd ed. CRC Press, 2001.
- [49] J.C. Spall “Introduction to Stochastic Search and Optimization”, John Wiley & Sons, New Jersey, 2003
- [50] D. Peng, B. Merriman, S. Osher, H. Zhao, M. Kang, “A PDE-Based Fast Local Level Set Method”, Journal of Computational Physics, 155, pp. 410–438,1999
- [51] M. C. Delfour, J. -P. Zolésio, “Shapes and Geometries: Metrics, Analysis, Differential Calculus, and Optimization”, Second Edition , Society for Industrial and Applied Mathematics Philadelphia, PA, USA , 2011
- [52] J. H. Holland, “Adaptation in Natural and Artificial Systems”, University of Michigan Press, 1975

- [53] J. Kennedy and R. Eberhart, "Particle Swarm Optimization", Proceedings of IEEE International Conference on Neural Networks IV. pp. 1942–1948.
- [54] S. Kirkpatrick; C. D. Gelatt, M. P. Vecchi. "Optimization by Simulated Annealing", Science, New Series, Vol. 220, No. 4598. (May 13, 1983), pp.671-680
- [55] V. Černý, "Thermodynamical approach to the traveling salesman problem: An efficient simulation algorithm". Journal of Optimization Theory and Applications, Vol. 45, pp.41-51, 1985
- [56] M. Dorigo. "The Metaphor of the Ant Colony and its Application to Combinatorial Optimization" Ph.D. Thesis, Politecnico di Milano, Italy, 1992
- [57] R. E. Bellman, "Dynamic Programming". Princeton, NJ, 1957.
- [58] K.N. Chaudhury, K.R. Ramakrishnan, "Stability and convergence of the level set method in computer vision", Pattern Recognition Letters, Vol.28, No. 7, pp. 884-893, May 2007
- [59] M. Zoppi, C. Dedeban, Ch. Pichot, S. Selleri, and G. Pelosi, "Optimal location of multiple objects or multi-antenna systems". 2012 IEEE AP-S & USNC/URSI, July 2012, Paper s353p2.pdf.
- [60] Z. Zhao, M. Zoppi, Ch. Pichot, and C. Dedeban, "Inversion algorithm for optimizing multi-antenna systems". 2013 IEEE-AP-S & USNC-URSI, July 2013, pp. 532-533.
- [61] Z. Zhao, Ch. Pichot, and C. Dedeban, "Shape gradient optimization for planar antenna arrays", 2014 IEEE AP-S & USNC/URSI, July 2014, pp.1954-1955.
- [62] Z. Zhao, Ch. Pichot, and C. Dedeban, "Level-Set Shape Optimization for Planar Antenna Arrays", 2015 ICEAA, Sep. 2015, Paper 147.pdf.

Abstract

The objective of this thesis work is to find the optimal shape of planar antenna elements and arrays from imposed constraints (e.g. desired or imposed radiation patterns, gain or directivity) or to reconstruct the shape from experimental measurements.

The optimization algorithm is based on the gradient-type method and an active contour reconstruction by means of the Level Set method. The forward problem is solved using an integral formulation of the EM problem with finite element discretization. The shape gradient is computed using two different methods: one is finite differential method based on nodal point mesh derivation with an infinitesimal modification of the triangular elements on the contour along the outward normal direction, another the topological shape gradient, which is computed based on a topological deformation on a contour. A narrow band level set method has been developed to evolve the contour of antennas and arrays using the deformation velocity computed from the shape gradient.

Different configurations of antennas and antenna arrays are studied for investigating the performance of the optimization algorithm. Frequency hopping and multi-frequency techniques have been used for optimizing the shape within a frequency band.

Shape optimization for planar antenna miniaturization has a large number of applications, particularly, for reflectarrays.

Keywords:

Shape Optimization

Method of Moments

Topological Gradient

Planar Antennas

Planar Antenna Arrays

Level Set Method

Résumé

L'objectif de cette thèse est de trouver la forme optimale d'une antenne planaire ou d'un réseau d'antennes planaires à partir de contraintes imposées (diagramme de rayonnement, gain ou directivité) ou de reconstruire la forme à partir de mesures expérimentales.

L'algorithme d'optimisation développé est basé sur une méthode de type gradient et la reconstruction des contours par une méthode d'ensembles de niveaux (*Level Sets*) ou "contours actifs". Le problème direct est résolu en utilisant une formulation intégrale du problème électromagnétique et une méthode d'éléments finis pour la discrétisation. Le gradient de forme est calculé en utilisant deux méthodes différentes. Tout d'abord, une méthode par différences finies basée sur la dérivée à un nœud du maillage, pour une modification infinitésimale des éléments triangulaires du contour, suivant la direction de la normale extérieure. La deuxième méthode est basée sur le gradient topologique pour le calcul de la déformation des contours. Une méthode d'ensembles de niveaux avec bande étroite a été développée pour faire évoluer le contour des antennes utilisant la vitesse de déformation calculée à partir du gradient de forme.

Différentes configurations d'antennes et réseaux d'antennes planaires ont été utilisées pour étudier les performances de l'algorithme d'optimisation. Des techniques de type saut de fréquence et multifréquence ont été utilisées pour optimiser la forme dans une bande de fréquence.

L'optimisation de forme pour la miniaturisation d'antennes planaires concerne de nombreuses applications, en particulier, pour les réseaux réflecteurs.

Mots clé:

Optimisation de forme

Méthodes des moments

Gradient topologique

Antennes planaires

Réseaux d'antennes planaires

Méthode d'ensembles de niveaux

Level Sets